Dissertation
submitted to the
Combined Faculties of the Natural Sciences and Mathematics
of the Ruperto-Carola-University of Heidelberg, Germany
for the degree of
Doctor of Natural Sciences

Put forward by
Georg Gotthilf Günter
Born in: Leonberg
Oral examination: February 4th, 2014

Interfacing Rydberg atoms with light and observing their interaction driven dynamics

Referees: **Prof. Dr. Matthias Weidemüller**
Prof. Dr. Markus Oberthaler

Abstract:

This thesis investigates new phenomena that arise when light is strongly coupled to an interacting atomic gas. For this, a new apparatus has been built which allows to create ultracold and dense atomic samples and to detect individual atoms in high-lying atomic states, so-called Rydberg atoms. Strong light-matter coupling is achieved using the collective coupling of the atomic cloud to the light field under conditions of electromagnetically induced transparency (EIT). In experiments on EIT involving non-interacting Rydberg states, we characterize the light-matter coupling and demonstrate the first combined optical and matter based probing of EIT. By coupling to strongly-interacting Rydberg states, we investigate the effect of interactions which we observe as a strong nonlinear optical response of the atomic gas as well as in the emergence of strong correlations between the hybrid quasi-particles associated with the strong light-matter coupling. We employ the nonlinear response of the atomic cloud to image Rydberg atoms immersed in the atomic cloud. In a theoretical proposal, we show that this novel imaging technique allows to investigate many-body Rydberg states with single particle sensitivity. Using the proposed imaging method, we demonstrate imaging of small numbers of Rydberg atoms with high time-resolution in single shot experiments. In experiments exploiting the dipolar exchange interaction between Rydberg atoms, we employ the new imaging technique to follow dipole-mediated transport of Rydberg excitations through the cloud. The transport dynamics is determined by the continuous spatial projection of the electronic quantum state under observation and features an emergent spatial scale of micrometer size induced by Rydberg-Rydberg interactions.

Zusammenfassung:

Diese Doktorarbeit untersucht die starke Kopplung von Licht an wechselwirkende atomare Gase. Hierfür wurde eine neue Apparatur aufgebaut, die es uns ermöglicht ultrakalte atomare Gase mit hohen Dichten zu erzeugen und einzelne Atome in hoch angeregten elektronischen Zuständen, so genannte Rydbergatome, zu detektieren. In den Experimenten werden die Atome und das Lichtfeld mittels elektromagnetisch induzierter Transparenz (EIT) stark gekoppelt. In Untersuchungen mit nicht wechselwirkenden Rydbergzuständen wird die Licht-Materie-Kopplung charakterisiert und erstmals sowohl der Licht- als auch der Materiefreiheitsgrad des gekoppelten Systems analysiert. In Experimenten mit stark wechselwirkenden Rydbergzuständen, wird der Einfluss der Wechselwirkung auf EIT untersucht. Als Folge der Wechselwirkung werden ein stark nichtlineares optisches Verhalten des atomaren Gases und Korrelationen zwischen den hybriden Quasiteilchen beobachtet. Unter Verwendung der optischen Nichtlinearität des atomaren Gases wird ein neues Verfahren vorgestellt, welches uns ermöglicht Rydbergatome in dichten ultrakalten Gasen optisch sichtbar zu machen. In theoretischen Untersuchungen wird gezeigt, dass die neue Abbildungsmethode es erlaubt Vielteilchenzustände von Rydbergatomen auf der Ebene einzelner Rydbergatome zu untersuchen. Anschließend werden in ersten Experimenten Verteilungen mit wenigen Rydbergatomen ortsaufgelöst und mit hoher Zeitauflösung nachgewiesen. Abschließend wird die Abbildungsmethode zur Untersuchung von dipolaren Transportphenomänen in Rydberggasen verwendet. Die experimentellen Ergebnisse zeigen, dass die Transportdynamik entscheidend durch die ständige Projektion des elektronischen Zustands während der Messung beeinflusst wird. Zusätzlich besitzt die Transportdynamik aufgrund der Abbildungsmethode eine charakteristische Längenskala in der Größenordnung einiger Mikrometer, die die Transporteigenschaften entscheidend modifiziert.

This thesis is based on the following manuscripts and publications:

- **Combined optical and population-based measurements of Rydberg electromagnetically induced transparency**
  C.S. Hofmann, G. Günter, H. Schempp, M. Robert-de-Saint-Vincent, S. Whitlock, M. Weidemüller
  in preparation

- **Observing the dynamics of dipole-mediated energy transport by interaction enhanced imaging**
  G. Günter, H. Schempp, M. Robert-de-Saint-Vincent, V. Gavryusev, S. Helmrich, C.S. Hofmann, S. Whitlock, M. Weidemüller
  Science **342**, 954 (2013)

- **An experimental approach for investigating many-body phenomena in Rydberg-interacting quantum systems**
  C.S. Hofmann, G. Günter, H. Schempp, N.L.M. Müller, A. Faber, H. Busche, M. Robert-de-Saint-Vincent, S. Whitlock and M. Weidemüller
  Frontiers of Physics, (2013)

- **Sub-Poissonian Statistics of Rydberg-Interacting Dark-State Polaritons**
  C.S. Hofmann, G. Günter, H. Schempp, M. Robert-de-Saint-Vincent, S. Whitlock, M. Weidemüller
  Physical Review Letters **110**, 203601 (2013)

- **Interaction Enhanced Imaging of Individual Rydberg Atoms in Dense Gases**
  G. Günter, M. Robert-de-Saint-Vincent, H. Schempp, C. S. Hofmann, S. Whitlock, M. Weidemüller
  Physical Review Letters **108**, 013002 (2012)

The author furthermore contributed to the following publications:

- **Full Counting Statistics of Laser Excited Rydberg Aggregates in a One-Dimensional Geometry**
  H. Schempp, G. Günter, M. Robert-de-Saint-Vincent, C. S. Hofmann, D. Breyel, A. Komnik, D. W. Schönleber, M. Gärttner, J. Evers, S. Whitlock, and M. Weidemüller
  arXiv:1308.0264 (2013), accepted for publication at Physical Review Letters

- **Spontaneous avalanche ionization of a strongly blockaded Rydberg gas**
  M. Robert-de-Saint-Vincent, C. S. Hofmann, H. Schempp, G. Günter, S. Whitlock, M. Weidemüller
  Physical Review Letters **110**, 045004 (2013)

- **Quantum interference in interacting three-level Rydberg gases: coherent population trapping and electromagnetically induced transparency**
  S. Sevinçli, C. Ates, T. Pohl, H. Schempp, C. S. Hofmann, G. Günter, T. Amthor, M. Weidemüller, J. D. Pritchard, D. Maxwell, A. Gauguet, K. J. Weatherill, M. P. A. Jones, C. S. Adams
  Journal of Physics B **44**, 184018 (2011)

- **Coherent Population Trapping with Controlled Interparticle Interactions**
  H. Schempp, G. Günter, C.S Hofmann, C. Giese, S.D. Saliba, B.D DePaola, T. Amthor, M. Weidemüller, S. Sevinçli, T. Pohl
  Physical Review Letters **104**, 173602 (2010)

- **Switching ultrastrong light-matter coupling on a subcycle scale**
  R. Huber, A. A. Anappara, G. Günter, A. Sell, S. De Liberato, C. Ciuti, G. Biasiol, L. Sorba, A. Tredicucci, A. Leitenstorfer
  Journal of Applied Physics **109**, 102418 (2011)

- **Sub-cycle switch-on of ultrastrong light-matter interaction**
  G. Günter, A. A. Anappara, J. Hees, A. Sell, G. Biasiol, L. Sorba, S. De Liberato, C. Ciuti, A. Tredicucci, A. Leitenstorfer, R. Huber
  Nature **458**, 178 (2009)

Contents

1 Introduction **1**

2 Ultracold Rydberg atoms **5**
2.1 Rydberg atoms 6
2.1.1 Alkali Rydberg atoms 6
2.1.2 Rydberg atoms in electric fields 8
2.1.3 Rydberg-Rydberg interactions 10
2.1.4 Rydberg atom-light interactions 17
2.2 Ultracold Rydberg atoms in dense atomic samples 21
2.2.1 Preparation of dense ultracold atomic samples 22
2.2.2 Rydberg excitation and detection 26

3 Rydberg electromagnetically induced transparency **31**
3.1 Theory of electromagnetically induced transparency 32
3.1.1 Light-matter interaction in a three-level system 32
3.1.2 Probe light propagation 35
3.1.3 Electromagnetically induced transparency resonance 37
3.1.4 Dark-state polaritons 39
3.2 Experimental study of Rydberg-EIT in an ultracold gas of ^{87}Rb 41
3.2.1 Reconstruction of the coupling beam profile and the Rydberg distribution 41
3.3 Theoretical description of light propagation in an interacting Rydberg gas 45
3.3.1 Rydberg-interacting polaritons 45
3.3.2 Optical response of the interacting gas 47
3.4 Optical and matter-based probing of interacting polaritons 49
3.4.1 Optical probing of the polaritons 50
3.4.2 Matter-based probing of the polaritons 52
3.4.3 Interplay of photonic and atomic correlations 53
3.4.4 Perspectives 53

4 Interaction enhanced imaging: A proposal **55**
4.1 State of the art Rydberg imaging techniques 56
4.2 Basic principle of interaction enhanced imaging 57
4.3 Optimal parameters 60

4.4 Simulations 62
4.4.1 Rydberg excitation 63
4.4.2 Imaging process 63
4.5 Extracting spatial correlations 65
4.6 Perspectives 67

5 Interaction enhanced imaging: Experiments 69
5.1 Experimental implementation 69
5.1.1 Density dependence 73
5.1.2 Electric field tuning 74
5.1.3 Sensitivity 75
5.2 Imaging the Rydberg blockade 77
5.3 Towards imaging of single Rydberg atoms 78

6 Dipole-mediated energy transport in Rydberg-gases 81
6.1 Transport dynamics during imaging 82
6.2 Environment assisted transport 84
6.2.1 A simple model 85
6.3 Perspectives 89

7 Conclusion 91

Bibliography 93

1 Introduction

The interaction between light and matter is one of the fundamental processes in nature and is ubiquitous therein. It is responsible for everyday phenomena like the refraction of light and plays an important role in many processes such as black-body radiation or photosynthesis. Hence, a lot of what we know today about nature and its constituents is intimately connected with our understanding of how light and matter interact. For instance, the investigation of light emitted by highly excited atoms by Johannes Rydberg and others [Ryd90], the black-body radiation laws discovered by Planck [Pla01] and the explanation of the photoelectric effect by Albert Einstein [Ein05] were milestones in the development of quantum mechanics. Our insight into the interplay of light and matter sets the basis for modern technologies with the invention of the laser [Mai60, Tow10] and liquid crystals [Fré27] as just two widely spread examples. To understand and control atom-light interactions at the level of individual quanta is at the heart of modern quantum optics [Har89]. Our ability to control and manipulate single photons or single matter excitations and their interplay is constantly improving (see e.g. Nobel prize in physics in 2012 [Har12]) and ultimately might enable future technologies such as quantum networks [Rit12, Per13] or large-scale universal quantum simulators [Blo12, Sch13a].

Of particular interest to current experiments is the regime of *strong coupling between light and matter*. In this regime, the coherent and reversible light-matter coupling dominates over dissipative processes and as a consequence, light and matter can no longer be regarded as separate entities. This mixing of light and matter gives rise to fascinating phenomena. For instance, it allows to transfer the quantum state of the light field in a controlled fashion onto the atoms and vice versa. One approach to achieve strong light-matter coupling is to enhance the effect of the light field using optical resonators as pursued in cavity quantum electrodynamics [Kim98]. In a cavity a photon interacts many times with an atom, resulting in an enhanced light-matter coupling. An alternative route involves the propagation of light through optically thick media consisting of many atoms which gives rise to a similar enhancement [Ham10]. In this case, one obstacle is to overcome spontaneous emission which introduces decoherence and typically accompanies the atom-light interaction.

An almost ideal light-matter interface can be realized using electromagnetically induced transparency (EIT) in which spontaneous emission can be eliminated while maintaining strong coupling to the light field [Fle05]. In EIT the presence of an additional strong light field renders an otherwise strongly absorbing medium transparent to a weak probe field acting like an optical switch. To illustrate the strong light-matter

coupling, we consider a single probe photon impinging on an atomic cloud as depicted in Fig. 1.1 (a). As the photon enters the cloud, the strong light-matter coupling partially converts the photon into a collective atomic excitation and forms a hybrid state of light and matter characterized by the appearance of a quasi-particle called dark-state polariton. The transformation into a dark-state polariton happens coherently, meaning that the conversion is loss free and the photon is fully recovered upon leaving the atomic cloud. While travelling through the cloud, the photon acquires a matter component and consequently inherits the properties of the atomic system, offering the fascinating possibility to manipulate light. For instance, this has been employed to slow down light [Hau99], to imprint magnetic moments onto the light field [Kar06] or to make photons sensitive to electric fields realizing giant Kerr-effects [Moh08]. These remarkable effects can be understood on the level of single (quasi-)particles.

We ask the question what happens when light is coupled to a *strongly interacting atomic many-body system*? With the unprecedented access and control over microscopic degrees of freedom of atoms possible these days, the research focus has shifted from exploring weakly interacting ultracold quantum gases to the creation and manipulation of strongly correlated atomic systems [Blo08]. Recently, it has become possible to investigate effects of strong electric dipole-dipole interactions using atoms in highly excited Rydberg states. Due to their huge size these atoms have exaggerated properties [Gal05]. For example, Rydberg atoms exhibit large dipole moments and show enormous long range electric dipole-dipole interactions [Gal08, Saf10]. In addition, the nature and strength of these interactions can be controlled by the choice of states and by external electric fields. When exciting atoms to Rydberg states with coherent light fields, the interactions give rise to strong atomic correlations and lead to many-body phenomena such as the Rydberg blockade [Luk01], in which it is possible to excite only a single Rydberg atom within a certain volume. As each blockade volume collectively shares a single excitation, also the interaction with the light field is modified and all the atoms within a blockade volume act as an effective two-level atom with enhanced coupling to the light field [Rob05, Gae09, Hei07]. Lately, interfacing Rydberg atoms with the light field using EIT has become possible and first experiments have demonstrated strong light-matter coupling involving Rydberg states [Moh07, Pri10].

In this thesis, we investigate strong light-matter coupling using EIT in ultracold atomic gases coupled to Rydberg states. With the potential to detect both the light and matter parts of the coupled light-matter system, this system enables unprecedented studies of strong light-matter coupling in EIT. The phenomena investigated in this thesis are schematically depicted in Fig. 1.1. In Ch. 3, we present the first matter-based probing of EIT by detecting the polaritons via their matter component inside the cloud using field ionization detection of Rydberg states. After the characterization of our system in the non-interacting regime (Ch. 3.2), we turn to the regime of strong atomic interactions (Ch. 3.4). The coupling of photons to strongly interacting Rydberg states leads to effective photon-photon interactions (Fig.1.1 (b)). We observe the effect of the interactions as a huge nonlinear optical response of the atomic cloud to the probe light

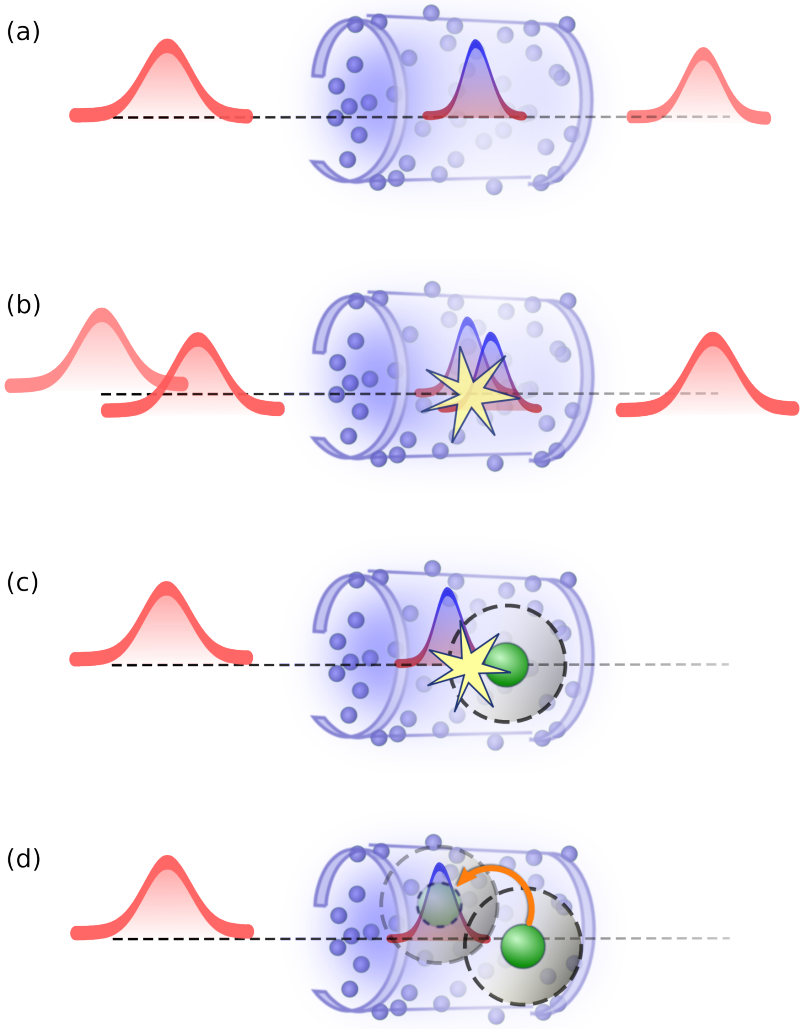

Figure 1.1: Illustration of the investigated light-matter interactions. (a) An incoming photon is converted into a dark-state polariton upon entering the atomic cloud. It travels without loss through the cloud with reduced group velocity and is coherently mapped back into the initial light mode upon leaving the cloud. (b) The interactions between polaritons mediated by the Rydberg-Rydberg interactions lead to scattering of a second polariton by the first one, resulting in an optical nonlinearity on the single photon level. (c) The scattering of polaritons on Rydberg atoms (green sphere) can be employed to sensitively detect individual Rydberg atoms. (d) Quantum-state exchange interaction between a Rydberg atom and the polaritons gives rise to dipolar transport of the Rydberg excitation.

field. We characterize the optical nonlinearity and map out its full range reaching deep into the strongly blockaded regime. Concomitant with the nonlinear optical response, we observe the emergence of correlations between the dark-state polaritons.

By exploiting the strong interactions between atoms in different Rydberg states combined with the optical nonlinearity of the atomic gas, we introduce a fundamentally new imaging method that allows us to resolve otherwise invisible distributions of Rydberg atoms. In a theoretical study (Ch. 4), we show that this technique allows to image individual Rydberg atoms embedded in dense atomic gases (Fig.1.1 (c)). Performing simulations of the imaging process including experimentally relevant noise sources, we show that it should be possible to image interacting many-body Rydberg states with single particle sensitivity. In Ch. 5 we turn to the experimental realization of this imaging technique. We demonstrate sensitive, spatially resolved detection of small numbers of Rydberg atoms and probe the Rydberg blockade in a new way.

In the last part of this thesis, we make use of our new imaging technique to observe the time evolution of this interacting light-matter system (Ch. 6). As a surprise, we discover that for certain Rydberg states the Rydberg distributions are not stationary during the imaging process. We find that the observed dynamics is mediated by dipolar exchange interactions between Rydberg atoms (Fig.1.1 (d)). Furthermore, the continuous observation in the imaging process acts as an environment to the transport dynamics and introduces a new spatial scale of micrometer size induced by the Rydberg-Rydberg interactions. Since the environment depends on the laser parameters, our system presents a promising model system to study dipolar transport phenomena which might help to elucidate open questions like the role of entanglement or the transition from classical to quantum behaviour in energy transport.

2 Ultracold Rydberg atoms

Parts of this chapter are included in the following publication:

An experimental approach for investigating many-body phenomena in Rydberg-interacting quantum systems
C.S. Hofmann, G. Günter, H. Schempp, N.L.M. Müller, A. Faber, H. Busche, M. Robert-de-Saint-Vincent, S. Whitlock and M. Weidemüller
Frontiers of Physics, (2013)

Highly excited, so-called Rydberg atoms, have been studied since the early days of quantum mechanics. The combination with ultracold atomic gases at the end of the 1990s has renewed the interest in these highly excited atoms and has revolutionized the field of Rydberg physics [Löw12]. Since, the field of ultracold Rydberg physics has developed into a diverse rapidly growing research area with topics ranging from quantum computing [Saf10] and quantum non-linear optics [Pri13] over strongly correlated plasmas [Kil07, Rol08] and ultracold chemistry [Ben09] to investigations of exotic quantum phases [Pup10, Hen10]. At the heart of the diverse phenomena that are explored in all these areas are the remarkable properties of Rydberg atoms. The large separation between the Rydberg electron and the atomic core and the concomitant loose binding leads to exaggerated properties of Rydberg atoms such as huge electric polarizabilities and strong dipole-dipole or van der Waals interactions. In ultracold Rydberg gases, the interaction energy can be much larger than all other energy scales, rendering a system that is dominated by interactions which leads to peculiar properties in the interplay with the light field.

Here, we review some of the basic properties of Rydberg atoms. In particular, the origin and the nature of the strong Rydberg-Rydberg interactions are discussed. Also, how these interactions in the interplay with the light field can induce spatial correlations in ultracold Rydberg gases is briefly introduced. Then, the experimental apparatus which was built in the course of this thesis is presented. The apparatus allows us to produce dense ultracold atomic clouds and to detect Rydberg atoms with single particle sensitivity. Moreover, it offers good optical access to the ultracold atoms, which is a key ingredient for the presented experiments on Rydberg atom-light interactions.

2.1 Rydberg atoms

Atoms with at least one electron in a highly excited state are referred to as Rydberg atoms. In the Rydberg state the electron is loosely bound and mostly far from the core. It therefore mainly experiences a $1/r$-potential, which renders Rydberg atoms, very similar to hydrogen atoms.

The investigation of these highly excited atomic states reaches back to the 19th century. Balmer established an empirical formula to describe the spectral lines of hydrogen observed by Ångstrom and others [Ång55, Bal85] which was shortly after generalized and extended to other chemical elements by Rydberg [Ryd90]. The Bohr-model [Boh13] provided the first theoretical description to explain the empirical findings by linking the observed spectra of hydrogen to the binding energy of the electron

$$E_n = -hc\frac{R_\infty}{n^2}, \tag{2.1}$$

where h is the Planck constant, c the speed of light and n the principal quantum number, which characterizes the state of the atom. The Rydberg constant can be expressed in terms of fundamental constants

$$R_\infty = \frac{m_e e^4}{8\,c\,\varepsilon_0^2\,h^3} \tag{2.2}$$

with e the elementary charge, m_e the electron mass, and ε_0 the vacuum permittivity. Like the binding energy, many properties of hydrogen show a characteristic scaling with the principal quantum number n which can already be derived within the simple Bohr-model. As high-lying electronic states of multi-electron atoms are very similar to the states of hydrogen, these scaling laws still hold despite the more complex structure of these atoms as will be discussed in the following.

2.1.1 Alkali Rydberg atoms

In this thesis we deal with highly excited states of rubidium which as an alkali atom has one valence electron. The other 36 electrons fill up the inner shells and together with the nucleus form the core. The core electrons are tightly bound and almost unperturbed by the valence electron. Hence, for highly excited states of the valence electron, the core and the valence electron form a hydrogen-like system. In contrast to hydrogen, electronic states with low angular momentum not only experience a singly charged core, as they penetrate and sample the substructure of the core. This leads to an energy shift of the rubidium Rydberg states with respect to the ones of hydrogen. Inside the core, the valence electron experiences an increased charge due to the reduced shielding of the nucleus and also polarizes the core. Both effects lead to an increased binding and a lowering in energy of these states.

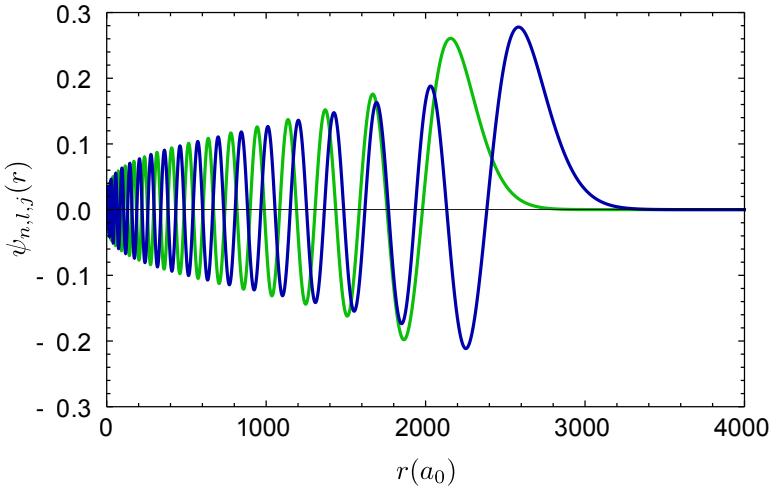

Figure 2.1: Rydberg wavefunction for the $|37S_{1/2}\rangle$-state of rubidium and hydrogen. The blue curve shows the wavefunction for the $|37S_{1/2}\rangle$-state of hydrogen calculated using PotCalc [Sin04]. The wavefunction of ^{87}Rb in the same state (green) is very similar to the one of hydrogen. The increased binding due to the extended core essential leads to a shifted hydrogen wavefunction. The distance r from the core is given in units of the Bohr-radius a_0.

The effect of the core can be taken into account using quantum defect theory [Sea83, Gal05]. The extent of the core only modifies the potential in the very inner part, where the kinetic energy is large and the wavefunction oscillates rapidly. The increased potential depth compared to the Coulomb-potential of hydrogen results in faster oscillations of the wavefunction in this region and leads to a phase shift of the wavefunction outside the core with respect to the hydrogen wavefunction. This phase shift can be accounted for by replacing the hydrogenic quantum number n by an effective principal quantum number $(n^*) = (n - \delta_{n,l,j})$ with $\delta_{n,l,j}$ the quantum defect for the state $|n, l, j\rangle$. With this modification the energy levels of the rubidium Rydberg-states can be written like the hydrogen levels as

$$E_{n,l,j} = -hc\frac{R_{Rb}}{(n^*)^2} \tag{2.3}$$

with $R_{Rb} = 109736.62\,\mathrm{cm}^{-1}$, the Rydberg constant for ^{87}Rb[1]. The quantum defect is determined by spectroscopic measurements [Han06] and can be approximated using the empirical Rydberg-Ritz formula [Gal05]. As the quantum defect reflects the penetration of the core, it depends on the quantum numbers n, l and j and decreases for states with increasing angular momentum. This results in additional structure of the energy-levels of alkali Rydberg states compared to hydrogen. As can be seen in Fig.2.2 (a) the $|S\rangle$, $|P\rangle$ and $|D\rangle$ states are energetically separated from the other states which allows us

[1]Accounting for the effective mass, the Rydberg constant is given by $R_{Rb} = R_\infty/(1 + m_e/m_{Rb})$.

property		(n^*)-scaling
binding energy	E_n	$(n^*)^{-2}$
level spacing	$E_{n+1} - E_n$	$(n^*)^{-3}$
lifetime	τ	$(n^*)^3$
ionisation field	$\mathcal{E}_{ion}$	$(n^*)^{-4}$
transition dipole matrix element	$\langle nl\vert\, \hat{\boldsymbol{d}}\, \vert n'l'\rangle$	$(n^*)^2$
polarizability	α	$(n^*)^7$
dipole coefficient	C_3	$(n^*)^4$
van der Waals coefficient	C_6	$(n^*)^{11}$

Table 2.1: Scaling laws for properties of Rydberg atoms. Some of the important properties of Rydberg atoms and their scaling with the effective principal quantum number $(n^*) = (n - \delta_{n,l,j})$ [Gal05].

to readily address them in the experiments. For $l > 3$ the centrifugal barrier prevents the electron from being close to the core and the quantum defect becomes negligible $\delta_{n,l,j} \approx 0$. Therefore, the states with $l > 3$ are degenerate like for hydrogen and are thus often referred to as the hydrogenic manifold.

As the effect of the extended core can be encapsulated in the effective quantum number, the properties of Rydberg atoms exhibit the same scaling laws like the hydrogen atom, but with n replaced by (n^*). Some important properties and their scalings are given in Tab. 2.1. These scalings illustrate the exaggerated properties of the Rydberg atoms. For instance, for rubidium Rydberg atoms in the $50S$-state, the strength of the van der Waals interaction approximately is 16 orders of magnitudes larger than for ground state atoms.

2.1.2 Rydberg atoms in electric fields

Given the enormous size and the loose binding of the electron to the core, Rydberg atoms are very sensitive to their environment, especially to electric fields. Here, we discuss two cases relevant for the experiments: for small electric fields the Rydberg atoms show large Stark shifts which allows to tune their energies and manipulate their properties. For larger but still moderate electric fields, the loose binding of the electron allows to separate the electron from the core and to ionize the Rydberg atom which can be employed to detect Rydberg atoms.

Stark-shift

The dipole interaction of the atom with the electric field leads to coupling of states of opposite parity. For small angular momenta ($l \leq 3$), the core potential lifts the l-degeneracy and second order non-degenerate pertubation theory can be applied. These

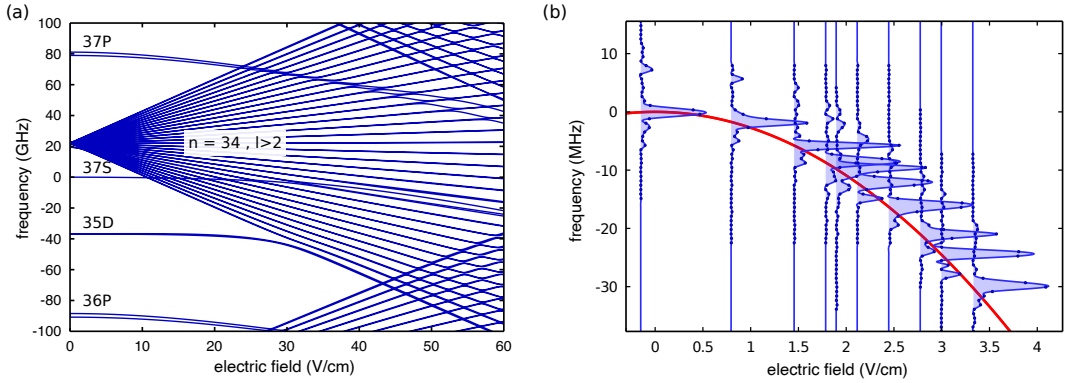

Figure 2.2: Stark map around the $|37S_{1/2}\rangle$-state of ^{87}Rb. (a) Calculated Stark map for the states in the vicinity of the $37S$-state using PotCalc [Sin04]. (b) Measured Stark map using field ionization. The blue dots show the measured ionization spectra for different electric fields. The solid lines are guides to the eye. The red line is a quadratic fit to the peak positions of the spectra.

states therefore show a quadratic Stark shift

$$\delta E_{n,l,j} = \sum_{n',l',j' \neq n,l,j} \frac{|\langle \psi_{nlj}| \hat{\boldsymbol{d}} \cdot \boldsymbol{\mathcal{E}} |\psi_{n'l'j'}\rangle|^2}{E_{nlj} - E_{n'l'j'}} = \frac{1}{2}\alpha \mathcal{E}^2 \tag{2.4}$$

for small electric fields $\mathcal{E}$, where the sum runs over all bare atomic states. As the dipole moment scales with $(n^*)^2$ and the energy difference between neighbouring states decreases with $(n^*)^{-3}$, we can readily deduce the $(n^*)^7$ scaling of the polarizability α given in Tab. 2.1.

In the hydrogenic manifold ($l > 3$), states with opposite parity are degenerate and form new eigenstates with respect to the electric dipole interaction which possess a permanent dipole moment. Hence these states exhibit a linear Stark shift in small electric fields. In general, Rydberg atoms in an electric field acquire a permanent dipole moment which is given by the derivative of their energy with respect to the electric field.

Fig. 2.2 (a) shows the calculated energies of Rydberg states in an electric field, a so-called Stark map, for states in the vicinity of the $37S_{1/2}$-state. As discussed, the states with low angular momentum show a quadratic shift for small electric fields in contrast to the linear behaviour of the states in the hydrogenic manifold. The Rydberg atoms are highly susceptible to electric fields, as can be seen in Fig. 2.2 (b). Fields on the order of a few Volts per centimeter already shift the relatively low-lying $37S_{1/2}$-state by a few tens of MHz, which is much larger than the excitation linewidth in the experiment. On the one hand, this can be used as a tool to tune the energy of Rydberg states or to employ Rydberg atoms as sensitive probes for small electric fields [Tau10, Sed12]. On the other hand, it also poses strict requirements on the electric field control needed in experiments.

Ionization

Due to the reduced binding of the Rydberg electron, already moderate fields are sufficient to separate the electron and the core and to ionize a Rydberg atom. Therefore field ionization and subsequent detection of the positively charged core and/or the electron has become an established technique to detect Rydberg atoms. With the ionization field depending on the state of the atoms, field ionization even allows for state selective detection of the Rydberg atoms.

To estimate the electric field needed to ionize a Rydberg atom, we consider a constant electric field, e.g., in the $z-$direction. The field deforms the Coulomb-potential and leads to an anisotropic potential with a local maximum. The ionization threshold is given by the field, where the binding energy matches the potential energy of the local maximum, giving

$$\mathcal{E}_{ion} = \frac{\pi\varepsilon_0(hcR_{Rb})^2}{e^3\,(n^*)^4} \tag{2.5}$$

$$\approx 3.2138 \cdot 10^5 \frac{\mathrm{kV}}{\mathrm{cm}} \times (n^*)^{-4}. \tag{2.6}$$

For instance, for the $37S$-state this corresponds to $\sim 245\,\mathrm{V/cm}$ whereas for the $50S$-state the required ionization field is much lower and only amounts to $\sim 65\,\mathrm{V/cm}$. This shows that field ionization allows to detect Rydberg atoms state-selectively in the experiment. The actual ionization dynamics are more complex, as quantum mechanically one has to consider the exact path through the Stark map with its avoided crossings which are passed adiabatically or diabatically, depending on the switching speed of the electric field [Gal05]. Nevertheless, the simple scaling provided here gives a good estimate for the fields required in the experiment and yields the correct scaling of the ionization field.

2.1.3 Rydberg-Rydberg interactions

The extraordinarily strong interactions between Rydberg atoms are the key ingredient for many fascinating phenomena in Rydberg physics. Here, we discuss the origin and the character of these interactions. We focus on the particular case of interactions of nS-states of ^{87}Rb which are relevant for the presented experiments.

Rydberg atoms interact via electric dipole-dipole interactions. Classically this can be understood as follows: a fluctuation in the charge distribution of one Rydberg atom instantaneously creates a dipole moment, that in turn induces a dipole moment in another atom with which it can interact. The operator describing the dipole-dipole interaction between two atoms is given by

$$\hat{\mathcal{V}}_{dd}(\boldsymbol{R}) = \frac{\hat{\boldsymbol{\mu}}_1 \cdot \hat{\boldsymbol{\mu}}_2}{R^3} - \frac{3(\hat{\boldsymbol{\mu}}_1 \cdot \boldsymbol{R})(\hat{\boldsymbol{\mu}}_2 \cdot \boldsymbol{R})}{R^5} \tag{2.7}$$

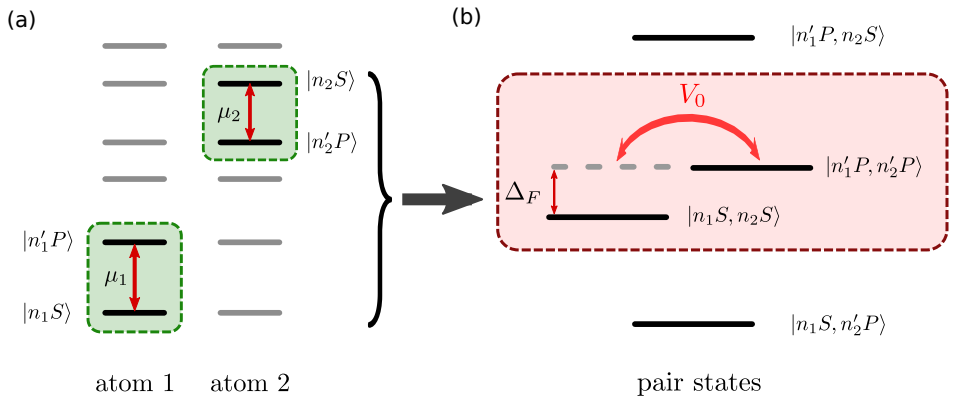

Figure 2.3: Bare atomic states and relevant pair states for the interaction. (a) schematically depicts the bare atomic states of two atoms. For the interaction between the atoms in the states $|n_1S\rangle$ and $|n_2S\rangle$, the main contribution to the interaction strength originates from coupling to the energetically closest pair state $|n_1'P, n_2'P\rangle$. (b) shows the pair states involving the four bare atomic states marked with green boxes in (a). Only the states $|n_1S, n_2S\rangle$ and $|n_1'P, n_2'P\rangle$ are coupled and the interaction of the atoms can be approximated considering these two levels. The energy difference between the coupled pair states is given by the Förster defect Δ_F.

where $\hat{\boldsymbol{\mu}}_1$ and $\hat{\boldsymbol{\mu}}_2$ are the dipole operators acting on atom one and two, respectively, and $\boldsymbol{R}$ denotes the vector separating the two atoms. Typically, the internal electronic dynamics is much faster than the motion of the atoms, and hence the distance between the atoms can be treated as a classical parameter in the Hamiltonian.

To calculate the interaction strength between two atoms, we have to determine the energy levels of the two coupled atoms which are governed by the Hamiltonian

$$\hat{\mathcal{H}} = \hat{\mathcal{H}}_1 \otimes \mathbf{1} + \mathbf{1} \otimes \hat{\mathcal{H}}_2 + \hat{\mathcal{V}}_{dd}(\boldsymbol{R}). \tag{2.8}$$

where $\hat{\mathcal{H}}_1$ and $\hat{\mathcal{H}}_2$ describe the energy levels of the two individual atoms. The energies of the coupled atoms are conveniently calculated in a pair state basis. The energy shift of a pair state due to the interactions reflects the interaction strength of the two atoms in this particular pair state. These energy shifts can only be obtained approximately, since all atomic states become coupled by the dipole-dipole interaction.

Two-state approximation

The largest contribution to the interaction between two atoms in a particular pair state originates from the coupling to the energetically closest pair state that is directly coupled. Considering only the coupling of these two pair states provides qualitative insights into the origin and nature of the interactions.

Fig. 2.3 (a) schematically shows the bare atomic states of the two atoms. In the experiments, we use the interactions of nS-Rydberg states $\{|n_1S\rangle, |n_2S\rangle\}$ to which we

will restrict the discussion in the following. Using the energetically closest coupled pair state $|n_1'P, n_2'P\rangle$, we determine the interaction of the atoms in the reduced pair state basis shown in Fig. 2.3 (b). The two pair states $|n_1S, n_2S\rangle$ and $|n_1'P, n_2'P\rangle$ are coupled via the dipole-dipole interaction and the Hamiltonian of the reduced system is given by

$$\hat{\mathcal{H}}_{red} = \begin{pmatrix} 0 & V_0/R^3 \\ V_0/R^3 & \Delta_F \end{pmatrix} , \tag{2.9}$$

where $V_0/R^3 = \langle n_1S, n_2S| \hat{\mathcal{V}}_{dd}(\boldsymbol{R}) |n_1'P, n_2'P\rangle$ is the strength of the dipole-dipole coupling and $\Delta_F = [E(n_1'P) + E(n_2'P)] - [E(n_1S) + E(n_2S)]$ is the energy difference between the two pair states, the so-called Förster defect. Solving for the energies of the coupled pair states, we find

$$E_\pm = \frac{1}{2}\left(\Delta_F \pm \sqrt{\Delta_F^2 + 4V_0^2/R^6}\right) . \tag{2.10}$$

The energies of the coupled atoms depend on the distance R and we can identify three types of interactions:

- **resonant dipole-dipole interaction** ($V_0/R^3 \gg \Delta_F$): For small distances or when the Förster defect is tuned to zero via electric fields, the dipole-dipole coupling dominates and the Rydberg states exhibit dipolar interactions, since the energies of the pair states

$$E_\pm \simeq \pm\frac{V_0}{R^3} = \pm\frac{\hbar C_3}{R^3} \tag{2.11}$$

  show a R^{-3} dependence[2]. The associated C_3-coefficient is related to the product of the two dipole matrix elements and hence shows a $(n^*)^4$-scaling.

- **van der Waals interaction** ($V_0/R^3 \ll \Delta_F$): For large distances the dipole-dipole coupling is only pertubative and the energies of the two states are approximately given by

$$E_+ \simeq \Delta_F + \frac{V_0^2/\Delta_F}{R^6} \qquad \text{and} \qquad \mathrm{E_-} \simeq -\frac{\mathrm{V_0^2/\Delta_F}}{\mathrm{R^6}} = \frac{\hbar \mathrm{C_6}}{\mathrm{R^6}}. \tag{2.12}$$

  In this regime, the Rydberg atoms exhibit van der Waals type interaction, as the energy of the pair states shifts with R^{-6}. In general, the C_6-coefficient strongly depends on the effective principal quantum number. The coupling strength V_0 scales with $(n^*)^4$ and the energy difference between the states scales as $(n^*)^{-3}$

[2] This is only valid down to the LeRoy radius, at which the electron clouds start to overlap and electron exchange has to be taken into consideration [Boi02].

which results in a $(n^*)^{11}$ dependence of the C_6-coefficient. Whether the states show attractive or repulsive interactions is determined by the sign of the Förster defect. With the given definitions, $C_6 > 0$ corresponds to repulsive interactions.

- **state exchange interaction**: For atoms in different atomic states, the interactions can lead to state exchange between the two atoms by the following process

$$n_1S + n_2S \overset{V_0}{\Longleftrightarrow} n_1'P + n_2'P \overset{V_0'}{\Longleftrightarrow} n_2S + n_1S. \tag{2.13}$$

  This process only occurs for atoms with a small difference $\delta n = n_1 - n_2$ in the principal quantum number. For pairs with large δn, V_0' is negligibly small and no exchange takes place. Exchange interactions are also important for the interplay between Rydberg S- and P-atoms. Here, the intermediate pair state is not needed and the pair states with exchanged Rydberg excitations are directly coupled. Since these two pair states are always degenerate, the involved Rydberg states strongly interact via dipolar exchange interactions.

The crossover between dipolar and van der Waals interaction happens for $V_0(R) = \Delta_F$, corresponding to a distance $R_{cross} = (\hbar C_3/\Delta_F)^{1/3}$. The behaviour of an interacting Rydberg gas in the two regimes is quite distinct. The dipolar interactions are inherently long-range. In contrast, in the van der Waals regime the interactions are dominated by the nearest neighbours and the sharp drop of the interaction strength often allows one to introduce a cut-off radius outside of which the interactions are negligible.

In contrast to the vast majority of interacting many-body systems, the interactions of Rydberg atoms can be tuned employing the huge susceptibility of Rydberg atoms to electric fields [Vog06, Wes06, Rya10, Nip12, Gur12]. By tuning pair states into resonance via what is referred to as a Förster resonance, dipolar interactions with a range even larger than the extent of the entire atomic ensemble can be achieved. We will employ electric field tuning in the experiment to further enhance the interactions between the atoms.

In an electric field, the Rydberg-atoms acquire a permanent electric dipole moment. As the interaction of two permanent dipoles scales as R^{-3}, the interaction strength even in very small electric fields will be dipolar for very large distances.

Interactions of nS-states of ^{87}Rb

To calculate the interactions of Rydberg atoms, in principle all states or practically many states have to be considered. This can be accomplished by numerically solving for the energy levels of two coupled atoms including many atomic levels. The interaction coefficients C_3 and C_6 are then obtained by fitting the short and long-range behaviour with C_3/R^3 and C_6/R^6, respectively [Sin05]. In the van der Waals regime, the dipolar coupling is only pertubative and the interaction coefficient can be obtained

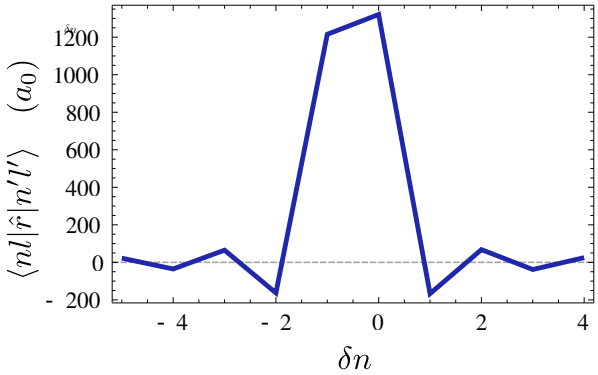

Figure 2.4: Radial matrix elements of the $|37S\rangle$-state of ^{87}Rb to adjacent $|n'P\rangle$-states. Shown are the radial matrix elements of the $|n = 37, l = 0\rangle$-state to neighbouring $|n', l' = 1\rangle$-states. The radial matrix elements are largest for the $nS \to nP$ and $nS \to (n-1)P$ transitions. The remaining elements quickly drop off with $\delta n = n' - n$ as the wavefunction overlap rapidly decreases.

using approximate solutions like for instance effective Hamiltonians [Bij13] in which the far off-resonantly coupled pair states are adiabatically eliminated[3].

The exact position of the atomic energy levels and the resultant Förster defects of the pair states are crucial for the strength and nature of the interactions. Therefore the interactions are very specific for each element. In the experiment, we address S-states of ^{87}Rb. In the case where both atoms are in the same nS-state, the interaction between the atoms is almost always repulsive [Bij13]. This is convenient for the experiment, as attractive interactions lead to rapid collisional ionization of the atoms [Amt07] which leads to uncontrolled effects in the experiments.

Interstate $n_1S - n_2S$ interactions in ^{87}Rb

Fig. 2.5 shows a map of C_6-coefficient for interactions between n_1S- and n_2S-states which are calculated using an effective Hamiltonian [Bij13]. As one can see not all Rydberg states strongly interact. This can be understood from the result derived in the two-state approximation, that the strength of the Rydberg-Rydberg interactions is determined by the coupling strength V_0 and the Förster defect.

The dipolar coupling strength strongly depends on the dipole matrix elements $\mu = \langle nl|\,\hat{\boldsymbol{\mu}}\,|n'l'\rangle$ which reflect the wavefunction overlap of the two states. The amplitude of the dipole matrix elements is given by the radial matrix elements $\langle nl|\,\hat{r}\,|n'l'\rangle$ which are shown in Fig. 2.4 for the $|37S\rangle$-state of ^{87}Rb to neighbouring Rydberg states. Due to selection rules S-states are only coupled to P-states. The transitions $nS \to nP$ and $nS \to (n-1)P$ show the largest radial matrix elements which are on the order $(n^*)^2 a_0$ with a_0 the Bohr radius [Wal08]. The next largest matrix elements which occur

[3] This is similar to the adiabatic elimination of an intermediate level in an off-resonant two-photon excitation.

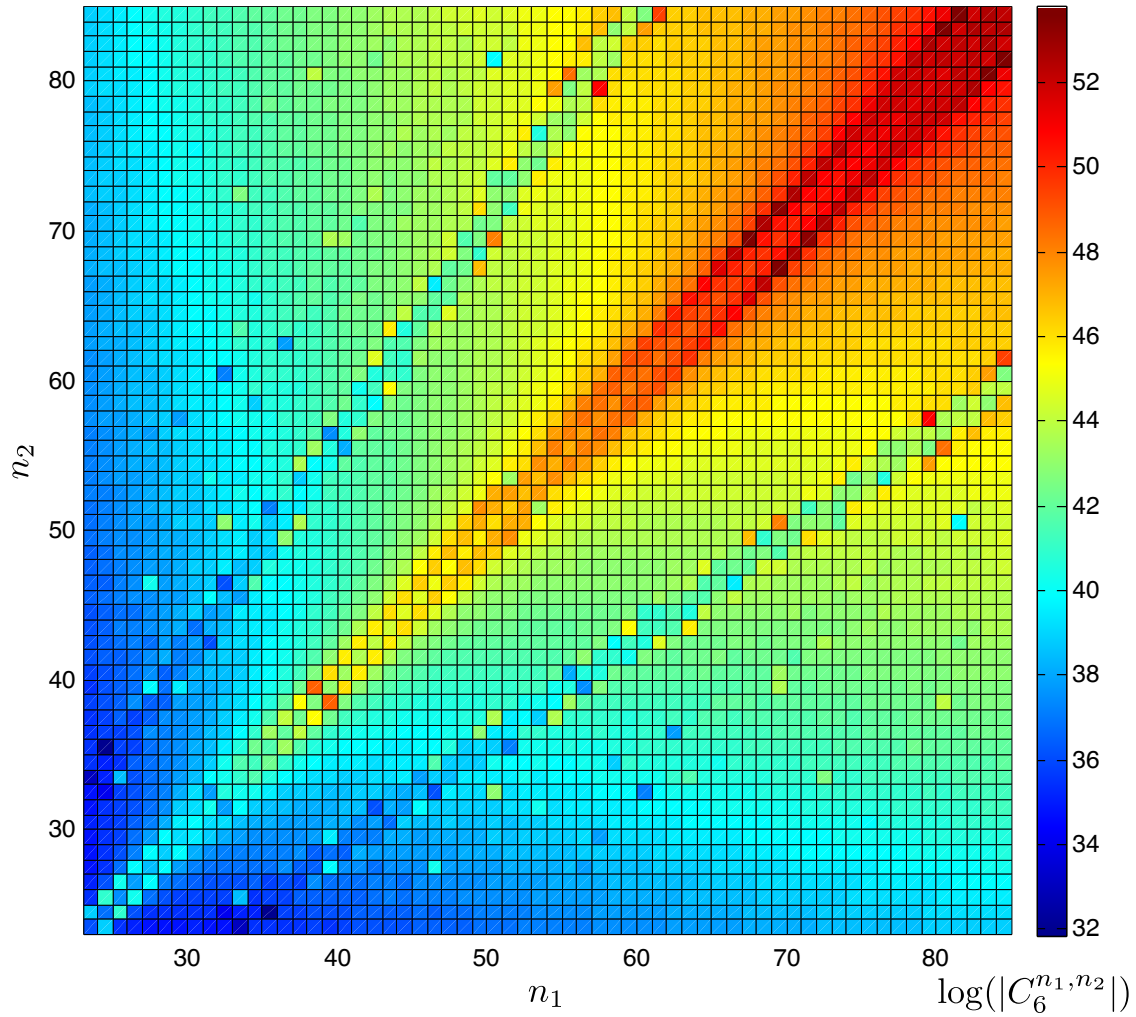

Figure 2.5: Map of interaction coefficients $C_6^{n_1,n_2}$ for $|s\rangle$-states of ^{87}Rb. Shown are calculated $|\log(C_6^{n_1,n_2})|$ for $|s\rangle$-states of ^{87}Rb using an effective Hamiltonian approach [Bij13]. The C_6-coefficients are given in atomic units ($E_h a_0^6/\hbar$ with E_h the Hartree energy). By courtesy of R.M.W. van Bijnen.

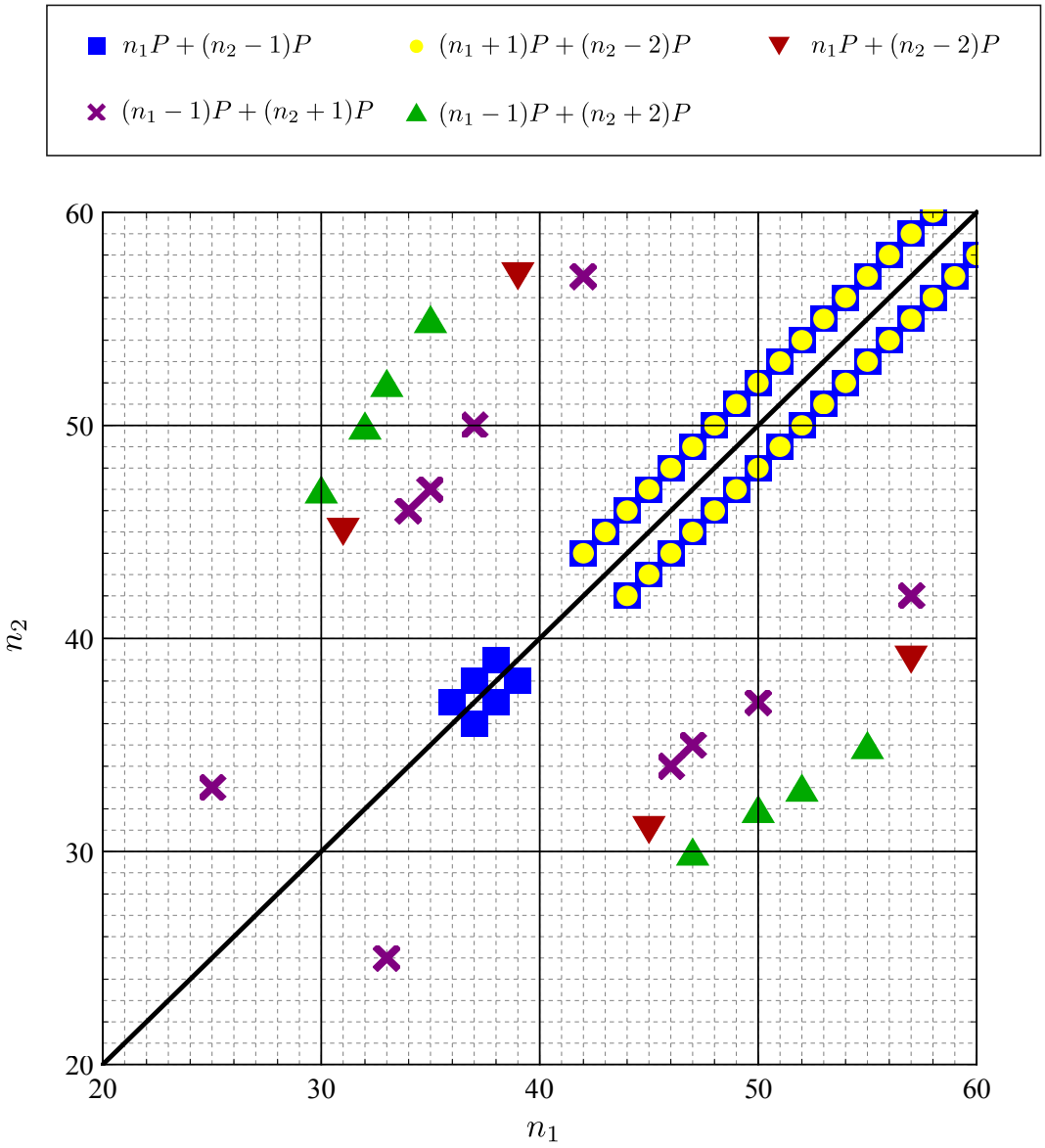

Figure 2.6: Interstate interaction resonances in ^{87}Rb atoms. Indicated are pairs $\{n_1S, n_2S\}$ that can be tuned into Förster resonance with electric fields $\leq 4\,\mathrm{V/cm}$ for $n = 20 - 60$ involving states with $\delta n = \pm 0, 1, 2$.

for $nS \rightarrow (n+1)P$ and $nS \rightarrow (n-2)P$ transitions are already roughly one order of magnitude smaller. As the remaining elements approximately fall off as δn^{-2} with $\delta n = n' - n$ the difference in the principal quantum number, we only need to consider the coupling of the following pair states

$$n_1S + n_2S \leftrightarrows n_1P + (n_2-1)P \tag{2.14a}$$
$$n_1S + n_2S \leftrightarrows n_1P + (n_2-2)P \tag{2.14b}$$
$$n_1S + n_2S \leftrightarrows (n_1-1)P + (n_2+2)P \tag{2.14c}$$
$$n_1S + n_2S \leftrightarrows (n_1+1)P + (n_2-2)P \tag{2.14d}$$
$$n_1S + n_2S \leftrightarrows (n_1-1)P + (n_2+2)P \tag{2.14e}$$
$$n_1S + n_2S \leftrightarrows (n_1-2)P + (n_2+2)P \tag{2.14f}$$

which are ordered in terms of coupling strength to explain the resonances in the interaction strength observed in Fig. 2.5.

In the experiments, we are interested in strong interstate interactions, i.e. $n_1 \neq n_2$; particularly in states with a Förster defect that can be tuned to zero using small electric fields ($\leq$4 V/cm) without the states crossing into the hydrogenic manifold. Investigating the Stark maps of the pair state combinations given above we identify the resonances shown in Fig. 2.6.

2.1.4 Rydberg atom-light interactions

The strong Rydberg-Rydberg interactions combined with the laser excitation naturally lead to correlations between the atoms and give rise to the so-called Rydberg blockade [Luk01, Saf10]. Extending the basic idea of the Rydberg blockade to systems containing many Rydberg excitations, has led to theoretical studies of intriguing many-body Rydberg states which exhibit long-range order [Wei08, Poh10, Sch10a, Bij11]. In the following, we focus on interaction effects in laser coupled two-level systems. Three-level systems which are the topic of this thesis will be addressed in Ch. 3. Here, we introduce the concept of the Rydberg blockade and briefly discuss crystalline many-body Rydberg states.

Rydberg blockade

We consider the laser excitation of two atoms with the excitation resonant to the ground-to-Rydberg transition and an excitation bandwidth of $\mathcal{W}$ as depicted in Fig.2.7 (a). The interaction of the two atoms in the Rydberg state induces a level-shift U of the doubly excited state $|rr\rangle$ that depends on the separation R of the two atoms. For large separations both atoms can be excited to the Rydberg state. Conversely, for small distances the interaction shift U exceeds the excitation linewidth $\mathcal{W}$ which inhibits the excitation of close-by pairs. This leads to an excitation blockade as only a single atom

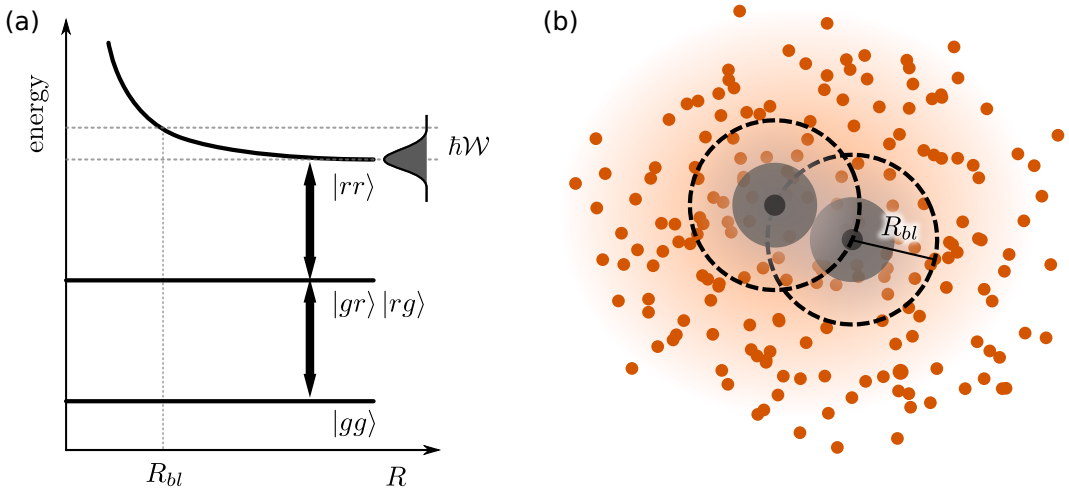

Figure 2.7: Rydberg blockade effect. (a) Two-atom blockade. For large distance R between the two atoms, both atoms can be excited to the Rydberg state. In contrast, for separations of the atoms smaller than R_{bl} the interactions shift the doubly excited state $|rr\rangle$ out of the excitation bandwidth $\mathcal{W}$ which blocks the excitation of close-by pairs. (b) Illustration of the blockade effect in an atomic cloud. In the case of resonant excitation and isotropic Rydberg-Rydberg interactions, the blockade leads to a blockade spheres (dashed line) around each Rydberg atom in which no further Rydberg atoms can be excited. Taken and adapted from [Hof13a].

can be excited. This can be formulated in the blockade condition

$$U \geq \hbar\mathcal{W}. \tag{2.15}$$

Since the natural lifetime of Rydberg-atoms scales with $(n^*)^3$, the excitation line-width is dominated by the power-broadening of the excitation and $\mathcal{W} \approx \Omega$ the Rabi-frequency. For isotropic interactions which is approximately true for van der Waals type interaction of nS-states [Wal08], the blockade volume is a sphere with a blockade radius of

$$R_{bl} = (C_6/\Omega)^{1/6} \tag{2.16}$$

as illustrated in Fig.2.7 (b). Angular dependent interactions lead to more complex volumes like ellipsoids or even show no blockade under certain angles [Saf10]. Since its proposal in 2001 by Lukin *et al.* [Luk01], the Rydberg blockade which leads to a saturation of the number of Rydberg excitations in the gas has been observed in many experiments for the different types of Rydberg-Rydberg interactions [Com10].

Collective atom-light interaction

The blockade and the concomitant reduction of accessible many-body states also leads to different dynamics in the system. We consider an ensemble of N atoms within a

blockade volume. Because of the blockade, only states containing a single Rydberg excitation can be accessed. As the light-field preserves the symmetry under particle exchange, the initial state with all the atoms in the ground state $|g^{(0)}\rangle$ solely couples to the totally symmetric Dicke-state $|R^{(1)}\rangle$

$$\left|R^{(1)}\right\rangle = \frac{1}{\sqrt{N}} \sum_{i=1}^{N} |g_1, ..., r_i, ..., g_N\rangle \,. \tag{2.17}$$

Therefore, the interaction of the entire atomic ensemble with the light field can be reduced to an effective two-level system with a collective Rabi-frequency $\Omega_{\text{col}} = \sqrt{N}\Omega$ which is enhanced by a factor $\sqrt{N}$ compared to the single atom Rabi-frequency Ω. This collective enhancement of the Rabi-frequency was experimentally observed for two atoms [Gae09] and indirect evidence was seen in large samples [Hei07]. As the ensemble of atoms within one blockade volume acts like a simple two-level atom but with enhanced coupling to the light field, it is sometimes referred to as a superatom [Vul06].

The enhanced coupling to the light field of a blockaded ensemble also affects the blockade. The enlarged Rabi-frequency increases the power-broading and we replace $\Omega \to \sqrt{N_{bl}}\Omega$ in Eq. (2.16) to define a superatom blockade radius

$$R_{bl} = \left(\frac{C_6}{\sqrt{N_{bl}}\Omega}\right)^{1/6} . \tag{2.18}$$

where $N_{bl} = n_a \times 4/3\pi R_{bl}^3$ is the number of atoms in the blockade volume and Eq. (2.18) needs to be solved self-consistently. The density dependent broadening of the excitation bandwidth leads to a decrease in the blockade radius for increasing atomic densities. A thorough definition of the blockade radius in a many-body system is difficult, since it depends on the specific arrangement of the atoms. Nonetheless, the given simple ad-hoc definition of the superatom blockade radius based on the partition of the cloud in terms of superatoms is in good agreement with many-body simulations [Rob05] and reproduces the experimentally observed scaling of the blockade radius with the atomic density [Hei07].

Crystalline many-body Rydberg states

The first experimental observations of the Rydberg blockade [Ton04, Sin04] in 2004 have triggered intense theoretical studies of many-body Rydberg states. Starting from the simple blockade picture outlined above, naturally the question arises how the superatoms are arranged within the atomic gas and whether there are ways to create spatially ordered states of Rydberg atoms.

In 2005 Robicheaux and Hernández predicted that the blockade can give rise to spatial many-body correlations in an disordered gas [Rob05], hinting already to spatially ordered states. A few years later, Weimer *et al.* investigated the ground-state properties

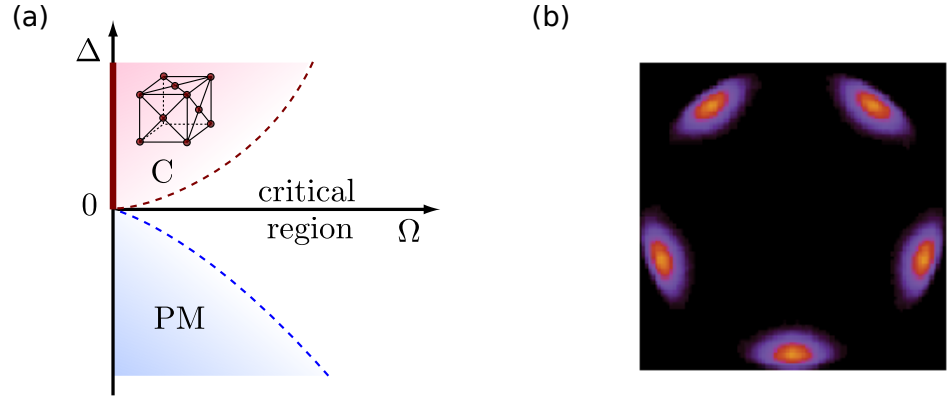

Figure 2.8: Crystalline many-body Rydberg states. (a) Schematic phase-diagram of atoms continuously coupled to interacting Rydberg states. The ground-state of this coupled system depends on the laser detuning Δ and the Rabi-frequency Ω. Going from negative to positive detuning the system undergoes a quantum phase transition from a disordered gas of ground-state atoms (PM) to a crystalline state of Rydberg-excitations (C). Taken from [Wei08]. (b) Simulated probability distribution of an adiabatically prepared two-dimensional Rydberg crystal. Taken from [Poh10].

of atoms under continuous laser coupling to Rydberg states [Wei08]. They discovered that this coupled light-matter system exhibits a second order quantum phase-transition which belongs to an unprecedented universality class. Varying the laser detuning, the system undergoes a transition from a disordered gas of ground-state atoms, to a state containing regularly spaced Rydberg excitations (see Fig. 2.8 (a)). Still the open question remained how the system can reach its ground-state. Shortly after, Pohl *et al.* proposed to prepare crystalline Rydberg states by dynamical crystallization of Rydberg excitations [Poh10]. As the crystalline arrangement of the Rydberg atoms minimizes the interaction energy, these states can be prepared by adiabatically following the ground-state of the system. Yet, so far these so-called "Rydberg crystals" have been elusive and remain an ongoing experimental challenge.

2.2 Ultracold Rydberg atoms in dense atomic samples

To investigate the interplay of light with strongly interacting ultracold Rydberg gases, a new experimental apparatus was designed and built with the following design criteria in mind:

Low temperature: To study effects of interactions and resulting many-body Rydberg states, we want the atoms to "stand still" during the course of the experiment to avoid mixing with motional degrees of freedom. Therefore ultracold atomic clouds offer an ideal starting ground. At a temperature of $1\,\mu$K the atoms move with a velocity of $\approx 15\,\mathrm{nm}/\mu\mathrm{s}$. This thermal motion of the atoms is negligible on the time scale of the experimental interrogation on the order of few tens of microseconds.

High atomic density: The interatomic separation scales with the atomic density n_a like $n_a^{-1/3}$. Hence, the role of interactions is effectively density dependent. The strongly interacting regime is characterized by $n_a R_{bl}^3 > 1$ [Löw12]. With blockade radii R_{bl} on the order of a few micrometers, we require densities of $1\,\mu\mathrm{m}^{-3}$ or higher. Furthermore, to study the transition from the non-interacting to the interacting regime tunability of the density over several order of magnitude is required.

Electric field control: Rydberg atoms experience large DC-Stark shifts due to their enormous polarizability (cf. Sec. 2.1.2). For instance, the state $|55S_{1/2}\rangle$ has a polarizability $\alpha \approx -100\,\mathrm{MHz}/(\mathrm{V/cm^2})^2$, while the lifetime limited transition width is only $\approx 30\,\mathrm{kHz}$ [Bet09]. Therefore, already small electric fields of $\mathcal{E} \approx 1\,\mathrm{V/cm}$ can shift Rydberg states by several hundred linewidths. On the one hand side, it outlines the need to compensate stray fields, that might be caused by a few spurious ions [Com10]. On the other hand, this can be employed to manipulate properties of the Rydberg state, like Förster tuning of interactions (cf. Sec. 2.1.3) or spatially resolved excitation in inhomogeneous fields [Mül07].

Good optical access: Interfacing light with the ultracold atomic cloud is at the heart of the presented experiments. For instance, addressing and imaging the atoms with high spatial resolution is an important ingredient for the new imaging method presented in Ch. 5. Additionally, a high degree of optical access allows us to implement optical dipole traps for fast evaporative cooling and control of the dimensionality of the atomic cloud.

Fast duty cycles: Short cycle times on the order of a few seconds allow to quickly scan large parameter ranges and enable to achieve good statistics in the measurements. In addition, it poses less stringent conditions on the long-term stability and facilitates the adjustment of the experiment.

In the following, we will outline the key features of the new apparatus. More details can be found in a recent PhD thesis [Hof13a] as well as Master theses [Mül10, Bus11, Fab11]. The main ingredients of the experimental setup are shown in Fig. 2.9.

2.2.1 Preparation of dense ultracold atomic samples

Cooling atoms to temperatures close to absolute zero is a standard task in modern ultracold experiments. Typically, the atoms are laser cooled and trapped inside an ultra-high vacuum (UHV) chamber, to isolate them from the environment. The applied laser cooling and trapping techniques are well established and their principles are explained in detail in [Ket99] and [Met07].

The vacuum system employed in our experiments is shown in Fig. 2.10 (a). Rubidium vapor inside the vacuum chamber is supplied by dispensers. The cooling of the atoms is performed in two stages: we apply dissipative precooling in a two dimensional magneto-optical trap (2D-MOT) followed by further cooling and in a three-dimensional magneto-optical trap (3D-MOT). In the second cooling stage, the atoms are transferred into a conservative potential provided by an optical dipole trap. In the dipole trap, evaporative cooling is used to further lower the temperature and increase the density of the atomic cloud which allows us to achieve Bose-Einstein condensation if required.

The experiments with Rydberg atoms happen on the microsecond time-scale, limited by the lifetime of the Rydberg atoms [Löw12] and collisional ionization [Amt10]. Therefore, to obtain short experimental cycle times, the preparation of the dense ultracold atomic sample has to be fast. The cooling cycle which allows us to achieve cycle times of a few seconds is outlined in the following.

(i) **Cold atom source:** We use a 2D-MOT in a glass cell, that is pressure separated by a differential pumping tube from the main chamber, as our cold atom source. The design and performance of the 2D-MOT is described in detail in [Hof13a]. In Rydberg experiments, care has to be taken to avoid unwanted effects of spurious ions in the vicinity of the atoms. The 2D-MOT provides an ion free cold atom source, since the cooling mechanism and the transmission through the differential pumping tube exclusively work for the specific neutral atomic species. Our compact and modular 2D-MOT provides an atom beam with a high flux of up to 3.9×10^9 atoms/s and a small divergence, such that under optimal conditions a MOT with about 3×10^8 atoms is loaded within 0.2 s. Another advantage of the 2D-MOT is, that its orientation with respect to the MOT-field gradient is unrestricted compared to e.g. Zeeman-slowers, which is beneficial for maximizing optical access.

(ii) **3D-MOT:** Our 3D-MOT is comprised out of six beams of superimposed cooling and repumping light with a $1/e^2$ diameter of 20 mm and two water cooled coils outside the vacuum chamber. This provides us with a large trapping volume. The cooling light with a total cooling power of 125 mW is red detuned from the cooling transition $|5S_{1/2}, F = 2\rangle \rightarrow |5P_{3/2}, F = 3\rangle$ by 19 MHz ($\sim 3\,\Gamma_e$ with Γ_e the decay rate of the $5P_{3/2}$-state). The repumping light is resonant with the $|5S_{1/2}, F = 1\rangle \rightarrow |5P_{3/2}, F = 2\rangle$ transition and has a total power of 140 μW. For the MOT, we apply a magnetic field gradient of 10.5 G/cm. The loading of the 3D-MOT, during which the dipole trap is already switched on, is followed

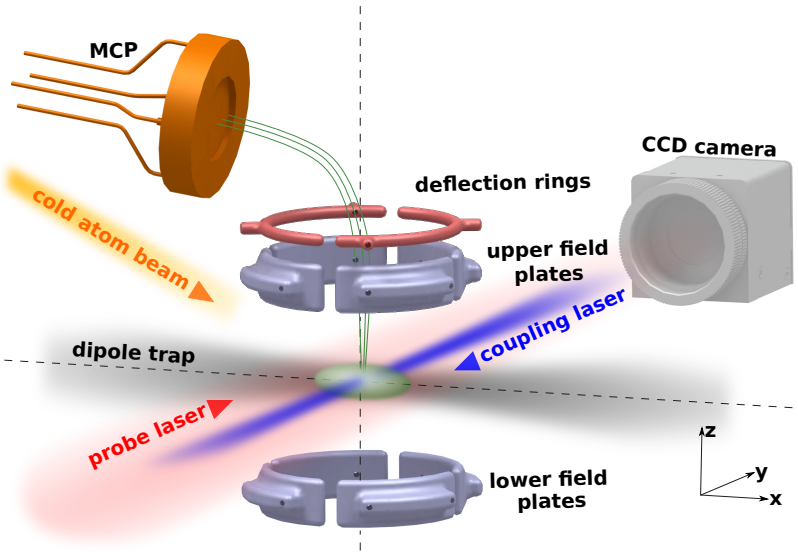

Figure 2.9: Schematic of the experimental setup. A two-dimensional magneto-optical trap (MOT) (not shown) provides a high flux cold atom beam which we use to load the 3D-MOT (not shown). The trapped and pre-cooled atoms (green ellipse) are subsequently transferred into an optical dipole trap for evaporative cooling. After trap release, the atoms are excited to high-lying Rydberg states by a 780 nm probe laser and a counter-propagating 480 nm coupling laser. An electrode structure (lower and upper field plates) is used for precise electric field control and for field ionization of Rydberg atoms. Guiding fields produced by two deflection rings direct the resulting ions (green trajectories) onto a micro-channel plate (MCP) detector. In parallel, optical detection with a CCD camera provides complementary information using Rydberg-EIT. Taken and adapted from [Hof13a]

by a compression and a dark-MOT phase to increase the density and to improve the loading into the dipole trap. In the compressed MOT, the magnetic field gradient and the detuning of the cooling light are increased in 200 ms to 14 G/cm and 25 MHz, respectively. Afterwards, in the dark-MOT phase at fixed magnetic field gradient the total cooling power is decreased down to 11 mW, the repumping power is lowered to 1 μW and simultaneously the cooler detuning is ramped to 48 MHz. To suppress atom loss because of hyperfine changing collisions in the dipole trap, in a last step the atoms are optically pumped into the $F = 1$ hyperfine manifold. This is done by turning off the repumper 2 ms before the MOT is completely switched off.

(iii) **Dipole trap:** In order to precisely control the density and temperature of the atoms and to produce Bose-Einstein condensates (BECs), we use an all-optical evaporation scheme. Compared to magneto-static traps [Löw12, Dub12], optical dipole traps are unrestricted to the used spin states and allow for almost instant trap switch-off. Furthermore, they minimally affect the optical access to the

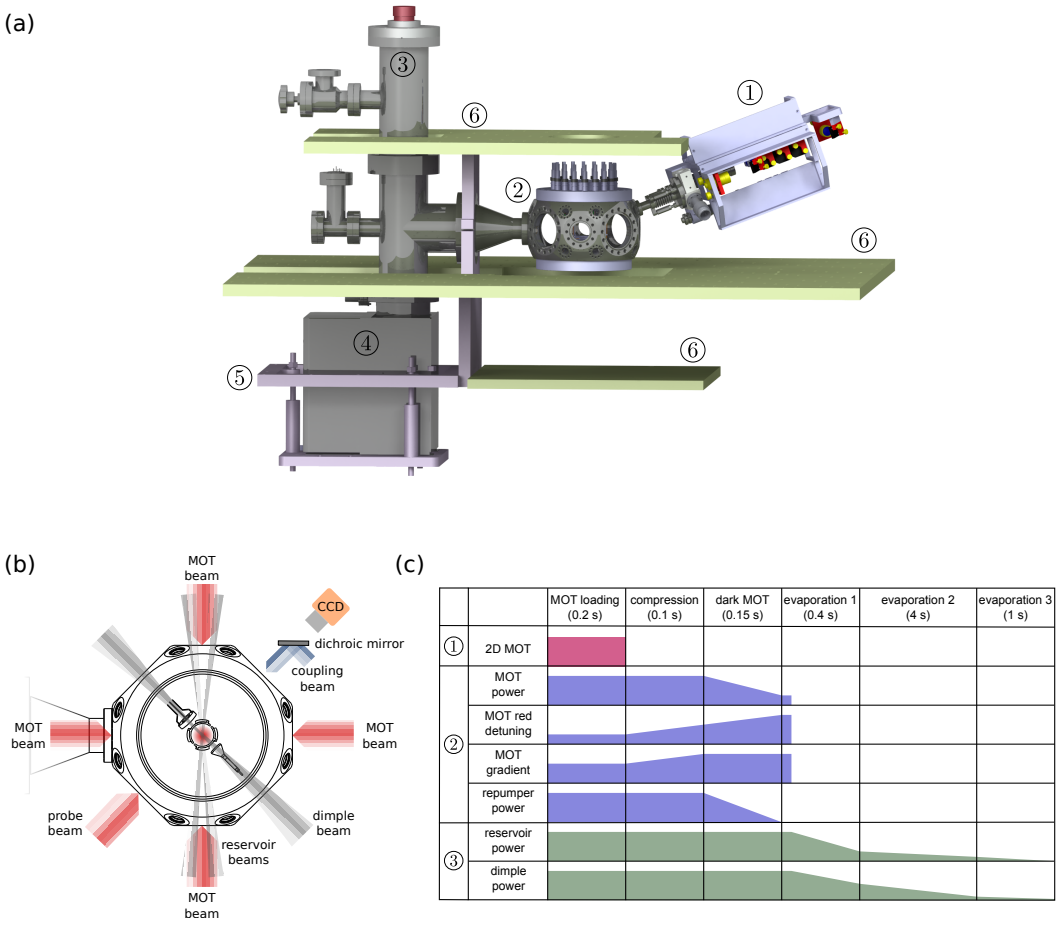

Figure 2.10: Experimental setup and cooling cycle. (a) Vacuum system including periphery. The apparatus has a dual chamber vacuum design with a modular 2D-MOT (1) as a cold atom source which is pressure separated from the science chamber the science chamber (2). For pumping a titan sublimation pump (3) and a 125 l ion pump (4) are used. A mounting structure (5) is recessed into the optical table (not shown) and supports the entire setup. Optical breadboards (6) are used to mount optical elements. (b) Top view on the science chamber illustrating the beam geometry. Three mutually orthogonal pairs of counter propagating beams (MOT beams) at 780 nm are used to realize a 3D-MOT. Two reservoir beams and a dimple beam form the dipole trap ($\lambda = 1064\,\mathrm{nm}$). The probe ($\lambda = 780\,\mathrm{nm}$) and the coupling ($\lambda = 480\,\mathrm{nm}$) laser are counter aligned using a dichroic mirror and propagate perpendicular to the dimple beam. The probe light is detected on a CCD camera. Optical elements are not shown for clarity. (c) Typical experimental cycle for the preparation of dense ultracold gases. Taken and adapted from [Hof13a]

atoms and their operation is technically less demanding than hybrid optical and magnetic traps. To combine a large volume trap for efficient loading from the 3D-MOT with tight confinement for fast evaporation, we employ a three beam optical dipole trap [Fab11]. As shown in Fig. 2.10 (b), two large beams cross under a small angle and form a large volume reservoir. Superimposed is a tightly focused "dimple" beam, that ensures high collision rates during evaporation and allows for fast evaporation ramps. Thus, the three beam geometry allows us to decouple the loading from the evaporation process. The dipole trap light is derived from a 50 W single frequency laser[4] at 1064 nm, resulting in a power of about 25 W on the atoms. The reservoir beams are generated by imaging the Bragg diffraction pattern of an acusto-optical modulator (AOM) onto the atoms. The two horizontally polarized beams have a waist of 120 μm, cross under an angle of 5.4° and are frequency shifted with respect to each other by $\nu_{AOM} \approx 80$ MHz to avoid beam interference. With a total power of about 21.5 W, the reservoir generates an optical potential with a depth $U_{res} = k_B \times 145\,\mu$K. Compared to a single beam trap with the same total power, the crossed trap design leads to a tighter confinement along the long axis of the trap, which significantly improves the loading [Fab11]. The vertically polarized dimple beam is focused down to 23 μm and crosses the reservoir under 45° with respect to the symmetry axes of the reservoir. With a typical power of 2 W, the dimple increases the potential depth by $U_{dimple} = k_B \times 350\mu$K, which results in a transfer of a large fraction of the atoms trapped in the reservoir into the dimple for the evaporation process.

From the MOT we transfer about 5×10^6 atoms into the optimized three beam trap. After 40-50 ms of plain evaporation, we start the forced evaporation by ramping down the power of the reservoir and the dimple. Depending on the experiment and the required densities and temperatures the evaporation sequence is adjusted. To achieve the highest densities and Bose-Einstein condensation the evaporation is performed in three stages with exponential decrease of the laser power. Typically, we reach the BEC transition at a critical temperature of $T_c = 260$ nK with about 10^5 atoms [Hof13a].

Whereas, Bose-Einstein condensation is not required in most of the experiments, the flexibility to change the dimensionality of the cloud is an important feature of the experiment. Loading atoms into the reservoir we can produce three dimensional ultracold atomic clouds. Switching to the dimple highly elongated clouds with an radial extend of only a few micrometers or less can be trapped which enables to create 1D-samples with respect to the Rydberg excitation.

[4] In the early stage of the experiment the 50 W were provided by a single frequency solid-state laser with 1 W, that was amplified using a fiber amplifier. Due to problems with the beam profile of the fiber amplifier, this system was replaced by a single-frequency solid-state-laser with 55 W output power.

Fig. 2.10 (c) summarizes a typical experimental cycle. Optimizing the sequence for the fastest duty cycle, we reach Bose-Einstein condensation with a cycle time down to 4.5 s. These fast duty cycles set the basis for the experiments detailed in following chapters.

State preparation

To precisely control the interplay between the light field and the atoms, we prepare the atoms in a well-defined initial state. Combined with suitable laser polarizations, this allows us to realize well-defined three-level or respectively two-level system despite the complex level structure of ^{87}Rb in the experiments (see Fig. 2.11). After reaching the final trap depth, we turn on microwave radiation resonant with the stretched $|5S_{1/2}, F = 1, m_F = 1\rangle \rightarrow |5P_{3/2}, F = 2, m_F = 2\rangle$ transition at a magnetic field of 2.9 G. The microwave radiation, which is blue detuned with respect to the transition at the initial magnetic field of 2.7 G, is emitted from one of the deflection rings of our electrode structure inside the vacuum chamber. In 100 ms we slowly ramp the magnetic field over the resonance to 3.1 G thereby adiabatically transferring the atoms in the state $|5S_{1/2}, F = 1, m_F = 1\rangle$ in a Landau-Zener sweep to the state $|5P_{3/2}, F = 2, m_F = 2\rangle$, which serves as the initial atomic state $|g\rangle$ in the experiments. With an energy splitting of about $h \times 6.8$ GHz of the $F = 2$ and $F = 1$ manifold, the atoms left in the other magnetic sublevels of the $F = 1$ manifold are far off-resonant to the light fields and do not take part in the investigated light-matter phenomena.

Atomic density tuning

Another important aspect for the investigation of interaction effects in the coupled light-matter system is the accurate tuning of the atomic density. To tune the atomic density, we let the atomic cloud ballistically expand after releasing the atoms from the trap. This allows us to bridge four orders of magnitude in density in the experiment. Alternatively, the atomic density can be tuned varying the transfer time in the microwave transfer. This is sometimes beneficial, as it permits to keep a constant time-of-flight and the excitation volume remains the same for all investigated densities.

2.2.2 Rydberg excitation and detection

After releasing the atoms from the optical trap, we investigate their interplay with the light fields in which they are excited to Rydberg states. After the interrogation with the light fields, which can be employed for optical detection of Rydberg state (cf. Ch. 3), we probe the Rydberg state population using field ionization of the Rydberg atoms.

Rydberg excitation

We excite the atoms to Rydberg states either using a direct two-photon excitation far detuned from the intermediate state or by coupling to Rydberg states under EIT

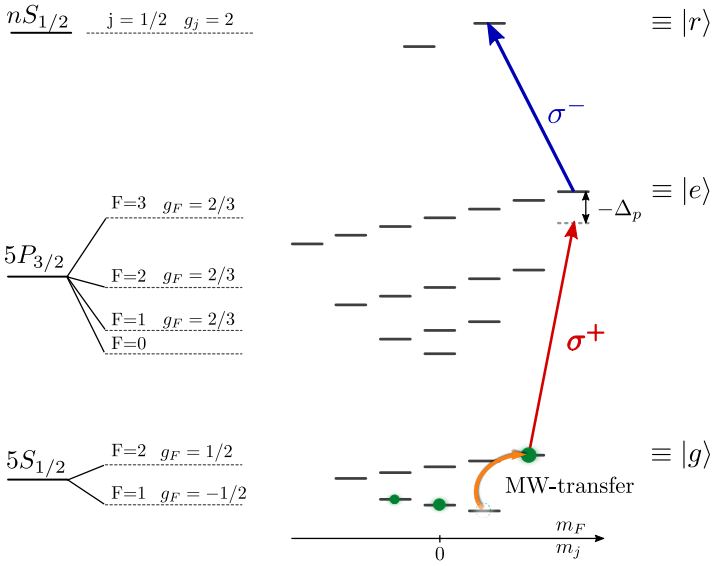

Figure 2.11: State preparation and realizing a three-level system in ^{87}Rb. Shown are the states of the $5S_{1/2}$ and the $5P_{3/2}$-manifold as well as the Rydberg states, that are coupled by the laser fields. After the evaporation the atoms are distributed over the $F = 1$ manifold. Using microwave (MW) transfer, the atoms in the state $|5S_{1/2}, F = 1, m_F = 1\rangle$ are transferred in the initial state $|5P_{3/2}, F = 2, m_F = 2\rangle$ for the EIT experiments. The probe and coupling beams, which are σ^+ and σ^- polarized respectively, thus only couple three levels of the ^{87}Rb atoms.

conditions which is discussed in Ch. 3. The two laser beams called probe and coupling beam are counter-aligned as shown in Fig. 2.10. The probe field with a wavelength of 780 nm couples the atoms to the intermediate $5P_{3/2}$-state and the coupling laser with a wavelength of 480 nm further promotes them to the Rydberg states. The excitation process and the involved states are shown in Fig. 2.11. Due to selection rules, the σ^+ polarized probe light only drives the transition $|g\rangle \equiv |5S_{1/2}, F = 2, m_F = 2\rangle \leftrightarrow |e\rangle \equiv |5P_{3/2}, F = 3, m_F = 3\rangle$. Likewise, the σ^- polarized coupling beam only couples to the Rydberg state $|r\rangle \equiv |nS_{1/2}, j = 1/2, m_j = 1/2\rangle$, realizing a well-define three-level system.

Electric field control

Controlling the electric field landscape at the position of the atoms is one of the challenges in experiments involving Rydberg atoms. To accomplish this task, a stainless steel electrode assembly - the *Rydberg detector* - is placed inside the vacuum chamber. Its design gives full optical access to the atoms which allows us to readily interface the atoms and the light field or to implement optical lattices. Design considerations and further technical details on the Rydberg detector are given in [Mül10] and [Hof13a]. In the experiment, the Rydberg detector accomplishes the following tasks:

- *Stray field compensation*: The dominant stray field in the experiment is due to residual fields of the charge particle detectors. In a first attempt, this stray field has been compensated using optical detection of the $50S$-Rydberg state. By comparing the EIT-resonance position (cf. Sec. 3.1.3) with and without the MCP on, the field plate voltages were adjusted until the two resonance positions matched. The residual field was measured to be $\lesssim 80$ mV/cm [Arg13]. Addressing Rydberg states with higher principal quantum numbers this can readily be improved. According to simulations the electrodes should allow for field compensation in a volume of $1\,\mathrm{mm}^{-3}$ down to 5 mV/cm [Mül10].

- *Application of precisely controlled homogeneous fields:* For Stark-tuning of the Rydberg states or Förster-tuning of the interactions (cf. Sec. 2.1.3) respectively, homogeneous electric fields are applied. Accounting for the grounded vacuum chamber and the exact wiring of all the electrodes, the simulated deviations in the electric field only amount to 0.5 % in a volume of $1\,\mathrm{mm}^3$ [Mül10]. The detector furthermore allows to generate homogeneous electric field gradients which allows to address different parts of the atomic cloud spatially resolved.

- *Application of large electric fields:* To ionize the Rydberg atoms we switch to electric field of a few 100 V/cm. These fields can in principle be ramped to achieve state-selective detection of the Rydberg atoms.

A schematic of the Rydberg detector is shown in Fig. 2.12 (a). The electrode assembly is mounted on a DN160CF to DN63CF reducing flange with 18 SHV connections (not shown in the figure). Attached to the reducing flange is a grounded holding structure, that supports ten individually addressable electrodes. The electrodes are divided in two deflection rings, that are used to guide the ions to one of the charged particle detectors, and eight field plates to control and manipulate the electric field at the position of the atom cloud.

Respectively, four field plates form a segmented cylinder above (3) and below (4) the atoms with an inner radius of 15 mm, 8 mm height and 2 mm thickness. The two segmented cylinders are separated by 28 mm. The cylindrical design and the position of the field plates were chosen to minimize field inhomogeneities. Simulations of different field plate geometries show that a prolate geometry allows for the best field homogeneity and gradient uniformity in the z-direction [Mül10].

The electric potentials on the field plates and hence the electric field at the position of the atom are controlled using bipolar voltage switches with an effective rise time of ∼100 ns. A low noise voltage supply[5] delivers voltages up to 3 kV . The half-ring shaped deflection rings (2) above the field plates are used to bend the ions that are produce in the field ionization process on a curved trajectory to either a micro-channel plate detector (MCP, (5)) and channel electron multiplier (CEM,(6)). The two detectors are

[5]WIENER MPOD-HV/LV with specified voltage ripples $< 2mV$ and $< 10mV$ peak-to-peak for the low and high voltage modules, respectively.

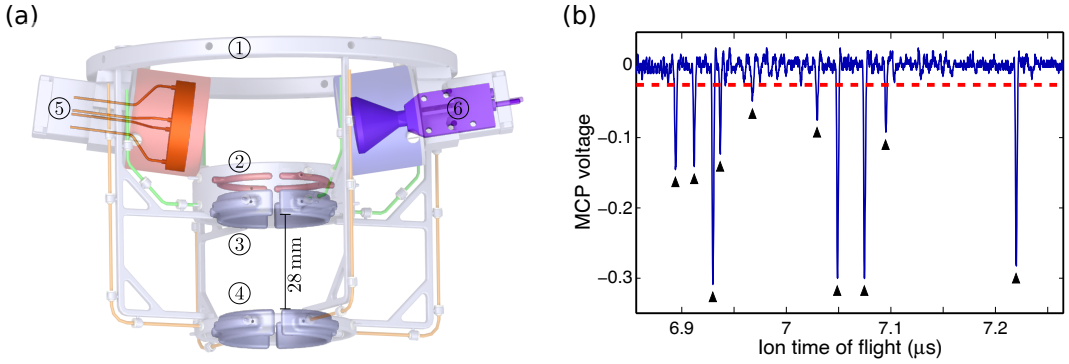

Figure 2.12: Electrode assembly for electric field control and for field ionization and detection of Rydberg atoms. (a) Schematic drawing of the electrode assembly. A grounded supporting structure (1) holds two deflection rings (2) as well as four upper (3) and four lower (4) field plates. The field plates are used to control the electric field at the position of the atoms. Charged particle detection is accomplished with either a micro-channel plate (MCP) (5) or a channel electron multiplier (CEM) (6) detector. Taken and adapted from [Hof13a]. (b) Typical ion trace for small numbers of Rydberg atoms. Detection events of individual ions are clearly identified (marked by black triangles). Voltage spikes below -0.02 V, are identified as an detected ion.

mirror-symmetrically situated above the electrodes and have a circular detection area of 165 mm^2. To minimize stray fields due to their bias voltage of $\simeq 2\,\mathrm{kV}$, both detectors are placed inside Faraday-cages.

Rydberg detection by ionization

Already moderate electric fields allow to ionize Rydberg atoms (cf. Sec. 2.1.2). This allows to detect Rydberg atoms by field ionization combined with consecutive charged particle detection. Since the ionization field is state dependent, this also allows for a state-selective detection of the Rydberg atoms.

In the experimental setup, fields up to $\mathcal{E} = 1.2\,\mathrm{kV/cm}$ can be applied, allowing to ionize Rydberg states from $n = 25$ ($\mathcal{E}_{ion} \simeq 1\,\mathrm{kV}$) to the continuum. In the presented experiments, the field ions are detected using a MCP and the resulting currents are recorded on a fast oscilloscope with a time resolution of 0.1 ns. Depending on the ion density, different methods are applied to analyse the ion traces. For large ion numbers n_{ion} - typically $n_{ion} > 20$ - the voltage spikes produced by the ions partially overlap. Therefore, under these conditions the ion traces are integrated, yielding a signal proportional to the ion number. For small ion numbers individual voltage spikes are clearly resolved above the background noise level of the ion traces as shown in Fig. 2.12 (b), showing that the apparatus is sensitive to individual Rydberg atoms. To count the ions several methods can be used: for a quick analysis, simple peak-find algorithms

are applied. For a more sophisticated analysis, a sparse spike deconvolution of the ion trace is employed. Further details on the different ion counting methods used in our experiment can be found in [Hof13a]. From the measured ion-pulse-height-distribution we infer a counting efficiency of 0.9, limited by the electrical noise. Combined with the MCP detection efficiency (≈ 0.6), the angular responsivity (≈ 0.9) and the guiding efficiency (≈ 0.9), this gives an estimated overall efficiency of $\eta \approx 0.4$.

3 Rydberg electromagnetically induced transparency

This chapter is based on the following publications:

Combined optical and population-based measurements of Rydberg electromagnetically induced transparency
C.S. Hofmann, G. Günter, H. Schempp, M. Robert-de-Saint-Vincent,
S. Whitlock, M. Weidemüller
in preparation

Sub-Poissonian Statistics of Rydberg-Interacting Dark-State Polaritons
C.S. Hofmann, G. Günter, H. Schempp, M. Robert-de-Saint-Vincent,
S. Whitlock, M. Weidemüller
Physical Review Letters **110,203601 (2013)**

The interaction of atoms with the electromagnetic field is at the heart of modern atomic and optical physics. In the presence of two coherent light fields intriguing effects such as electromagnetically induced transparency (EIT) or lasing without inversion arise. In EIT the presence of a strong coupling field renders the atoms, that are otherwise strongly absorbing, transparent to a weak probe field [Fle05]. At the few photon level, this phenomenon is characterized by the appearance of quasi-particles called dark-state polaritons, that are coupled excitations of the atoms and probe field. These hybrid quasi-particle simultaneously possess photonic and atomic properties, which can be tailored by the choice of the involved atomic states. This has been used, for instance, to slow down or even stop light [Hau99, Liu01, Phi01, Baj03], to imprint a magnetic moment onto light fields [Kar06], or to realize giant electro-optical effects in atomic vapours [Moh08]. New effects arise when coupling to strongly interacting atomic states. Here, we present a description of EIT including the effect of Rydberg-Rydberg interactions and experiments on EIT involving strongly interacting Rydberg states. The strong Rydberg-Rydberg interactions lead to effective polariton-polariton interactions, which we observe as an optical-nonlinearity in the transmitted probe light. In addition we find that the polariton interactions result in a narrowing of the statistical distribution of the number of polaritons, which reflects spatial and temporal correlations between the polaritons.

This chapter is structured as follows: First, we introduce a semi-classical approach to describe the interaction of light fields with non-interacting atoms and explain the origin of EIT. Then we present experiments on spatially resolved Rydberg-EIT in ultracold atomic clouds of ^{87}Rb with low atomic densities. In the low density regime, the effects of Rydberg interactions are negligible and the experiments are well captured by the semi-classical light-matter treatment. This allows us, based on the measured transmission spectra, to reconstruct the beam profile of the coupling beam at the position of the atoms as well as the Rydberg distribution in the atomic cloud. This serves as a valuable tool to characterize the system parameters in the experiments in the regime of strong Rydberg interactions.

3.1 Theory of electromagnetically induced transparency

Electromagnetically induced transparency (EIT) is a quantum interference effect which occurs in coherently driven three-level systems with two stable or metastable states and one rapidly decaying level. The destructive interference of different excitation pathways driven by the radiation fields leads to cancellation of absorption and renders the medium transparent. Since its theoretical proposal in the early 1990s and its first experimental realisation shortly after by Steven Harris and co-workers in hot Strontium vapor [Har90, Bol91], EIT has been realized in diverse physical systems ranging from atomic vapors [Bol91] over solids [Lon05] to atomic nuclei [Röh12].

Here we investigate EIT in an ultracold atomic gas of ^{87}Rb atoms. The two laser fields, which are referred to as the probe and coupling field, couple the ground $|g\rangle$ and first excited state $|e\rangle$ as well as a high-lying Rydberg state $|r\rangle$ of the atoms as schematically depicted in Fig. 3.1. The ground state of the atoms is stable and the Rydberg state with a life-time of several tens of microseconds is long-lived, whereas the first excited state rapidly decays with rate $\Gamma_e \sim 6\,\mathrm{MHz}$. The presence of the strong coupling on the upper transition induces an atomic coherence that cancels the absorption on the lower transition for the probe field. At the same time the gas exhibits a large dispersion that can be controlled and modified using the coupling field, which makes EIT an ideal light-matter interface.

To quantitatively describe this phenomenon we introduce a semi-classical treatment of the light field interacting with a quantum mechanical three-level system. Then we show how the quantum state of the three-level system is related to the optical response of the medium and how the coherence in the system can render the medium transparent to the radiation fields.

3.1.1 Light-matter interaction in a three-level system

To describe many features of the interplay between light and atoms, a semi-classical approach using a classical light field and a quantized atomic system is sufficient. Here, we consider a three-level atom with states $|g\rangle, |e\rangle$ and $|r\rangle$ in ladder configuration as

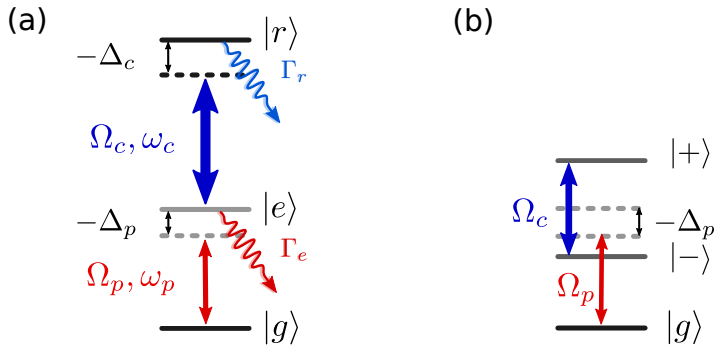

Figure 3.1: Three-level ladder system interacting with two coherent light fields. (a) The atomic states $|g\rangle, |e\rangle$ and $|r\rangle$ are near resonantly coupled by two coherent light fields, which are characterized by their frequencies $\omega_{p,c}$, Rabi-frequencies $\Omega_{p,c}$ and their detunings from the atomic transitions $\Delta_{p,c}$. The intermediate state $|e\rangle$ is rapidly decaying with rate Γ_e, whereas the upper state is long-lived with a decay rate Γ_r. (b) In the case of strong coupling Ω_c on the upper transition, it is convenient to use a dressed basis. Shown is the case for $\Delta_c = 0$ with the dressed states $|\pm\rangle = 1/\sqrt{2}\,(|r\rangle \pm |e\rangle)$.

depicted in Fig. 3.1. The states are coupled by two classical monochromatic light fields with electric fields $\boldsymbol{\mathcal{E}}_{p,c}(t) = \boldsymbol{\mathcal{E}}^{\mathbf{0}}_{\boldsymbol{p,c}} \cos(\omega_{p,c} t)$ at the position of the atom. The probe laser field near-resonantly drives the $|g\rangle \rightarrow |e\rangle$ transition with a frequency ω_p and is detuned from the atomic transition by $\Delta_p = \omega_p - \omega_{eg}$ where ω_{eg} is the transition frequency between the states $|g\rangle$ and $|e\rangle$. Similarly, the coupling laser acts on the $|e\rangle \rightarrow |r\rangle$ transition and is detuned by $\Delta_c = \omega_c - \omega_{re}$. The Hamiltonian that governs the evolution of the coupled atom-light system consists of two parts: $\hat{\mathcal{H}}_{atom}$ describes the atomic degrees of freedom whereas $\hat{\mathcal{H}}_{atom-light}$ accounts for the interaction of the atom with the light fields. Hence, one obtains

$$\hat{\mathcal{H}} = \hat{\mathcal{H}}_{atom} + \hat{\mathcal{H}}_{atom-light}. \tag{3.1}$$

We employ the dipole approximation[1] in which the atom-light interaction is given by $\hat{\mathcal{H}}_{atom-light} = -\hat{\boldsymbol{d}} \cdot \boldsymbol{\mathcal{E}}$, where $\hat{\boldsymbol{d}}$ is the electric dipole operator. Applying the rotating wave approximation and transforming to a rotating frame [Mar07], we obtain the time independent Hamiltonian

$$\hat{\mathcal{H}} = \frac{\hbar}{2} \begin{pmatrix} 0 & \Omega_p & 0 \\ \Omega_p & -2\Delta_p & \Omega_c \\ 0 & \Omega_c & -2(\Delta_p + \Delta_c) \end{pmatrix} \tag{3.2}$$

[1] Even though the Rydberg states have an extent on the order of 500 nm which is comparable to the wavelength this approximation is still valid. The transitions that we will consider always involve at least one tightly bound atomic state that has an extent much smaller than the wavelength.

given in the basis $|g\rangle = (1,0,0), |e\rangle = (0,1,0)$ and $|r\rangle = (0,0,1)$. The Rabi-frequencies $\Omega_{p,c}$ quantify the coupling strength on the probe and coupling transition, respectively, and are given by $\Omega_{p,c} = -\boldsymbol{\mathcal{E}}^{\mathbf{0}}_{\boldsymbol{p,c}}\boldsymbol{d}/\hbar$, with $\boldsymbol{\mathcal{E}}^{\mathbf{0}}_{\boldsymbol{p,c}}$ the amplitude of the corresponding electric field and $\boldsymbol{d}$ the dipole matrix element of the respective transition[2].

Decay of the intermediate state $|e\rangle$ leads to decoherence and a non-unitary evolution of the system. This can be incorporated employing the density matrix formalism which describes the time evolution of incoherent or open systems. The time evolution of the density matrix ρ which describes the quantum state of the atoms is governed by the Von Neumann equation [Scu97]

$$\dot{\rho} = -\frac{i}{\hbar}[\hat{\mathcal{H}}, \rho] + \mathcal{L}_{decay}(\rho) + \mathcal{L}_{laser}(\rho). \tag{3.3}$$

The effect of spontaneous decay and dephasing are incorporated using the Lindblad superoperators [Scu97]. The Lindblad operator

$$\mathcal{L}_{decay}(\rho) = -\frac{1}{2}\sum_k (C_k^\dagger C_k \rho + \rho C_k^\dagger C_k) + \sum_k C_k \rho C_k^\dagger \tag{3.4}$$

includes incoherent evolution due to spontaneous decay of the excited atomic states. The sum runs over all decay modes and the operators C_k describe the decay modes and their strength. The first term in the Lindblad operator introduces the decay of the coherences and the populations in the excited state, whilst the second term accounts for the additional population in the final state. For our three-level system $k = \{(ge), (er)\}$ and the decay operators are given by

$$C_{ge} = \sqrt{\Gamma_e}\,|g\rangle\langle e| \qquad \text{and} \qquad C_{er} = \sqrt{\Gamma_r}\,|e\rangle\langle r|\,, \tag{3.5}$$

where Γ_e and Γ_r denote the decay rates of the $|e\rangle$- and $|r\rangle$-state, respectively.

The light sources in the experiments are not perfectly monochromatic, but fluctuate around a central frequency. When the finite linewidth of the laser light is caused by phase fluctuations, the fluctuations in the laser frequency result in a decay of the atomic coherences, while the populations remain unchanged [Sul94, Fle05]. We can account for this effect using a phenomenological Lindblad operator $\mathcal{L}_{laser}(\rho) = -\gamma_{ij}/2 \cdot \rho_{ij}$, which describes the dephasing by a light field with a Lorentzian frequency spectrum with a full width half-maximum (FWHM) of γ_{ij}. With laser linewidths γ_p and γ_c for the probe and coupling laser, respectively, the Lindblad operator $\mathcal{L}_{laser}(\rho)$ reads

$$\mathcal{L}_{laser}(\rho) = -\frac{1}{2}\begin{pmatrix} 0 & \gamma_p\rho_{ge} & \gamma_{gr}\rho_{gr} \\ \gamma_p\rho_{eg} & 0 & \gamma_c\rho_{er} \\ \gamma_{gr}\rho_{rg} & \gamma_c\rho_{re} & 0 \end{pmatrix}. \tag{3.6}$$

[2]We only use real Rabi-frequencies here, as by unitary transformation the phase of a complex Rabi-frequency can be eliminated [Mar07].

For independently fluctuating probe and coupling lasers, the dephasing of the ground-to-Rydberg-coherence is given by the sum[3] of the two laser linewidths $\gamma_{gr} = \gamma_p + \gamma_c$. In the experiment the coupling laser is stabilized on the two-photon resonance in a thermal Rubidium vapor cell [Abe09] using the probe laser. Therefore, their frequency fluctuations can be correlated and the two-photon dephasing γ_{gr} can be smaller than the sum of the two linewidths.

Evaluating the Von Neumann equation with the given Lindblad operators leads to the optical Bloch-equations (OBEs):

$$\begin{aligned}
\dot{\rho}_{gg} &= -\Omega_p \,\mathrm{Im}[\rho_{\mathrm{ge}}] + \Gamma_e \rho_{ee} && \text{(3.7a)}\\
\dot{\rho}_{ee} &= \Omega_p \,\mathrm{Im}[\rho_{\mathrm{ge}}] - \Omega_c \,\mathrm{Im}[\rho_{\mathrm{er}}] - \Gamma_e \rho_{ee} + \Gamma_r \rho_{rr} && \text{(3.7b)}\\
\dot{\rho}_{rr} &= \Omega_c \,\mathrm{Im}[\rho_{\mathrm{er}}] - \Gamma_r \rho_{rr} && \text{(3.7c)}\\
\dot{\rho}_{ge} &= -\Gamma_{ge}\rho_{ge}/2 + i\,\Omega_c \rho_{gr}/2 + i\,\Omega_p(\rho_{gg} - \rho_{ee})/2 && \text{(3.7d)}\\
\dot{\rho}_{gr} &= -\Gamma_{gr}\rho_{rg}/2 - i\,(\Omega_p \rho_{er} - \Omega_c \rho_{ge})/2 && \text{(3.7e)}\\
\dot{\rho}_{er} &= -\Gamma_{er}\rho_{er}/2 - i\,(\Omega_c \rho_{rr} + \Omega_p \rho_{gr} - \Omega_c \rho_{ee})/2, && \text{(3.7f)}
\end{aligned}$$

where Im[x] denotes the imaginary part of x and we have defined the rates $\Gamma_{ge} = \Gamma_e + \gamma_p + 2i\Delta_p$, $\Gamma_{er} = \Gamma_e + \Gamma_r + \gamma_c + 2i\Delta_c$ and $\Gamma_{gr} = \Gamma_r + \gamma_{gr} + 2i(\Delta_p + \Delta_c)$.

3.1.2 Probe light propagation

To obtain the optical response of the gas, we have to relate the quantum state of the atoms to the polarizability of the gas. The incoming light fields induce a polarization in the atoms, which is reflected in their atomic coherences[4]. The microscopic state of the atoms is linked to the macroscopic polarisation of the gas by $\boldsymbol{P} = n_a \langle \hat{\boldsymbol{d}} \rangle = n_a \mathrm{Tr}[\rho \hat{\boldsymbol{d}}]$, where n_a is the the atomic density. Using Maxwell's equations allows us to derive the optical susceptibility [Pri11]

$$\chi(\Delta_p) = -\frac{2\, n_a \,|d_{eg}|^2}{\varepsilon_0 \hbar} \frac{\rho_{eg}}{\Omega_p} = -\chi_0 \frac{\Gamma_e}{\Omega_p} \rho_{eg}, \tag{3.8}$$

for a near resonant probe field where ε_0 denotes the vacuum permittivity. To separate the specific medium properties and the dependence of the susceptibility on the laser parameters, we have defined the constant $\chi_0 = \sigma_0 n_a / k$ with $\sigma_0 = 3\lambda^2/2\pi$ the resonant scattering cross-section and k the probe wave vector. With typical Rabi-frequencies of several MHz in the experiment, the atomic evolution reaches steady-state in less than a microsecond. This allows to work with the steady-state solutions of the OBEs in most cases.

[3] For two lasers that fluctuate independently of each other the linewidth of the two-photon transition is given by the convolution of the two laser line-profiles, resulting in a Lorentzian profile with a width given by the sum of the two Lorentzian laser linewidths.

[4] As the dipole operator only couples states with opposite parity, only superpositions of atomic states carry a dipole moment.

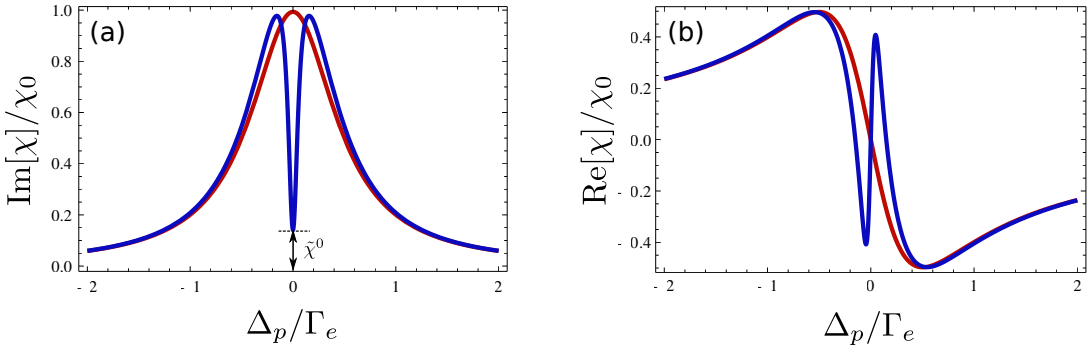

Figure 3.2: Three- and two-level susceptibility. Real (b) and imaginary (a) part of the rescaled susceptibility χ/χ_0 as a function of the probe laser detuning Δ_p in units of Γ_e. The susceptibility is obtained by the steady-state solution of the OBEs with $\Omega_c/\Gamma_e = 0.3$, $\Omega_p/\Gamma_e = 0.03$, $\Delta_c/\Gamma_e = 0$, $\Gamma_r/\Gamma_e = 0.005$ and laser linewdiths of $\gamma_p/\Gamma_e = \gamma_c/\Gamma_e = 0.005$ (blue curves). The laser linewidths lead to a finite absorption on two-photon resonance characterized by $\tilde{\chi}^0$. For comparison the red curve shows the susceptibility with the coupling beam off ($\Omega_c = 0$).

There are two important cases encountered in the experiment:

(i) Using the steady-solution for ρ_{eg} with the coupling beam off ($\Omega_c = 0$), we recover the well known Lorentzian profile for the lower transition

$$\chi_{2lvl}(\Delta_p) = \chi_0 \frac{i\Gamma_e\Gamma_{ge}}{2\Omega_p^2(\Gamma_e+\gamma_p)/\Gamma_e + |\Gamma_{ge}|^2} \tag{3.9a}$$

$$= \chi_0 \frac{\Gamma_e(-2\Delta_p + i(\Gamma_e+\gamma_p))}{\Omega_p^2(\Gamma_e+\gamma_p)/\Gamma_e + (\Gamma_e+\gamma_p)^2 + 4\Delta_p^2} \tag{3.9b}$$

(ii) In the presence of the coupling light the optical response of the gas changes dramatically. The imaginary part of the susceptibility shows a characteristic double peak structure and has a minimum for $\Delta_p = \Delta_c$ which corresponds to the EIT-resonance. In the case of weak probe light ($\Omega_p \ll \Omega_c, \Gamma$), we obtain the following analytic expression for the susceptibility

$$\chi_{3lvl}(\Delta_p) = \chi_0 \frac{i\,\Gamma_e\Gamma^*_{gr}}{\Gamma^*_{ge}\Gamma^*_{gr} + \Omega_c^2} \tag{3.10a}$$

$$= \chi_0 \frac{i\,\Gamma_e}{(\Gamma_e+\gamma_p-2i\Delta_p) + \frac{\Omega_c^2}{(\Gamma_r+\gamma_{gr}-2i(\Delta_p+\Delta_c))}}. \tag{3.10b}$$

The real and imaginary part of the susceptibility for the two cases as a function of the probe frequency are shown in Fig. 3.2. For the displayed susceptibilities, the coupling laser is chosen to be resonant to the upper transition.

In the experiment, we measure the transmission of the probe beam through the cloud. To calculate the transmission based on the local optical susceptibility, we propagate the incoming probe field through the cloud. Using the paraxial approximation and assuming a stationary probe field[5], we can work with the following simple equation for the amplitude $\mathcal{E}_p^0$ of the probe field

$$\frac{\partial}{\partial z}\mathcal{E}_p^0 = \frac{ik}{2}\chi(z)\mathcal{E}_p^0, \tag{3.11}$$

where z denotes the propagation direction. Looking at Eq.(3.11), one can see that the imaginary part of the susceptibility leads to absorption of the probe light, whereas the real part induces a phase shift. In the linear regime, where χ does not depend on Ω_p one can readily integrate Eq.(3.11) and obtain the transmission through the cloud

$$T = \frac{I}{I_0} = \exp\left(-\frac{\sigma_0\Gamma_e \mathrm{Im}[\rho_{\mathrm{eg}}]}{\Omega_p} n_{2D}\right) = \exp(-\mathrm{OD}) \tag{3.12}$$

where $n_{2D} = \int n_a(z)dz$ is the two-dimensional column density and OD the optical density.

3.1.3 Electromagnetically induced transparency resonance

To further understand how a three-level system exposed to two coherent light fields can be rendered transparent, we investigate the eigenstates of the coupled light-matter system on two-photon resonance ($\Delta_p + \Delta_c = 0$) [Fle05]

$$|+\rangle = \sin\theta\sin\phi\,|g\rangle + \cos\phi\,|e\rangle + \cos\theta\sin\phi\,|r\rangle\,, \tag{3.13a}$$
$$|-\rangle = \sin\theta\cos\phi\,|g\rangle - \sin\phi\,|e\rangle + \cos\theta\cos\phi\,|r\rangle\,, \tag{3.13b}$$
$$|D\rangle = \cos\theta\,|g\rangle - \sin\theta\,|r\rangle\,, \tag{3.13c}$$

where the mixing angles θ and ϕ are defined as

$$\tan\theta = \frac{\Omega_p}{\Omega_c} \qquad \text{and} \qquad \tan 2\phi = \frac{\sqrt{\Omega_\mathrm{p}^2 + \Omega_\mathrm{c}^2}}{\Delta_\mathrm{p}}. \tag{3.14}$$

Notably, the eigenstate $|D\rangle$ does not contain the excited state $|e\rangle$ and is thus immune to spontaneous decay. For this reason, it is referred to as a *dark state*. Even though the two light fields couple this state to the excited state, no population transfer to the excited state takes place. The two excitation pathways from $|g\rangle \to |e\rangle$ and $|r\rangle \to |e\rangle$ interfere destructively for this particular superposition. Therefore, an atom in this state is rendered transparent and effectively decoupled from the light fields.

[5] This is well justified for a collimated probe pulses of several microseconds like in the experiment.

The remaining two eigenstates contain the excited state and hence can decay into the dark state by spontaneous emission. Under continuous laser driving, the atoms therefore accumulate in the dark state by optical pumping. This effect, called coherent population trapping, was discovered by Alzetta *et al.* in 1976 [Alz76]. In contrast, in EIT, atoms that are initially in $|g\rangle$ coherently evolve into the dark state. Provided that the envelope of $\mathcal{E}_p^0$ of the electric probe field rises sufficiently slowly[6] the presence of the strong coupling field leads to an adiabatic rotation of the mixing angle and a loss free transmission of the probe beam through the medium.

To describe the properties of the EIT-resonance it is convenient to introduce the EIT-parameter $\mathcal{C} = \Omega_c^2/\Gamma_{gr}^0\Gamma_{ge}^0$ with the decoherence rates $\Gamma_{gr}^0 = \Gamma_{gr}(\Delta_p = \Delta_c = 0)$ and $\Gamma_{ge}^0 = \Gamma_{ge}(\Delta_p = 0)$. EIT is connected to the atoms being prepared in the dark-state and can only occur if the dark-state is populated faster than the decay Γ_{gr}^0 of the atomic coherence. With the rate Ω_c^2/Γ_{ge}^0 at which the dark-state is populated, $\mathcal{C} > 1$ is required for EIT to occur. This condition is similar to the condition for strong coupling in cavity quantum electrodynamics [Kim98, TS11] and reflects the strong light-matter coupling under EIT-condition.

On EIT-resonance the imaginary part of the susceptibility, which is connected to the absorption of the atomic cloud, takes on a minimum value χ_0. The spectral width of the transparency window, which reflects the appearance of the dark state, depends on the strength of the coupling beam and on the different dephasing rates. In the weak probe limit and $\Omega_c < \Gamma_e$ the susceptibility on resonance and the spectral width $\mathcal{W}_{EIT}$ (FWHM) can be expressed in terms of C and are given by

$$\chi_0 = \frac{1}{1+\mathcal{C}}\,\chi_{2lvl}^0 \tag{3.15}$$

$$\mathcal{W}_{EIT} = \Gamma_{gr}^0\,(1+\mathcal{C})\,. \tag{3.16}$$

This allows to achieve very narrow spectral features that are not limited by the natural linewidth of the exited state and which can be employed for high precision spectroscopy or electro- and magnetometry [Sed12, Fle00b].

Interestingly, the real part of the susceptibility which is related to the refractive index n of the atomic cloud changes rapidly in the EIT-window and shows normal dispersion on two-photon resonance. This leads to a reduced group velocity

$$v_g = \frac{c}{n_g} = \frac{c}{n(\omega_p) + \omega_p \frac{\mathrm{d}n}{\mathrm{d}\omega}} \tag{3.17}$$

where c is the speed of light and n_g denotes the group index. Since the change in refractive index is huge, a probe pulse entering the cloud gets slowed down and compressed [Hau99]. As the width of the EIT window depends on the coupling Rabi-

[6] The adiabaticity criterion is $\sqrt{\Omega_p^2 + \Omega_c^2} \gg \dot{\theta}$ [Fle05].

frequency, the steepness of the dispersion and accordingly the deceleration of the probe pulse can be controlled via the coupling beam, even allowing for a complete halt of the light pulse [Phi01]. This exceptional combination of no absorption in conjunction with a large dispersion, which can be controlled by optical means, makes EIT an ideal light-matter interface and sets the basis for many fascinating applications in non-linear and quantum optics.

3.1.4 Dark-state polaritons

To describe EIT on the level of single probe photons the semi-classical description is no longer sufficient. Accounting for the quantum-mechanical nature of the probe field a neat picture arises, in which the incident probe field and the atomic coherence form coupled excitations called *dark-state polaritons* [Fle05].

To motivate the appearance of these quasi-particles, we consider a probe pulse travelling through the atomic gas with the coupling beam present [Eis06]. As the front edge of the pulse enters the medium, it is rapidly decelerated due to the reduced group velocity. At the same time the trailing edge of the pulse is still outside the atomic gas and travels at the speed of light in vacuum. This results in a spatial compression of the light pulse entering the cloud by the ratio c/v_g while its photonic amplitude remains unchanged and its energy is reduced. When entering the cloud, part of the probe light together with energy taken from the coupling beam prepares the atoms in the dark state and establishes a coherence between the states $|g\rangle$ and $|r\rangle$, thereby altering the state of the atoms. This wave of atomic coherence, which is also referred to as a spin-wave[7], travels alongside the probe pulse through the cloud. At the end of the gas the process is reversed. The atomic coherence is converted without loss back into probe photons and the initial light pulse is recovered.

The described strong coupling of the probe light and the atomic coherence leads to the formation of mixed states of light and matter. In a homogeneous gas, for example, a single probe photon is coupled to the collective state, that comprises a single Rydberg excitation shared among all the atoms, and forms a dark-state polariton [Fle02]

$$\left|D^{(1)}\right\rangle = \cos\theta \left|g^{(0)}, 1\right\rangle - \sin\theta \left|R^{(1)}, 0\right\rangle, \tag{3.18}$$

where the collective states involving N atoms and the probe field are

$$\left|g^{(0)}, 1\right\rangle = |g_1, g_2, ..., g_N\rangle_{atomic} \otimes |1\rangle_{probe} \text{ and} \tag{3.19}$$

$$\left|R^{(1)}, 0\right\rangle = \frac{1}{\sqrt{N}} \sum_{j=1}^{N} e^{\phi_j} |g_1, ..., r_j, ..., g_N\rangle_{atomic} \otimes |0\rangle_{probe}. \tag{3.20}$$

[7] Using the mapping $|g\rangle \rightarrow |\downarrow\rangle$ and $|r\rangle \rightarrow |\uparrow\rangle$, the wave of atomic coherence can be interpreted as a spin-wave.

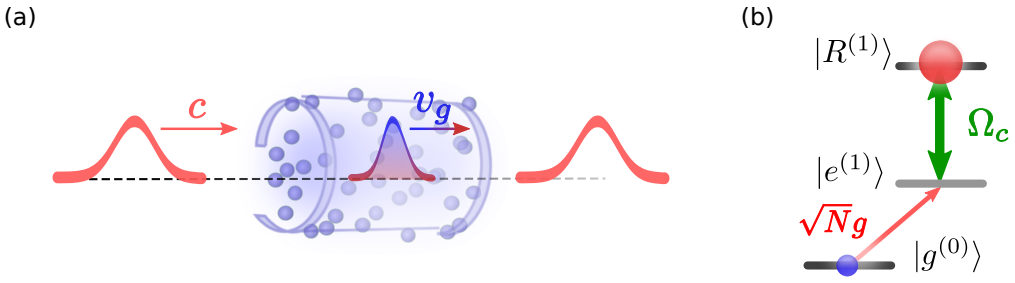

Figure 3.3: Single dark-state polariton. (a) Outside the atomic cloud the polariton is entirely photonic and travels at the speed of light c. Inside the medium the polariton pulse is compressed and transformed into a combined photonic and atomic excitation. The matter part bestows the polariton with a non-zero mass and the polariton travels with reduced velocity $v_g < c$. Leaving the medium the transformation is adiabatically reversed, recovering the initial probe pulse. The coupling beam Ω_c is not shown. (b) Levels and their couplings involved in EIT with a single photon in the probe mode coupled to the entire atomic ensemble - see text.

The mixing angle θ which determines the character of the polariton is defined by

$$\tan^2\theta = \frac{Ng^2}{\Omega_c^2} = \frac{n_a\,\sigma_0 c\,\Gamma_e}{\Omega_c^2} = \tilde{n}_g \tag{3.21}$$

with g the Rabi-frequency of a single probe photon, n_a the atomic density and σ_0 the resonant scattering cross-section for the $|g\rangle$ to $|e\rangle$ transition. Outside the medium the mixing angle is zero (as $n_a = 0$) and the polariton is entirely photonic as illustrated in Fig. 3.3. When the polariton enters the EIT-medium the mixing angle is adiabatically rotated and the polariton acquires a matter part. The matter admixure gives the polariton mass, resulting in a slow down of the polariton and propagation at a reduced group velocity

$$v_g = \frac{c}{1+\tilde{n}_g} \approx c/\tan^2\theta, \tag{3.22}$$

which is proportional to the photonic fraction of the polariton. This deceleration inside the medium leads to a compression of the polaritons which is accompanied by an increase in the polariton density. The density of dark-state polaritons

$$\rho^{(0)}_{DSP} = \frac{I_p}{\hbar\omega_p v_g} \approx n_a \frac{\Omega_p^2}{\Omega_c^2}. \tag{3.23}$$

is given by the probe photon density outside the medium $I/\hbar\omega_p c$ enlarged by the compression of the pulse inside the cloud by c/v_g[8]. As one can see from Eq. (3.23) the

[8]To relate the polariton density to the atomic density, we have used the approximate group velocity

polariton density can be controlled using the laser parameters and the atomic density which will become important in the case of interacting polaritons.

The states involved in EIT with a single probe photon shown in Fig. 3.3 (b), reveal an important difference to the single atom dark-state given in Eq. (3.13c). In contrast to the single atom picture, the polariton describes a collective atomic excitation. The collective coupling of the probe photon to all atoms in the probe mode leads to a $\sqrt{N}$ enhancement of the atom-light coupling g and an increased mixing angle. In other words, the probability to find one of the atoms in the Rydberg state is enlarged by a factor N compared to detecting one particular atom in the Rydberg state. Therefore under typical conditions in ultracold atom experiments, with densities in the range $n_a = 10^9 - 10^{13}\,\mathrm{cm}^{-3}$ and coupling Rabi-frequencies on the order of 5 MHz, the polaritons are almost entirely matter-like ($\cos^2\theta \approx 10^{-3} - 10^{-7}$).

The properties of the atomic states involved can hence be employed to engineer the properties of the polaritons which are subsequently mapped on the outgoing light field. This has been used for example to imprint a magnetic moment onto a light field [Kar06] or to realize giant electro-optical effects based on the large polarizability of Rydberg atoms [Moh08]. In the Sec. 3.3, we will extend this idea by coupling the light fields to a strongly interacting Rydberg gas, which leads to qualitatively new effects.

3.2 Experimental study of Rydberg-EIT in an ultracold gas of ^{87}Rb

In this section we present experiments on Rydberg-EIT in an ultracold atomic cloud of ^{87}Rb in the low density regime. We combine the spatially resolved detection of the transmitted probe light with the measurement of the Rydberg population via field ionisation in a single probe frequency scan. This gives access to the local optical susceptibility and the Rydberg state population, and allows to obtain the spectral and spatial properties of the underlying Rydberg-EIT system. Analysing EIT spectra for thousands of camera pixels in parallel, we deduce the beam profile of the coupling laser, which is subsequently used to reconstruct the spatial distribution of Rydberg atoms in the cloud.

3.2.1 Reconstruction of the coupling beam profile and the Rydberg distribution

The experiments presented here are performed in the low density regime, meaning that the Rydberg density is small compared to the blockade density. With atomic densities of a few $10^9\,\mathrm{cm}^{-3}$ and a blockade radius of $R_{bl} \approx 3\,\mu$m for the addressed $37S_{1/2}$-Rydberg state, the expected Rydberg density $\rho_{rr}\, n_a$ is much less than one per blockade volume

given in Eq. (3.22) together with $I_p = \varepsilon_0 c/2(\hbar\Omega_p/d_{eg})^2$.

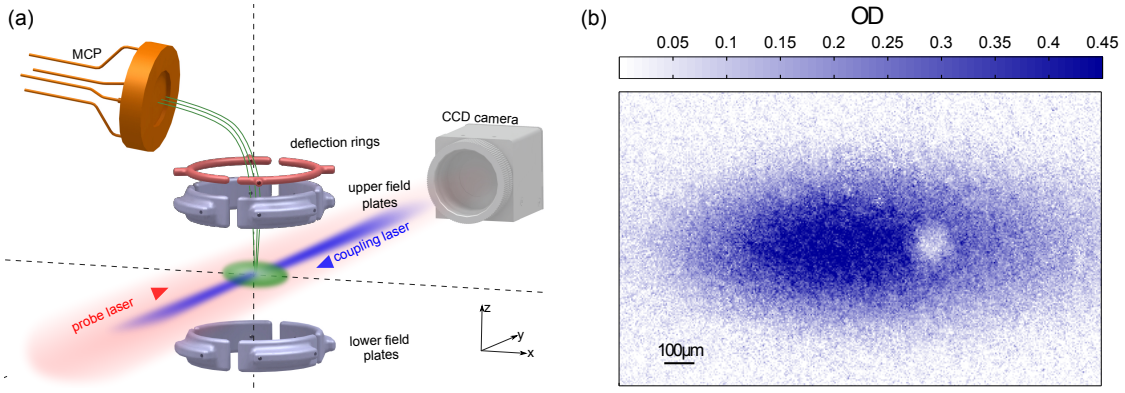

Figure 3.4: Spatially resolved EIT. (a) Schematic of the experimental setup. After release from the trap, the atomic cloud (green) is coupled to high-lying Rydberg states under EIT-condition with a probe and coupling laser at 780 nm and 480 nm, respectively. The transmitted probe light is imaged and detected on a CCD camera. An electrode structure is used for field control as well as for field ionization of the Rydberg atoms and guiding of the resulting ions onto a micro-channel plate (MCP) detector. (b) Absorption image of the atomic cloud with the coupling beam on two-photon resonance. Slightly to the right of the cloud center we observe a transparent spot as the presence of the coupling renders the cloud transparent.

$4/3\pi R_{bl}^3$. Therefore, effects of the Rydberg-Rydberg interactions are negligible and the interplay of the atoms with the light fields is well captured by the single atom picture outlined in the Sec. 3.1.

The experimental setup is sketched in Fig. 3.4 (a). After the microwave transfer, we release the atoms from the trap and let the cloud expand to prepare an atomic cloud with a peak density of $n_a = 3.9 \times 10^9\,\mathrm{cm}^{-3}$ and axial and radial extent of $\sigma_{ax} = 420\,\mu\mathrm{m}$ and $\sigma_r = 158\,\mu\mathrm{m}$, respectively. The probe and coupling beams are counter aligned and propagate perpendicular to the long axes of the cloud. We apply a homogeneous magnetic field of 3.8 G along the axes given by the two laser beams. The σ^--polarized coupling beam is focused on a small region of the cloud, whereas the σ^+-polarized probe beam with a waist of 15 mm uniformly illuminates the atomic cloud with a Rabi-frequency $\Omega_p = 2\pi \times 1.1\,\mathrm{MHz}$. The transmitted probe light is imaged onto a charge-coupled device (CCD) camera. In a single experimental run we take two images separated by 150 ms and with an exposure time of $t_{exp} = 20\,\mu\mathrm{s}$: one with the atoms and one without the atoms which we divide to obtain a standard absorption image of the cloud [Ock10]. Fig. 3.4 (b) shows a typical absorption image of the cloud. The presence of the coupling beam, which is resonantly driving the transition to the Rydberg state $37S_{1/2}$, renders the atoms transparent and manifests as a transparent spot slightly to the right of the cloud center.

Keeping the coupling laser resonant to the upper transition, we scan the probe frequency. Fig. 3.5 (a) shows the measured optical density (OD) at the center of the region illuminated by the coupling beam as a function of the probe detuning, which nicely

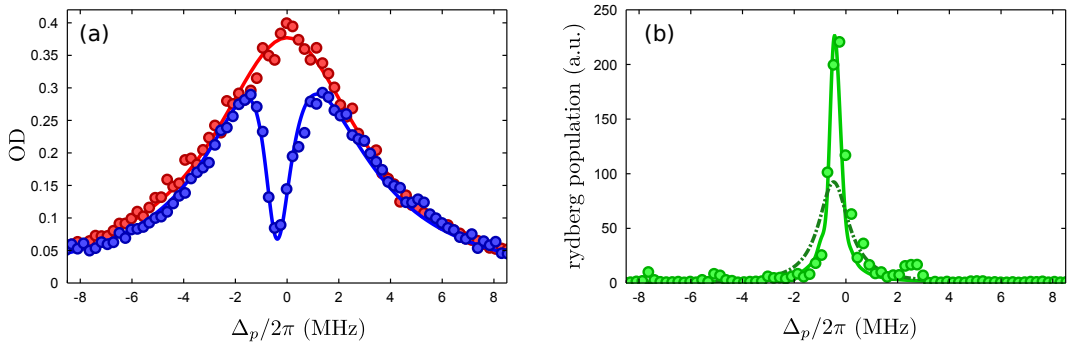

Figure 3.5: Measured EIT spectrum. (a) shows the optical density as function the probe detuning Δ_p. The blue data points show the optical density at the center of the region illuminated by the coupling beam, whereas the red data points display the response without the coupling beam, which is inferred from the 2D-fit to the absorption of the atomic cloud excluding the EIT-region. The solid lines are fits to the data using the optical Bloch-equations. (b) displays the Rydberg population measured in the same experimental run. The solid line is a calculated spectrum using the measured distribution of coupling Rabi-frequencies. In comparison, the dashed line shows the spectrum expected for a homogeneous coupling Rabi-frequency with $\Omega_c = \Omega_{c,max}$.

exhibits the expected transparency resonance. To quantify the degree of transparency in the presence of the coupling beam we use the different regions with and without the coupling beam of the atomic cloud. First, we fit a 2D-Gaussian distribution to the absorption image of the cloud excluding the region of the coupling beam to retrieve the atomic density distribution. Extrapolating the fit to the EIT-region, we infer the local atomic density as well as the two-level absorption without the coupling beam. With this information at hand we determine a reduction of slightly above 80% in the absorption at the center of the coupling beam compared to the two-level response.

Reconstruction of the coupling beam profile

Due to the coupling power dependence of the optical response under EIT-conditions (see Eq. 3.10b), the transparent spot visible in the absorption images does not necessarily reflect the beam shape of the coupling beam. In the probe frequency scan we acquire images of the whole cloud for the different detunings, which carry the information about the local optical response. We use this to construct a series of EIT-spectra pixel-by-pixel. Fitting the steady-state solution of the single-atom OBEs to the pixel spectra, allows us to extract the spatial distribution of coupling Rabi-frequencies on the atoms.

The EIT-region in a typical dataset involves $\sim 10^4$ pixels. This makes it prohibitively slow to fit pixel-by-pixel. In addition, the signal-to-noise for a single pixel is quite low. Therefore, we employ a two-step fitting routine, that minimizes the number of free parameters. In a first step, we use the result of the 2D-Gaussian fit to remove the linear density dependence of the optical density and to reduce the effect of density

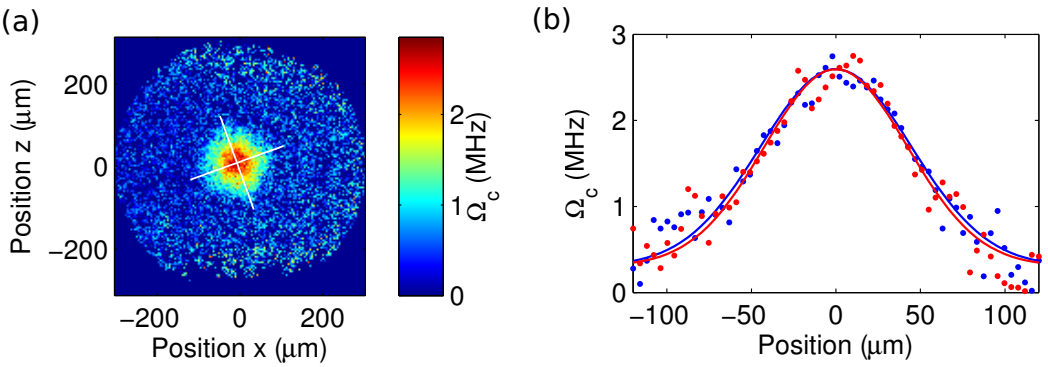

Figure 3.6: Measured coupling beam profile. (a) displays the reconstructed distribution of Rabi-frequencies at the position of the atoms. (b) shows cuts along the major axes of the distribution indicated with white lines in (a). The measured beam profile, using the atoms as a sensor, reflects the Gaussian beam profile of the incoming coupling beam.

fluctuations. To determine Ω_c for each pixel we assume that γ_{gr} and Δ_c are global laser parameters and pixel independent. Using the steady-state solution of the OBEs, we calculate model spectra corresponding to different $\Omega_c/2\pi$ between 0-10 MHz in steps of 0.05 MHz. To estimate the local Rabi-frequency we determine the least-square difference between the pixel spectrum and each model spectrum. The estimation of the local Rabi-frequencies is embedded in a Nelder-Mead non-linear optimization algorithm to find the best match for the global parameters. For the scan shown in Fig. 3.5, we extract a two-photon dephasing $\gamma_{gr} = 2\pi \times 260\,\text{kHz}$, $\Delta_c = 2\pi \times 0.39\,\text{MHz}$ and a peak coupling Rabi-frequency $\Omega_c = 2\pi \times 2.6\,\text{MHz}$ which is in good agreement with the estimated coupling Rabi-frequency using the measured power at 480 nm of 3 mW [Dei06, Pri11]. The reconstructed beam profile is shown in Fig. 3.6 and reflects the incoming Gaussian beam profile. We have also used this method to optimize the quality of a top hat beam profile [Hof13c] as well as to shape the coupling beam for the experiments presented in chapter 5.

Reconstruction of the Rydberg distribution

In the same experimental run, we measure the total Rydberg population which can be directly compared with the results of the optical spectrum fitting. At the end of the probe laser pulse we switch to an electric field of $\mathcal{E} \approx 250\,\text{V/cm}$ in 250 ns and field ionize the Rydberg atoms. The resulting ions are detected on a MCP detector as described in Sec. 2.2.2. Fig. 3.5 (b) shows the measured Rydberg population as a function of the probe detuning, which exhibits a narrow resonance. In the field ionization process we detect the Rydberg population in the entire atomic cloud, thereby essentially integrating the Rydberg atom distribution. Therefore, to match the measured spectrum, one has to account for the spatial inhomogeneity of the atomic density and the coupling Rabi-frequency as the Rydberg fraction $\sim \Omega_p^2/\Omega_c^2$ in the dark-state varies locally. This

can be accomplished using the reconstructed coupling beam profile and the inferred local atomic density. Since in the wings of the coupling beam profile the dynamics is slow and the system does not reach steady state, we introduce a cut-off Rabi-frequency. The cut-off Rabi-frequency $\Omega_{cut} \approx \sqrt{\Gamma_e/t_{exc}}$ corresponds to the minimum coupling strength, for which the atoms reach steady-state within the exposure time t_{exc}. For Rabi-frequencies smaller than Ω_{cut} we approximate the Rydberg-population as zero. The spectrum obtained by integrating the inferred local Rydberg population is in good agreement with the measured spectrum as shown in Fig. 3.5 (b). In comparison, the spectrum estimated using a homogeneous coupling Rabi-frequency $\Omega_c/2\pi = 2.6$ MHz is significantly broader and reduced in amplitude. Both features reflect the scaling of the Rydberg-fraction $\sim \Omega_p^2/\Omega_c^2$ and show that the Rydberg population in the wings of the coupling beam predominantly determines the total Rydberg population.

The combination of optical and population-based probing of coherently driven three-level atomic systems offers new ways to study phenomena like EIT, coherent population trapping and can help to elucidate their interrelation. The presented method that allows to characterize in-situ the system parameters like the coupling Rabi-frequency distribution serves as a valuable tool for the investigation of strongly-interacting many-body systems and is employed in the experiments presented in the following. Furthermore, as we will see in the next section, by combining optical spectroscopy with field ionization detection we can obtain nearly full access to the microscopic and macroscopic properties of Rydberg many-body systems.

3.3 Theoretical description of light propagation in an interacting Rydberg gas

On the level of single quanta, EIT is characterized by the appearance of dark-state polaritons which provide an intuitive picture to understand how coupling to strongly interacting Rydberg states under EIT-condition gives rise to the huge optical nonlinearities which we observe in the experiment. Furthermore, we observe that the polariton-polariton interactions mediated by their Rydberg component result in strong correlations of these quasi-particles.

3.3.1 Rydberg-interacting polaritons

In the following, we show how polariton-polariton interactions can be mediated by coupling to strongly interacting Rydberg states. Due to the nature of the Rydberg interactions this can lead to highly nonlinear and nonlocal optical effects [Sev11]. On one-photon resonance, the Rydberg blockade, in which a single excitation shifts the Rydberg states of atoms within the blockade radius out of resonance, gives rise to dissipative hard-core interactions between the dark-state polaritons. This is reflected

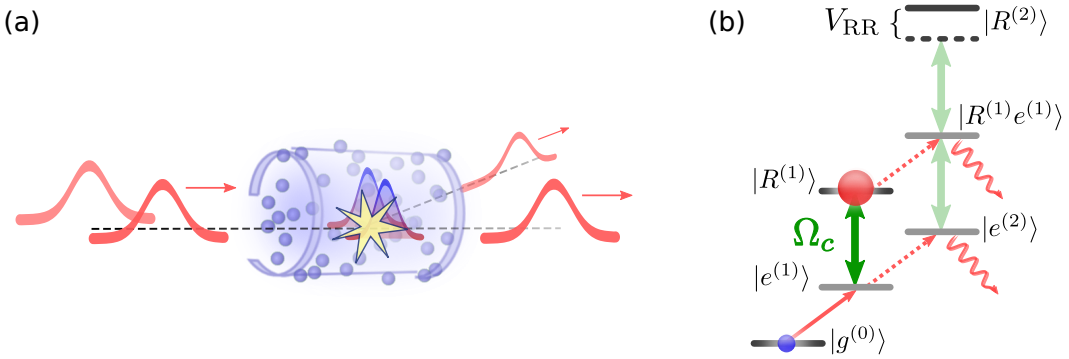

Figure 3.7: Interacting Polaritons. (a) Two photons impinge on an atomic cloud of the size of a blockade volume. Inside the cloud they are compressed due to the reduced group velocity of the polaritons and start to "overlap". The Rydberg blockade effect leads to a polariton blockade and the second polariton is scattered off the first polariton. (b) shows the states coupled by the light fields with two photons in the probe mode. Entering the cloud the first photon evolves into a dark-state polariton, as indicated by the populations in the states $|g^{(0)}\rangle$ and $|R^{(1)}\rangle$. The Rydberg-Rydberg interactions V_{RR} shift the collective state $|R^{(2)}\rangle$ out of resonance, which inhibits the formation of the two-photon dark-state inside the cloud. This effectively breaks the EIT-condition for the second photon, since it is now coupled to states containing the intermediate state $|e\rangle$ which is rapidly decaying.

in the emergence of correlations in both the atomic and the light fields [Gor11, Pet11, Pey12, Hof13b].

To understand how polariton-polariton interactions arise we provide the following simple picture: we consider a cloud of the size of the blockade radius and two photons subsequently impinging on the cloud as illustrated in Fig. 3.7 (a). The first photon enters the cloud and is converted into a dark-state polariton which propagates freely through the atomic cloud and is coherently converted back into the original optical mode upon leaving the cloud. When the second photon enters the cloud it tries to establish a co-propagating spin-wave to form a dark-state polariton. However, this is inhibited by the presence of the first polariton. The first dark-state polariton exhibits a large Rydberg state component, which strongly interacts with nearby atoms. This interaction shifts the state with two Rydberg excitations $|R^{(2)}\rangle$ out of resonance (see Fig. 3.7 (b)), which would be required to create a second dark-state polariton, effectively resulting in a polariton blockade (in analogy with the Rydberg blockade). The EIT condition for the second photon is broken and it is coupled to states containing the rapidly decay intermediate state. It is no longer dark and scattered from the cloud. This illustrates how atoms coupled to Rydberg states can act as a non-linear optical medium operating on the single-photon level, as a single photon inside the medium dramatically alters the medium properties.

This reasoning can readily be extended to large atomic clouds and arbitrary probe pulses. As long as the density of dark-state polaritons ρ_{DSP} is low enough, the proba-

bility to find two polaritons within a blockade volume is negligible and the polaritons propagate without loss through the medium. When the probability to find several polaritons in the same blockade volume is significant the excess polaritons are no longer dark and experience strong scattering. This imposes a critical density of dark-state polaritons $\rho_c = V_{bl}^{-1} = (4\pi R_{bl}^3/3)^{-1}$, corresponding to one polariton per blockade volume. Beyond this, the density of dark-state polaritons saturates.

3.3.2 Optical response of the interacting gas

Motivated by the picture of polariton-polariton scattering outlined above we set up a simple two-component model for the susceptibility to describe the transmission through the cloud under EIT-condition: the photons that are converted into dark-state polaritons propagate in the cloud under EIT-condition with residual susceptibility χ_0. In contrast, the remaining probe photons, which we will refer to as bright polaritons inside the cloud, are decoupled from the Rydberg state and hence experience the two-level response χ_{2lvl} of the lower transition. We therefore write the susceptibility as a weighted combination of the two components

$$\chi = f_{dark}\,\chi_0 + f_{bright}\,\chi_{2lvl} \tag{3.24}$$

with f the fraction of dark and bright polaritons, respectively. This simple two-component susceptibility is equivalent to the universal scaling relation given by *Ates et al.* [Ate11][9] which was obtained using Monte-Carlo simulations and a many-body rate-equation approach. Our simple model as well as the approach by Ates *et al.* neglect any effects of the scattering process on the dark-state polaritons. For instance, the scattering event can lead to a localization of the polariton wave-function which changes the polaritonic and subsequently the photonic mode of the outgoing photon.

In our model, all the many-body effects are encapsulated in f_{dark}. To determine the effect of polariton-polariton interactions on the probe transmission, we require a model to relate this to experimental parameters such as density and intensity. We employ a simple model based on an excluded volume picture to account for the interactions between polaritons. Each dark-state polariton in the cloud reduces the available volume by V_{bl}, thereby decreasing the probability to convert an incoming photon into a dark-state polariton. The density of dark-state polaritons ρ_{DSP} is hence reduced by $(1 - \rho_{\mathrm{DSP}}\,V_{bl})$ compared to the polariton density $\rho_{\mathrm{DSP}}^{(0)}$ without interactions (cf. Eq. (3.23)) and we find

$$f_{dark} = \frac{\rho_{\mathrm{DSP}}}{\rho_{\mathrm{DSP}}^{(0)}} = (1 - \rho_{\mathrm{DSP}}\,V_{bl}) \qquad \text{and} \qquad f_{bright} = 1 - f_{dark}. \tag{3.25}$$

[9] Using $f_{dark} = 1/\left(f_{bl} - 1\right)$, which relates f_{dark} to the blockade fraction f_{bl} used by *Ates et al.* and rescaling the susceptibility $\tilde{\chi} = \chi/\chi_{2lvl}$, one can readily see that Eq. (3.24) is equivalent to the universal scaling obtained in [Ate11].

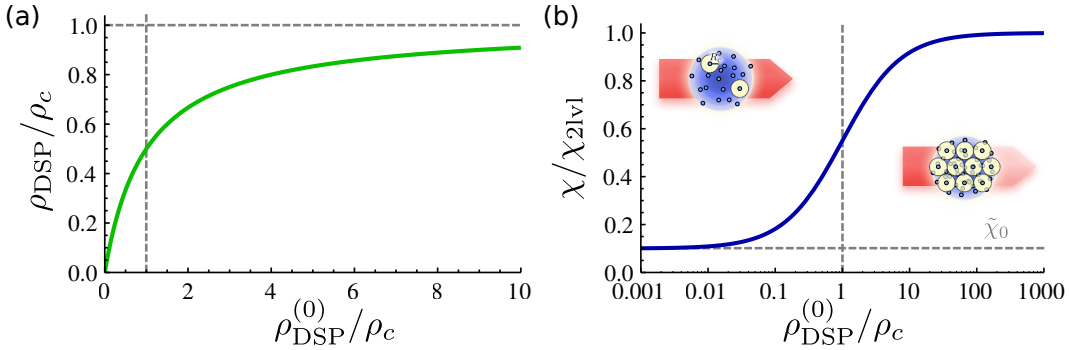

Figure 3.8: Modelled density of dark-state polaritons and the corresponding optical response. (a) Scaled density of dark-state polaritons as function of the scaled non-interacting polariton density $\rho^{(0)}_{DSP}/\rho_c$. (b) Scaled susceptibility χ/χ_{2lvl} as a function of $\rho^{(0)}_{DSP}/\rho_c$.

We can solve Eq. (3.25) for the density of dark-state polaritons and obtain the scaled dark-state polariton density

$$\rho_{\mathrm{DSP}}/\rho_c = \frac{\rho^{(0)}_{\mathrm{DSP}}/\rho_c}{1+\rho^{(0)}_{\mathrm{DSP}}/\rho_c} \tag{3.26}$$

which is shown in Fig. 3.8 (a). As expected, for low polariton densities ($\rho^{(0)}_{\mathrm{DSP}} \ll \rho_c$) the polariton density with and without interactions are identical as interaction effects are negligible. For high polariton densities, the density of dark-state polaritons saturates as the dark polaritons become densely packed in the cloud. This picture neglects collective effects which for example reduce V_{bl} when $\rho_{DSP} \gtrsim \rho_c$. Nonetheless, it is an excellent approximation to the results found by Monte-Carlo simulation [Ate11]. With the density of dark-state polaritons at hand, we can calculate f_{dark} and using Eq. (3.24) obtain the susceptibility of the interacting gas

$$\chi = \frac{\tilde{\chi}_0 + \rho^{(0)}_{\mathrm{DSP}}/\rho_c}{1+\rho^{(0)}_{\mathrm{DSP}}/\rho_c}\chi_{2lvl}, \tag{3.27}$$

where $\tilde{\chi_0} = \chi_0/\chi_{2lvl}$ is the rescaled susceptibility on EIT-resonance for a non-interacting cloud. The effect of the excitation blockade on the optical susceptibility is shown in Fig. 3.8(b): for small polariton densities the optical response is dominated by the residual absorption on EIT-resonance and shows a non-linear absorption proportional to $\rho^{(0)}_{\mathrm{DSP}}$. For $\rho^{(0)}_{\mathrm{DSP}} > \rho_c$, which marks the point of strong blockade, the susceptibility saturates towards the two-level response. This is expected as only a small fraction of photons will be converted into dark-state polaritons and most of the incoming photons will be absorbed in this regime. In the next section we present experiments in which we investigate the Rydberg-mediated optical non-linearity and map out its full dynamic range.

3.4 Optical and matter-based probing of interacting polaritons

Here, we investigate both light and matter aspects of strongly interacting dark-state polaritons in dense atomic gases involving highly excited Rydberg states. To map out the non-linear optical response of the atomic gas, we vary the atomic density over four orders of magnitude. Probing the matter part of the polaritons inside the atomic cloud, we find that the optical non-linearity is accompanied by reduced fluctuations in the polariton number when entering the strongly interacting regime.

In the experiment, we prepare a cigar shaped cloud of approximately 5×10^4 ^{87}Rb atoms at a temperature of 5 μK in the optical dipole trap. The experimental setup is similar to the one described in Sec. 3.2.1. The probe and the coupling light couple the states $|g\rangle = |5S_{1/2}, F = 2\rangle$[10], $|e\rangle = |5P_{3/2}, F = 3\rangle$ with a decay rate of $\Gamma_e = 2\pi \times 6.1\,\mathrm{MHz}$ and the Rydberg state $|r\rangle = |55S_{1/2}\rangle$ which has a lifetime of ≈ 80 μs [Bet09]. The circularly polarized probe beam uniformly illuminates the atomic cloud from the side and the transmitted light is imaged onto a CCD camera with an optical resolution of ≈ 12 μm (Rayleigh criterion). The coupling laser is again counter aligned to the probe beam. In contrast to the previously discussed experiments in which we worked with a Gaussian coupling beam, here the coupling beam is passed through a diffractive optical element to create an approximately uniform intensity profile with $\Omega_c = 2\pi \times 5.1\,\mathrm{MHz}$ over an elliptical region of $\approx 65 \times 130$ μm^2. The frequencies of both lasers are tuned to the respective atomic resonances. The linewidths of the two transitions, including both decay and dephasing terms, are determined in independent measurements as $\Gamma^0_{eg} =\approx 6.4$ MHz and $\Gamma^0_{gr} =\approx 1.7$ MHz for the probe transition and the two-photon transition, respectively. This yields an EIT coupling parameter $\mathcal{C} = \Omega_c^2/(\Gamma^0_{eg}\Gamma^0_{gr}) = 2.4$ and an EIT resonance width of $\mathcal{W}_{EIT} = (1+\mathcal{C})\Gamma^0_{gr} = 2\pi \times 5.8$ MHz. The anticipated blockade radius which is given by the distance at which the interaction energy matches the half width of the transparency window is $R_c = (2C_6/\mathcal{W}_{EIT})^{1/6} \approx 5$ μm with the van-der-Waals interaction strength $C_6 \approx 2\pi \times 50$ GHz μm^6. To control the atomic density before pulsing on the probe light we switch off the optical trap and vary the time-of-flight between 20 μs and 4.5 ms. Hereby the peak atomic density along the line-of-sight varies between $n_a \approx 10^{13} - 10^9\,\mathrm{cm}^{-3}$. This is coupled to a change in the cloud length in the probe direction between $\approx 2\,\mu$m and $100\,\mu$m and a change in the optical density of the cloud between 3 and 0.1, where the maximum optical density that we observe in the experiment is limited by the optical resolution.

[10] In contrast to the initial state preparation described in Sec. 2.2.1, in the experiments outlined here the atoms are not initially prepared in the state $|g\rangle = |5S_{1/2}, F = 2, m_F = 2\rangle$. After the evaporation the atoms are just repumped and are distributed over the $F = 2$ manifold. Also, no homogeneous magnetic field was applied.

3.4.1 Optical probing of the polaritons

To investigate the effects of the polariton interactions we vary the polariton density $\rho_{DSP}^{(0)}$. Looking at Eq. (3.23) this can be achieved either by changing the atomic density n_a or the intensity of the probe light I_p.

Figure 3.9 shows absorption images of the atomic cloud for three expansion times corresponding to three different peak atomic densities. For long time-of-flights, corresponding to low densities of $n_a \lesssim 10^{10}$ cm^{-3}, the cloud has expanded considerably and fallen under gravity. Here, we observe a high degree of transparency, which can be attributed to the low density of dark-state polaritons. By analyzing the images as described in section 3.2.1 we retrieve the absorption in the EIT region and extract the two-level absorption. At low densities, we find that the optical response is linear and corresponds to a scaled optical susceptibility $\chi_0/\chi_{2lvl} = 0.3 \pm 0.1$. This is consistent with the expected on-resonant optical susceptibility in the non-interacting EIT regime $\chi_0/\chi_{2lvl} = 1/(1+\mathcal{C}) \approx 0.29$. At densities above $n_a \approx 1 \times 10^{10}$ cm^{-3} we start to observe a decrease in the transparency due to interactions. Above $n_a \approx 4 \times 10^{11}$ cm^{-3} the EIT spot vanishes almost completely.

The full nonlinear optical response as a function of peak atomic density is shown for two different probe intensities of $5\,\mu$W/cm^2 and $62\,\mu$W/cm^2 in Fig. 3.9 (e). We observe a transition from transparent to fully absorbing by increasing density. The observed behaviour resembles the characteristic behaviour predicted for the susceptibility by the two-component model in Sec. 3.3.2 and by full many-body calculations of the optical susceptibility [Ate11]. For the higher probe intensity, the nonlinearity sets in for lower densities as expected since the higher incoming photonic flux results in a higher polariton density.

Fitting the two-component model to the experiment, we find that the effect of nonlinear absorption as the probe light propagates through the cloud must be accounted for. We simultaneously fit the two-component model to both datasets with a single critical polariton density as the only free parameter. The fit matches both datasets well, showing that the intensity scaling of the polariton density is well captured in the two-component model. The critical density obtained by the fit corresponds to a critical radius $R_{c,fit} = 8.2\,\mu$m, which is slightly larger than the anticipated blockade radius $R_c \approx 5\,\mu$m, reflecting stronger interaction effects than expected based on the simple picture presented in Sec. 3.3.2. Considering the simplicity of the two-component model the agreement is quite remarkable. The observed discrepancy might be due to the limitations of the two-component model which neglects the long-range tail of the polariton-interactions and effects of the scattering process on the dark-state polaritons. As discussed in Sec. 3.3.2, this might result in a reduced probe transmission which would mimic stronger interactions. Furthermore, effects of additional density dependent dephasing are not included in the model [Gär13].

The optical nonlinearity of the Rydberg gas has interesting properties. With the measured optical density $OD > 3$ for atomic densities above $5 \times 10^{11}\,$cm^{-3}, we estimate that the presence of a photon propagating through the cloud leads to a conditional

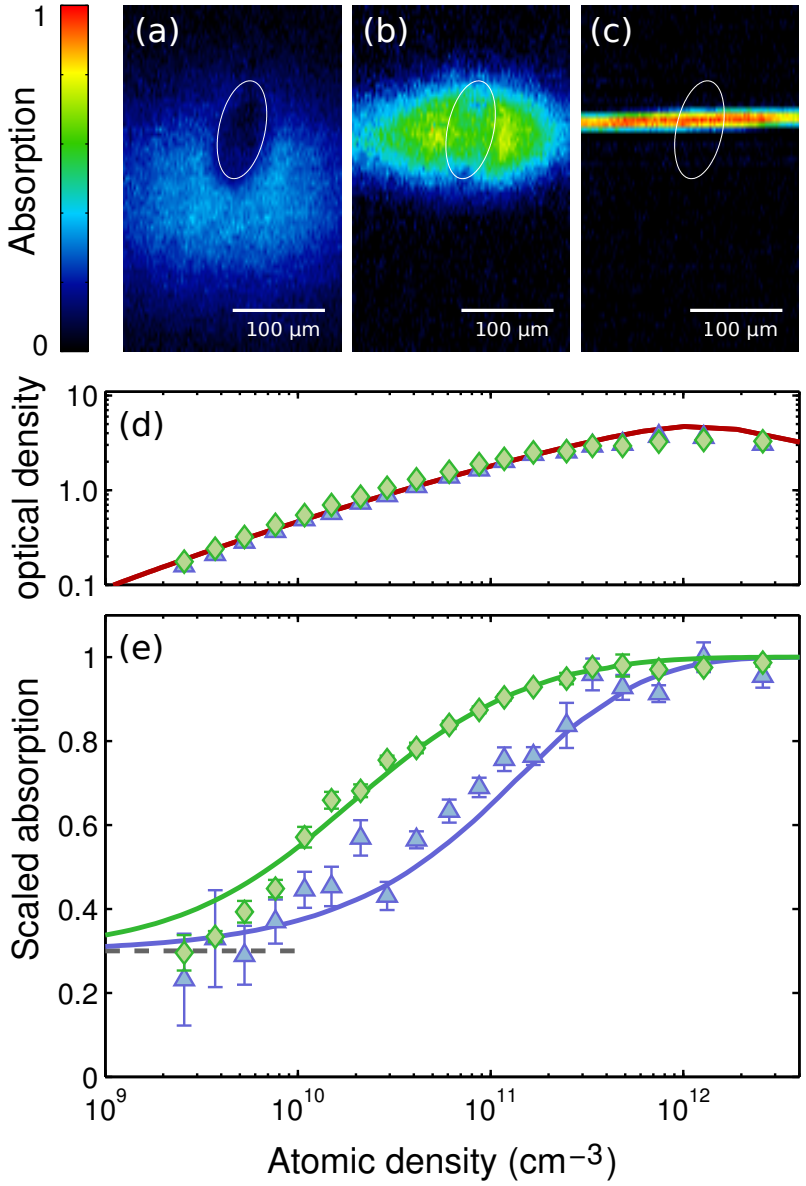

Figure 3.9: Nonlinear optical response of the Rydberg EIT medium. (a)-(c), Absorption images of the atomic cloud for three expansion times with a probe intensity of $I_p = 5\ \mu\mathrm{W/cm^2}$ and peak densities corresponding to $5 \times 10^9\ \mathrm{cm^{-3}}$, $5 \times 10^{10}\ \mathrm{cm^{-3}}$ and $3 \times 10^{12}\ \mathrm{cm^{-3}}$. The EIT region illuminated by the coupling laser is indicated by white ellipses. The measured optical density (d) and the absorption scaled to the two-level response are shown as a function of peak atomic density for two different probe intensities: $5\,\mu\mathrm{W/cm^2}$ (blue triangles) and $62\,\mu\mathrm{W/cm^2}$ (green diamonds). The dotted horizontal line shows the expected low density EIT absorption due to the finite laser linewidths. The solid lines are a fit to the data using the hard-sphere model with a single ρ_c as the only free parameter for both curves.

absorption of >95% for subsequent photons. This is expected to lead to strong correlations in the outgoing probe field and might allow to create quantum many-body states of photons such as crystals or trains of single photons [Gor11]. So far the conditions in our experiment are not ideal to investigate these states as the single photon absorption (without interactions) in this density regime is $\approx 60\%$. Therefore, most of the photons that propagate under EIT-conditions are absorbed, hindering the observation of these photonic many-body states. The single photon absorption is determined by the residual absorption on EIT-resonance which is mainly limited by laser linewidths in our experiments. These have been improved by a factor of about 10 since performing the experiments, opening the possibility to investigate these phenomena in future experiments.

3.4.2 Matter-based probing of the polaritons

In our experiments, the dark-state polaritons are almost entirely matter-like. For the given conditions the polariton mixing angle $\theta \to \pi/2$ and the photonic admixture of the polaritons becomes very small with $\cos^2(\theta) \approx 10^{-3} - 10^{-7}$ in Eq. (3.18). Therefore, measuring the Rydberg population serves as a projective measurement of the number of polaritons inside the cloud. Since the outgoing light field and the polaritons inside the Rydberg medium are non-trivially connected, measuring the dark-state polaritons inside the medium, which is done here for the first time, reveals new aspects of this strongly coupled light-matter-system. As the focus of this thesis lies on the effects of Rydberg-Rydberg interactions on the light field, only a summary of the findings of the matter based probing of the polaritons is given here. Further details can be found in [Hof13b].

We measure the polariton number inside the cloud by field ionization and subsequent detection of the individual ions on a MCP detector with high time resolution and near single particle sensitivity (cf. Sec. 2.2.2). This allows us to follow the polariton pulse in time as it propagates through the medium. In the low density regime, the probe pulse is mapped one-to-one onto the atoms and the observed dynamics of the polariton pulse is well described using the optical Bloch equations. To get into the regime of strong polariton-polariton interactions, we increase the atomic density. For high atomic densities we expect the polaritons to be densely packed and strongly correlated. Even though we cannot spatially resolve the polaritons in the experiment, which would allow to directly observe these correlations, the statistics of the polaritons can reveal the presence of polariton-polariton correlations. To obtain the polariton distribution we repeat the experiment many times and in each experimental run determine the number of detected ions. For low densities, the measured distribution shows Poissonian fluctuations reflecting the fluctuations of the incoming coherent light field [Scu97]. For high atomic densities, the polariton pulse gets delayed and we observe a significant narrowing of the measured ion distribution. This can be understood by examining the density of dark-state polariton ρ_{DSP} shown in Fig. 3.8 (a): for large atomic densities

corresponding to large ρ_0^{DSP}, the polariton density saturates. Because of this saturation, fluctuations in ρ_0^{DSP} or equivalently in the incoming probe field result in strongly reduced fluctuations of the density of dark polaritons. Reduced polariton fluctuations as observed in the polariton statistics reveal the emergence of spatial and temporal correlations among the polaritons [Ate09].

3.4.3 Interplay of photonic and atomic correlations

As mentioned earlier, in contrast to the non-interacting case it is not possible to relate the observed atomic correlations to the correlations in the outgoing light. Without interactions the quantum state of the light field is mapped one-to-one onto the polaritons and vice versa [Fle00a]. In the presence of polariton interactions no such general mapping between the correlations on the outgoing light field and the atomic correlations exists, as the following two examples illustrate. In a dense but optically thin medium, excess photons may not be efficiently scattered out of the forward direction thereby yielding almost classical fluctuations on the outgoing light field, despite the presence of strong atomic correlations. Alternatively, outside of the blockaded regime, spin-wave dephasing due to atomic interactions can significantly alter the statistics of the emitted light [Dud12b, Dud12a, Bar12], even though the atomic correlations could remain nearly classical.

Therefore, we also attempted to measure photonic correlations of the transmitted probe light. The simple picture outline in Sec. 3.3.1 implies that in the regime where the blockade radius is on the order of the absorption length or larger the polariton-blockade leads to anti-bunching of the outgoing photons. This would be reflected in a reduction of the second-order intensity correlation function $g^{(2)}(\tau = 0)$. Looking at the probe light transmitted through a region of the atomic cloud with a diameter of $5\,\mu$m, we measured the intensity correlation function in a Hanbury-Brown-Twiss type experiment [Bro56], but did not observe a reduction in the intensity correlation function. Probably the main reason for the lack off reduction in $g^{(2)}(\tau = 0)$ is our limited optical resolution of $12\,\mu$m, which leads to photons coming from different blockade regions being detected at the same position in the imaging plane. With an improved optical resolution combined with addressing Rydberg states with higher principal quantum number this can be overcome in future experiments.

3.4.4 Perspectives

The presented experiments provide a direct observation of strongly-interacting dark-state polaritons realized using EIT in an ultracold Rydberg gas. We observe strong polariton-polariton interactions through the density and intensity dependent optical response of the atomic gas and the polariton counting statistics, which become significantly sub-Poissonian at high densities, reflecting the emergence of spatial and temporal correlations between polaritons.

Only recently, photonic correlations have been observed in the second order intensity correlation function $g^{(2)}(\tau)$ of light retrieved from small Rydberg ensembles [Dud12b, Max13], and via light propagation through dense atomic clouds under Rydberg-EIT conditions [Pey12]. In our experiments, which can also be interpreted as Rydberg dressing of photons, in which photon-photon interactions are mediated by the Rydberg state admixture, also the out-going probe field is expected to be strongly correlated. So far, we could not observe the expected anti-bunching of the outgoing probe photons. Most likely, the two main limiting factors in the presented experiments are the optical resolution as well as the residual single photon absorption. These limitations can be overcome in future experiments by coupling to Rydberg states with higher principal quantum numbers and improving the optical resolution. For instance, with a principal quantum $n = 100$ the blockade radius increases to $\approx 15\,\mu$m. This is much larger than the optical resolution of our imaging system which has recently been improved to below $5\,\mu$m (Rayleigh criterion) [Hel13]. The larger blockade radius not only reduces the requirements on the optical resolution but at the same time can, depending on the cloud shape, increase the optical depth per blockade volume, thereby also enhancing the conditional absorption. With the installation of a new laser system, we have reduced the two-photon linewidth by a factor of about 10, which reduces the single photon absorption from 60% in the presented experiments down to 9%. Currently, we are setting up an ultrastable cavity to even further reduce the laser frequency fluctuations. This is expected to double the count-rate of transmitted photons which will facilitate the observation of photon correlations in future experiments.

By detuning from the intermediate state, the dissipative character of the polariton-polariton interactions could be suppressed while maintaining the huge non-linearities which would give rise to coherent photon-photon interactions. In a very recent experiment, it was shown that these coherent interactions can lead to attractive photon-photon interactions which favour pair-wise propagation of photons through the cloud and was observed as bunching of the outgoing photons [Fir13]. The large single photon nonlinearity gives complete control over the photon-photon interactions. This might allow to create and study novel photonic many-body states like photonic crystals [Cha08] or trains of single photons [Poh10, Gor11]. In addition, it opens fascinating possibilities to realize deterministic manipulation of photons for quantum information science [Gor11, Pri13].

4 Interaction enhanced imaging: A proposal

This chapter is based on the following publication:

Interaction Enhanced Imaging of Individual Rydberg Atoms in Dense Gases
G. Günter, M. Robert-de-Saint-Vincent, H. Schempp, C.S. Hofmann,
S. Whitlock, M. Weidemüller
Physical Review Letters **108,013002 (2012)**

The ability to prepare and probe individual quantum systems in precisely controlled environments is a driving force in modern atomic, molecular and optical physics. Manipulating single atoms [Mes96], molecules [Moe07] and ions [Lei03], for example, is becoming a common practice. At the heart of these experiments are powerful imaging techniques, which have taken on great importance in diverse areas, such as chemical sensing and chemical reaction dynamics [Bet93, Xie94], probing superconducting materials [Yaz97, Pan00], and for quantum logic and quantum information processing [Sch04, Nel07, Häf05]. Recently, new single atom and single site sensitive imaging techniques for optical lattices have opened the door to control and probe complex many-body quantum systems in strongly correlated regimes [Ger08, Bak09, Wei11].

The usual approach to detect single particles is to measure the fluorescence or absorption of light by driving a strong optical cycling-transition. Weak or open transitions present a difficulty since the maximum number of scattered photons becomes greatly limited. In the case of long lived states of trapped ions, electron shelving has been used as an amplifying mechanism in order to directly observe quantum jumps [Nag86]. Another approach involves the use of an optical cavity to enhance the interaction of atoms with a light field [Boc10, Geh10, Bra11]. This makes it possible to reach single-atom sensitivity, but usually at the expense of greatly reduced spatial resolution.

Here, we propose a new approach to imaging individual particles by exploiting their interaction with a bath of easily interrogated probe atoms. Interactions alter the properties of a strong optical transition for many probe atoms within a critical radius, thereby providing two mechanisms which greatly enhance the effect of a single impurity on the light field. As a probe we consider interaction-induced shifts of highly polarizable Rydberg states of a dense atomic gas resolved via a narrow electromagnetically induced transparency resonance. Even though the Rydberg states are barely populated, the

EIT resonance is extremely sensitive to their properties [Moh07, Wea08, Pri10, Tau10]. Thereby EIT provides the means to obtain a strong absorption signal and great sensitivity combined with high spatial resolution which as we will outline in this chapter allows for detecting individual impurities.

We exemplify our scheme for the specific case of imaging many-body states of strongly-interacting Rydberg atoms which act as impurities in a quasi-two-dimensional atomic gas as schematically depicted in Fig. 4.1. After introducing the basic principles of the proposed imaging technique and discussing the influence of different noise sources, we present simulations including the effects of experimentally relevant noise sources to demonstrate the potential of the proposed imaging method. The performed simulations show that non-destructive single-shot optical images of Rydberg atoms with high resolution and enhanced sensitivity can be obtained. We show in particular that this will provide immediate experimental access to spatial correlations in recently predicted crystalline states of highly excited Rydberg atoms [Wei08, Poh10, Sch10a, Bij11]. In contrast to field-ionization, the presented approach does not destroy the many-body Rydberg state and should also allow for the study of the time evolution of a single sample.

4.1 State of the art Rydberg imaging techniques

Traditionally Rydberg atoms are field ionized and the resulting ions are subsequently detected. This is inherently destructive, has relatively poor overall detection efficiency, and typically provides no spatial resolution. As a result, much of the investigations on ultracold Rydberg gases done so far, such as the scaling laws for excitation [Löw09], excitation statistics [Lie05, Amt10, Vit11] and light-matter interactions [Moh07, Wea08, Pri10, Sch10b], have been restricted to the study of cloud averaged properties. Whereas these experiments inferred the presence of the microscopic correlations from a change in the ensemble properties, they could not reveal the exact underlying microscopic structure of the gas. This is now changing with the first techniques being demonstrated, that allow for spatially resolved detection of Rydberg atoms. These techniques can be grouped depending on the atoms they work for namely alkali and earth-alkali atoms, and are briefly reviewed in the following.

The first experiment to show spatially resolved detection of single Rydberg atoms was performed by Schwarzkopf *et al.* [Sch11]. In their experiment, Schwarzkopf and coworkers combined the established technique of field ionization with techniques employed in field-ion microscopy. To spatially resolve the ions created in the field ionization process, an ionization electrode with a small, round tip is place only a few hundred micrometers from the atoms. The tip is switched to a high voltage, producing strongly diverging electric field lines at the position of the atomic cloud. The Rydberg-ions are subsequently extracted along these diverging field lines towards a two-dimensional MCP detector, thereby magnifying the initial spatial distribution of Rydberg atoms considerably. Using this technique Schwarzkopf *et al.* achieve a spatial resolution of

3.5 μm in their experiments which allowed them to observe spatial correlations in the Rydberg gas and to directly measure the blockade radius.

An optical approach for detecting single Rydberg-atoms with high sensitivity was demonstrated by Schauß *et al.* using high-resolution fluorescence imaging [Sch12]. After excitation of the Rydberg atoms, the atoms in the ground state are removed with resonant laser light, which is followed by de-excitation of the Rydberg atoms via stimulated emission to the first excited state. From there, the atoms rapidly decay to the ground state and are captured in an optical lattice. Using high-resolution fluorescence imaging the positions of the atoms are detected with a spatial resolution of $\sim 0.5\,\mu$m given by the lattice spacing [Wei11]. This allowed Schauß *et al.* to directly observe microscopic crystalline structures in small Rydberg ensembles. The single particle detection efficiency in their experiment of $\sim 75\,\%$ is quite high and mainly limited by the lifetime of the Rydberg state.

With a second valence electron, earth-alkali atoms offer alternative approaches to detect atoms with one electron in the Rydberg state. One way is to exploit auto-ionization of the Rydberg atoms upon excitation of the remaining core electron. With one electron in a Rydberg state with low angular momentum, excitation of the second core electron leads to rapid and efficient auto-ionization on a time scale of $\sim 100\,$ps. Lochead *et al.* used this auto-ionization mechanism as a local probe to sense the position of the Rydberg atoms [Loc13]. Scanning a tightly focused excitation beam across the atomic cloud they mapped out the position of the Rydberg atoms with a spatial resolution of $10\,\mu$m by detection of the auto-ions which were extracted by a small electric field.

Besides using the second electron to trigger auto-ionization processes, the remaining valence electron also allows to implement established optical detection techniques such as absorption or fluorescence imaging as was demonstrated by McQuillen *et al.* [McQ13]. Since the used optical transitions are in the near UV, this should in principle allow for good spatial and temporal resolution. To circumvent auto-ionization processes the Rydberg atoms have to be excited or transferred to high angular momentum states such that the wavefunction overlap of the two valence electrons remains negligible. In the experiments performed by McQuillen *et al.*, this was accomplished using a dilute ultracold neutral plasma, where the collision of plasma electrons promoted the Rydberg atoms to states with high angular momentum.

4.2 Basic principle of interaction enhanced imaging

Our imaging technique is based on the interactions of Rydberg impurities $|i\rangle$ with a bath of surrounding probe atoms. Fig. 4.1 illustrates the basic situation that we envisage. The presence of a Rydberg impurity causes an energy shift $U = \hbar C_6/|d|^6$ for the probe Rydberg state $|p\rangle$ of nearby atoms, where d is the distance from the probe atom to the Rydberg impurity and the interaction coefficient C_6 reflects the sign and strength of the impurity-probe interactions. This level-shift, which reflects the presence of the

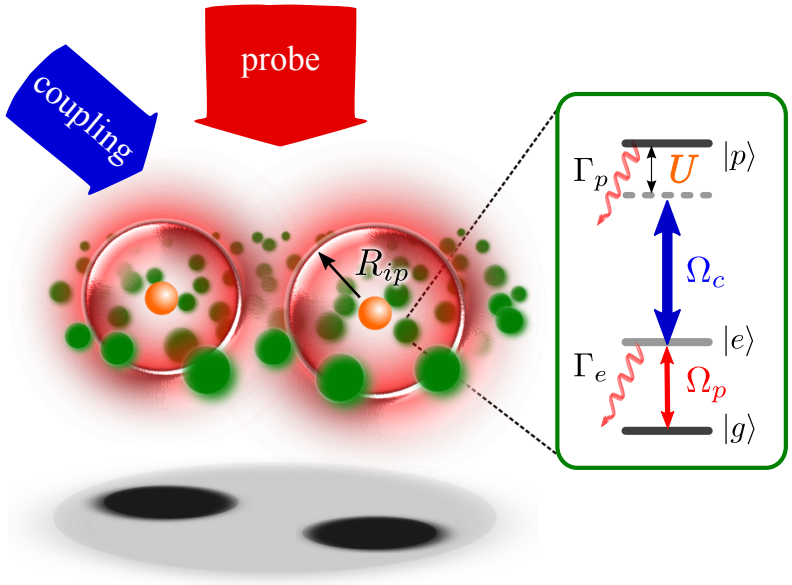

Figure 4.1: Scheme for imaging individual impurities within a dense atomic gas. Impurities (orange spheres) are embedded within a dense two-dimensional atomic gas of probe atoms (green spheres). The probe atoms are coupled under EIT-condition to a probe Rydberg state $|p\rangle$ via two coherent light fields characterized by the Rabi-frequencies Ω_p and Ω_c. This renders the atoms far from any impurity transparent for the probe light which is resonant to the lower transition. However, strong interactions with an impurity lead to a frequency shift U of the resonance within a critical radius R_{ip}, making the probe atoms in this region strongly absorbing. The change in absorption properties of many probe atoms surrounding an impurity makes it possible to map the position of the impurities onto the absorption profile of the probe laser allowing to image the impurities.

Rydberg impurity, is mapped onto the light field using an EIT-resonance involving the probe Rydberg state $|p\rangle$. Subsequent detection of the light field allows to reveal the impurity. The concept of our technique is related to an idea by Müller *et al.* which proposes that a single Rydberg atom could control the optical transfer of an ensemble of ground state atoms between two ground states using the Rydberg blockade [Mül09]. State-selective imaging of the atoms after the state-transfer could also be employed for detection of the Rydberg atom [Olm11].

To image the Rydberg impurities we consider the case of resonant driving ($\Delta_p = \Delta_c = 0$)[1]. Far away from any impurity, the probe Rydberg state $|p\rangle$ is unshifted and the probe atoms evolve into the dark-state $|D\rangle \propto \Omega_c|g\rangle - \Omega_p|p\rangle$, which decouples from the light field and the atoms become transparent as described in Sec. 3.1.3. In contrast, in the vicinity of an impurity the strong impurity-probe interactions shift the probe

[1]Resonant coupling ($\Delta_p = \Delta_c = 0$) provides the maximum contrast while maintaining the smallest probe Rydberg population.

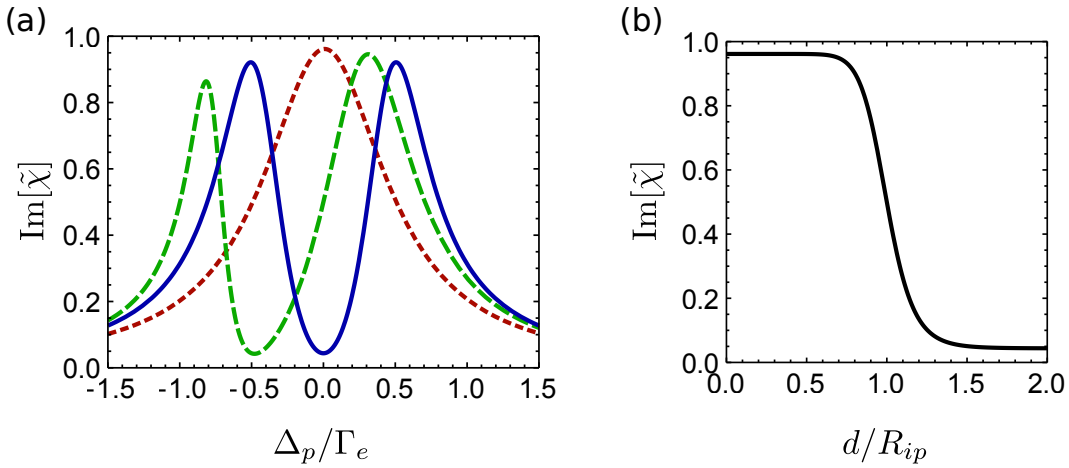

Figure 4.2: Imaginary part of the susceptibility depending on the distance to the impurity (a) Im$[\tilde{\chi}]$ as a function of probe detuning for $\Omega_c = 1$, $\Gamma_p = 0.006$, $\gamma_p = 0.04$, $\gamma_{gp} = 0.04$ and $\Delta_c = 0$ (in units of Γ_e) for three distances d from the Rydberg impurity. The solid red line shows the case $d \to \infty$, the dashed green line corresponds to $d = R_{ip}$ and the dotted blue line is for $d = R_{ip}/2$. (b) Im$[\tilde{\chi}]$ as a function of distance from the Rydberg atom with $\Delta_p = 0$.

Rydberg state which breaks the EIT-condition and leads to strong absorption on the probe transition. Hence, spatially resolved detection of the transmitted probe light reveals the positions of the impurities.

To describe the effect of an impurity Rydberg atom on the probe light field propagating through the atomic gas under EIT-conditions, we follow an approach based on the three-level OBEs outlined in Ch. 3. The interaction of an impurity with the surrounding probe atoms is incorporated as an additional spatially dependent energy shift $\Delta_c \to \Delta_c + C_6/|d|^6$ of the probe Rydberg state. In general, one should also account for interactions between atoms in the probe Rydberg state $|p\rangle$, but these only play a role if the population in $|p\rangle$ state is on the order of one per blockade volume (see Sec. 3.3.1). For $\Omega_p \ll \Omega_c$ the population in $|p\rangle$-state is small and these effects can be neglected which we will assume in the following. We include spontaneous decay from the intermediate and the probe Rydberg states as well as laser linewidths using the Lindblad formalism (cf. Sec. 3.1.1). Using the steady-state solution for the density matrix we solve for the susceptibility of the lower probe transition which reflects the effect of the impurities on the outgoing probe field. In the weak probe limit, the scaled susceptibility reads (see Eq. (3.10b))

$$\tilde{\chi}(\Delta_p, d) = \frac{\chi}{\chi^0_{2lvl}} = \frac{i\,\Gamma_e}{(\Gamma_e + \gamma_p - 2i\Delta_p) + \frac{\Omega_c^2}{\Gamma_p + \gamma_{gp} - 2i(\Delta_p + \Delta_c + C_6/|d|^6)}}. \tag{4.1}$$

where χ^0_{2lvl} denotes the absolute value of the on-resonant two-level susceptibility.

The imaginary part of the scaled susceptibility χ/χ^0_{2lvl} which is proportional to the

probe absorption is shown in Fig. 4.2 for different laser parameters and for different distances d to a Rydberg impurity. Far from the influence of the Rydberg impurity ($d \to \infty$), the susceptibility takes on the characteristic shape with vanishing absorption on resonance as discussed in Sec. 3.1.3. For smaller distances, the EIT resonance shifts due to interaction induce level shift of the $|p\rangle$ state and the on-resonant absorption starts to increase. For $d \to 0$, the excited states $|p\rangle$ become far detuned and the background atoms effectively act as two-level systems. In this case, the usual Lorentzian lineshape is recovered with maximum absorption on resonance.

From Eq. 4.1 and taking $\Delta_p = \Delta_c = 0$, we find the distance dependent susceptibility $\mathrm{Im}[\tilde{\chi}] \approx \left(1+(d/R_{ip})^{12}\right)^{-1}$ where we have defined a critical distance $R_{ip} = (2C_6\Gamma_e/\Omega_c^2)^{1/6}$ at which $\mathrm{Im}[\tilde{\chi}]$ reduces to half its maximum value. This critical distance reflects the point where the interaction shift matches the half width of the transparency window. As we can see in Fig. 4.2 (b) the susceptibility is almost constant for $d < R_{ip}$ and sharply drops around R_{ip} to its value without interactions. Hence, for a two-dimensional atomic gas with a density n_{2D}, the presence of a Rydberg atom essentially triggers $N = n_{2D}\pi R_{ip}^2 \gg 1$ atoms each with an absorption cross-section $\sim \lambda^2$ to scatter many photons, thereby producing a dark shadow on the probe beam. Since for typical experimental parameters $N \approx 50$, and $R_{ip} \approx 1$ μm which is comparable to experimentally accessible optical resolutions, the spatially resolved probe absorption provides an excellent signature for the presence of a single Rydberg atom within a dense gas.

4.3 Optimal parameters

To apply this scheme to real experiments one also has to analyze the influence of noise. The quality of an absorption image, which we will use to image the Rydberg impurities, will be degraded by intensity noise of the probe light and by intrinsic atomic density fluctuations. Since the EIT scheme relies on relatively weak probe intensities, and the number of ground state atoms in close proximity to a Rydberg impurity may be small, it is advantageous to find the parameters which will minimize the influence of imaging noise.

To locate a Rydberg atom in an image and to estimate its position we define a measure

$$\Delta T = \frac{N_{ph}^{(A)}}{N_{ref}^{(A)}} - \frac{N_{ph}^{(B)}}{N_{ref}^{(B)}}, \tag{4.2}$$

which reflects the difference in transmission (or equivalently absorption) of probe light between two regions of an image denoted A and B. We will employ this measure to quantify the signal-to-noise of the imaging technique. We consider the case with a Rydberg atom located in region A and B serves as a background region. To accurately estimate the position of the atom from the absorption image one must account for the noise in both the region of the atom (A), but also in the background region (B).

$N_{ph}^{(A/B)}$ is the total photon number detected in each region which is proportional to the number of counts of the CCD camera in the experiment. For the following analysis we assume a quantum efficiency ≈ 1. In the experiment, we take reference measurements with $N_{ref}^{(A/B)} \approx N_{ref}$ in the absence of atoms, that can be used to normalize out small spatial variations of the probe laser. Assuming N_g absorbing atoms in each region $N_{ph} = N_{ref}\,T \approx N_{ref}\exp\left(-sN_g\mathrm{Im}[\tilde{\chi}]\right)$, where we have expressed n_{2D} in Eq. (3.12) as N_g/a with a the area of the region and we have defined $s = \sigma_0/a$. The optical susceptibility $\tilde{\chi}$ depends on the laser detunings, intensities and on the proximity to a Rydberg atom as discussed in the previous paragraph. With a Rydberg atom located in region A, $\mathrm{Im}[\tilde{\chi}_A] > 0$ and we expect $\Delta T < 0$.

The precision with which an estimate of ΔT can be obtained is given by

$$\begin{aligned}\mathrm{var}(\Delta T) &\approx \frac{\mathrm{var}(N_{ref})\langle N_{ph}^{(A)}\rangle^2 + \mathrm{var}(N_{ph}^{(A)})\langle N_{ref}\rangle^2}{\langle N_{ref}\rangle^4} \\ &+ \frac{\mathrm{var}(N_{ref})\langle N_{ph}^{(B)}\rangle^2 + \mathrm{var}(N_{ph}^{(B)})\langle N_{ref}\rangle^2}{\langle N_{ref}\rangle^4}\end{aligned} \tag{4.3}$$

where we have propagated the variance[2]. Both intensity and atom number fluctuations are accurately described as Poissonian processes and $\mathrm{var}(N_{ref}) = \langle N_{ref}\rangle$ as well as $\mathrm{var}(N_g) = \langle N_g\rangle$. Using the propagation of variances once more we find $\mathrm{var}(N_{ph}^{(A)}) \approx \langle T_A\rangle^2\,\mathrm{var}(N_{ref}) + \langle N_{ref}\rangle^2\,\mathrm{var}(T_A)$ with $\mathrm{var}(T) = s^2\mathrm{Im}[\tilde{\chi}_A]^2\langle T_A\rangle^2\langle N_g\rangle$. Eq. (4.3) can then be expressed as

$$\begin{aligned}\mathrm{var}(\Delta T) &= \frac{2\langle T_A\rangle^2}{\langle N_{ref}\rangle} + \frac{2\langle T_B\rangle^2}{\langle N_{ref}\rangle} \\ &+ s^2\langle N_g\rangle\Big(\mathrm{Im}[\tilde{\chi}_A]^2\langle T_A\rangle^2 + \mathrm{Im}[\tilde{\chi}_B]^2\langle T_B\rangle^2\Big).\end{aligned} \tag{4.4}$$

The first two terms can be attributed to photon shot noise in the images while the last term is associated with atom number fluctuations. In the background region B the atoms are driven under EIT-condition and $\mathrm{Im}[\tilde{\chi}]_B \approx 0$. In the region of the impurity the and optical response including saturation and neglecting laser linewidths is given by $\mathrm{Im}[\tilde{\chi}]_A = \mathrm{Im}[\tilde{\chi}]_{max} = \Gamma_e^2/(\Gamma_e^2 + \Omega_p^2)$. In the limit of strong absorption $\langle T_A\rangle \ll 1$,

[2]For a quantity $f(a,b)$ which depends on two random variables the variance is approximately given by [Ock10]

$$\mathrm{var}(f) \approx \left(\frac{\partial f}{\partial a}\right)^2 \mathrm{var}(a) + \left(\frac{\partial f}{\partial b}\right)^2 \mathrm{var}(b) + 2\frac{\partial f}{\partial a}\frac{\partial f}{\partial b}\mathrm{cov(a,b)}$$

where the partial derivatives are evaluated at the mean values $\langle a\rangle$ and $\langle b\rangle$. Also the average of f is interpreted as $\langle f\rangle = f\left(\langle a\rangle, \langle b\rangle\right)$ in the following. If the two variables are uncorrelated, as it is the case for N_{ph} and N_{ref}, the covariance cov(a, b) vanishes.

which yields the best signal-to-noise ratio, we find

$$\mathrm{var}(\Delta T) \approx 2/\langle N_{ref}\rangle + s^2\langle N_g\rangle \mathrm{Im}[\tilde{\chi}]^2_{max} \exp\left(-2s\langle N_g\rangle \mathrm{Im}[\tilde{\chi}]_{max}\right). \tag{4.5}$$

This suggests that $\mathrm{var}(\Delta T)$ can be made arbitrary small for large $\langle N_{ref}\rangle$ and large $\langle N_g\rangle$. However, to ensure that ensemble-ensemble interactions can be neglected sets an additional constraint. To neglect these interactions we require that the polariton density $\rho^{(0)}_{DSP} \approx N_g/a \cdot \Omega_p^2/\Omega_c^2 \leq (\pi R_{pp}^2)^{-1}$ where R_{pp} defines the range of probe-probe interactions (see Sec. 3.3.1). This is equivalent to constraining the number of atoms in the probe Rydberg state $|p\rangle$ within a the radius R_{pp} to $\lesssim 1$. Taking N_g to be the number of ensemble atoms within a disk of radius R_{pp} implies $N_g \lesssim \Omega_c^2/\Omega_p^2$. Above this critical number, the susceptibility in the background region starts to increase from its minimum value as discussed in section 3.3.1 thereby reducing the contrast between the two regions. This constraint imposes a relationship between the maximum density of probe atoms and the maximum probe intensity $\langle N_{ref}\rangle \leq \Omega_c^2\tau/\sigma_0 n_{2D}\Gamma_e$, with the exposure time τ. Taking the maximum value of $\langle N_{ref}\rangle$ and expressing it in terms of n_{2D} the variance becomes

$$\mathrm{var}(\Delta T) = \frac{2\sigma_0\Gamma_e n_{2D}}{\Omega_c^2\tau}\left(1 + \frac{\Omega_c^2\tau\sigma}{2\Gamma_e\pi R_{pp}^2}\mathrm{Im}[\tilde{\chi}]^2_{max}\exp\left(-2\sigma_0 n_{2D}\mathrm{Im}[\tilde{\chi}]_{max}\right)\right) \tag{4.6}$$

with $\mathrm{Im}[\tilde{\chi}]_{max} \approx \left(1+2\,\Omega_c^2/\Gamma_e^2 n_{2D}\pi R_{pp}^2\right)^{-1}$. To find the optimal atomic density n_{2D}^{opt} and probe intensity for fixed Ω_c and τ one can now numerically maximize the signal-to-noise ratio using Eq. (4.6).

In general, the maximum signal-to-noise ratio is achieved for large coupling strengths Ω_c and long exposure times τ. In practice however, these will be limited by the available laser power and by the required time resolution, which has to be short compared to the typical lifetime of a Rydberg atom ($\sim 100\ \mu$s). In the following, we simulate imaging of ^{87}Rb Rydberg-impurities in the state $|i\rangle \equiv |55S\rangle$ and using the state $|p\rangle \equiv |28S\rangle$ as the probe state. Assuming $\Omega_c = 2\pi \times 50$ MHz and $\tau = 10\ \mu$s, we find $n_{2D}^{opt} = 50\mu\mathrm{m}^{-2}$. The additional effects of finite laser linewidths tend to increase ρ_{pp} slightly for the same Ω_p which leads to a shift of the optimum density to slightly lower values. Including this effect yields an optimal density $n_{2D}^{opt} \approx 40\mu\mathrm{m}^{-2}$.

4.4 Simulations

To show the potential of our imaging scheme we carry out numerical calculations of the EIT imaging process on simulated distributions of Rydberg atoms excited from a quasi-2D ideal gas. This situation can be realized experimentally e.g. by laser excitation of an ultracold atomic cloud initially confined in an optical dipole trap made from cylindrically focused Gaussian beams.

4.4.1 Rydberg excitation

To simulate the excitation of Rydberg impurities by a chirped laser pulse we employ a simple semi-classical model. We start from a randomly distributed, thermal gas of 25 000 ^{87}Rb atoms in their atomic ground state with a peak density of $n_{2D} = 40\,\text{atoms}/\mu\text{m}^2$ and a cloud radius of $\sigma = 10\,\mu m$. Each atom is treated as a point-like classical particle which can be in either the electronic ground state or in the Rydberg impurity state $|i\rangle \equiv |55S\rangle$. In the impurity Rydberg state the atoms show isotropic van der Waals interactions with a $C_6 = 2\pi \times 50$ GHz μm^6 [Sin05].

In the simulation the excitation laser is swept from 0 to +200 MHz within 6 μs with an effective Rabi frequency of $\Omega = 2\pi \times 2.0\,\text{MHz}$. During the excitation sweep each atom can undergo a transition to the impurity Rydberg state. The transition probability is estimated using the Landau-Zener formula for a sweep through an avoided crossing [Wit05]. The effect of Rydberg-Rydberg interactions causes level shifts for the nearby atoms which subsequently alters their probability to be excited by the laser pulse, giving rise to strong spatial correlations.

The simulation starts with zero detuning for the excitation laser and one atom is chosen at random to start in the Rydberg state. In the next time step the laser frequency is varied according to a fixed sweep rate, and we calculate all level shifts due to Rydberg-Rydberg interactions. From the atoms which crossed the resonance condition in the previous timestep we randomly select newly excited atoms based on their Landau-Zener probabilities. Any successful excitation immediately influences all other surrounding atoms. This is reflected in the simulated distributions in terms of the excitation blockade effect. For each time step we also solve the Newtonian equations of motion of the Rydberg atoms to account for their interparticle mechanical forces. The ground state atoms are assumed to be frozen and their motion is not included in the simulation. The simulation returns a list of the final coordinates of all the ground state and Rydberg atoms within the gas after the laser sweep. These coordinates are then used as inputs to calculate the corresponding absorption image.

4.4.2 Imaging process

We calculate absorption images of the simulated Rydberg distributions by numerically solving the optical Bloch equations for the probe atoms at each spatial position while accounting for the level-shifts produced by all Rydberg atoms. We assume the atoms are nearly stationary during the imaging process which requires temperatures below ≈ 10 μK which are readily achieved in experiments. From the mean intensity at each pixel, we generate Poisson distributed photon-shot noise. Similarly, a reference image is generated with uncorrelated noise for background division.

Fig. 4.3 shows calculated single-shot absorption images without and with the coupling laser. Each pixel corresponds to a region of $(0.5\,\mu\text{m})^2$ in the plane of the atoms and we assume an exposure time of 10 μs. The effect of finite optical resolution in the experiment is accounted for assuming a numerical aperture of NA = 0.25. For the

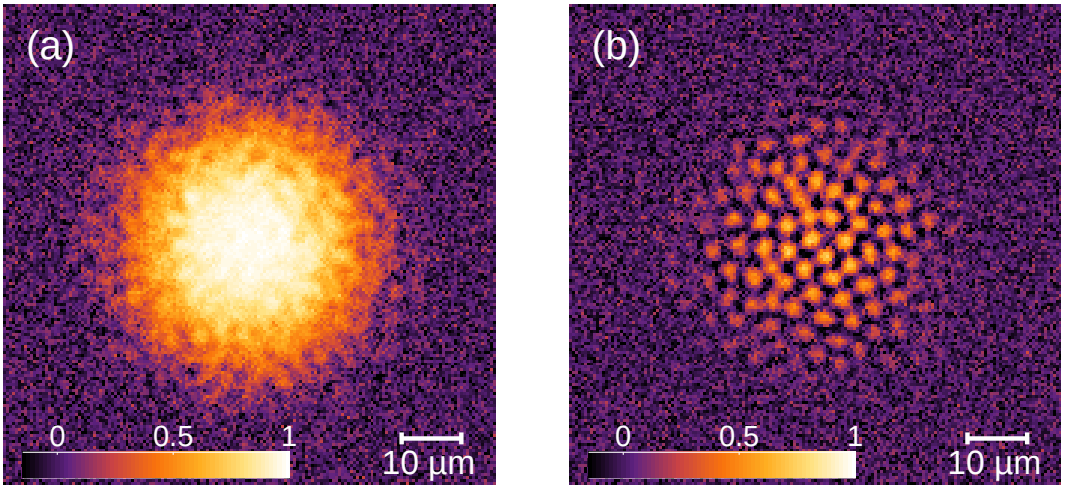

Figure 4.3: Simulated absorption images of atom distributions including photon shot noise and atomic density fluctuations. (a) Without the coupling beam ($\Omega_c = 0$), a regular absorption image of the probe atoms is obtained. The color code indicates absorption.(b) With the coupling on the probe atoms are rendered transparent, except for those in the vicinity of a Rydberg impurity. The positions of the Rydberg impurities are clearly identified bright spots in the absorption image. Parameters of the simulation are given in the text.

probe atoms, we take the ^{87}Rb states $|5S_{1/2}, F = 2, m_F = 2\rangle$ for the ground state, $|5P_{3/2}, F = 3, m_F = 3\rangle$ for the intermediate state and $|p\rangle \equiv |28S\rangle$ for the probe Rydberg state. The used decay rates are $\Gamma_e = 2\pi \times 6.1$ MHz and $\Gamma_p \approx 2\pi \times 10\,\mathrm{kHz}$ and for the coupling laser we assume $\Omega_c = 2\pi \times 50\,\mathrm{MHz}$. Laser linewidths of $2\pi \times 1\,\mathrm{MHz}$ were assumed for both probe and coupling lasers. The interaction coefficient between $|55S\rangle$ and $|28S\rangle$ states was calculated as $C_6(28S - 55S) = -2\pi \times 8.7\,\mathrm{MHz}\,\mu\mathrm{m}^6$ giving $R_{ip} = 0.59\,\mu\mathrm{m}$. Interactions between background atoms are taken as $C_6(28S - 28S) = 2\pi \times 10.1\,\mathrm{MHz}\,\mu\mathrm{m}^6$ ($R_c' = 0.61\mu\mathrm{m}$). Based on the analysis presented in Sec. 4.3, we choose $n_{2D} \approx 40\,\mathrm{atoms}/\mu\mathrm{m}^2$ which gives the optimal signal-to-noise ratio. The probe Rabi-frequency ($\Omega_p = 2\pi \times 5.8\,\mathrm{MHz}$) is chosen such that probe-probe interactions can be neglected. Such parameters are readily achieved in current experiments with quasi-2D atomic gases [Gör01].

In the background region of the image, the signal is dominated by photon-shot noise, while at the center atom-shot noise dominates. With the coupling laser on, the probe atoms are rendered mostly transparent, except for the regions of high absorption around each Rydberg atom (Fig. 4.3(b)). The locations of the individual Rydberg atoms are clearly resolved in the image as bright (absorbing) spots with a spatial extent of 2.3 μm FWHM comparable to the assumed optical resolution. Higher resolutions can easily be envisaged considering state-of-the-art atom imaging systems [Bak09, Wei11] with the fundamental limit given by the density of background atoms surrounding the impurities which is constrained by the probe-probe interactions and the achievable laser couplings.

The signal-to-noise ratio of our images is sufficiently high that we can fit the position of each Rydberg atom with subpixel precision.

4.5 Extracting spatial correlations

Of particular interest for current experiments is the possibility to observe strong spatial correlations between Rydberg atoms induced by interactions in an otherwise disordered gas [Rob05, Amt10, Wei08, Poh10, Sch10a, Bij11]. In the following we investigate the nature of the spatial correlations in our simulated Rydberg ensembles as well as how much information on long-range correlations can be obtained using the presented imaging technique.

From the simulated images, we see that the distribution of Rydberg atoms appears highly-correlated, reproducing some of the features of a full quantum mechanical treatment [Poh10]. To characterize the translational order of the simulated Rydberg distributions, we use the pair distribution function from the absorption images $A(\boldsymbol{r})$:

$$G_2[A](\boldsymbol{r}) = \frac{\int d^2r'\ A(\boldsymbol{r'})A(\boldsymbol{r'}+\boldsymbol{r})}{\left(\int d^2r'\ A(\boldsymbol{r'})\right)^2}. \tag{4.7}$$

To account for the inhomogeneous density and finite size of the system we normalize the pair distribution function, $g(\vec{r}) = \langle G_2[A]\rangle / G_2[\langle A\rangle]$, where the brackets reflect averages over independent realisations. For a random distribution of atoms $g(r) \approx 1$. Larger correlation values indicate an enhanced probability to find two Rydberg atoms at a given separation, while lower values indicate the absence of pairs.

Fig. 4.4 shows the pair distribution function $g(r)$ calculated from 15 simulated images. Since there is no preferred orientation in our system $g(r)$ takes on cylindrical symmetry. We clearly observe a shell with $g(r) \approx 0$ at a radius of $\sim$2.5 μm which reflects the strong blockade of excitation due to Rydberg-Rydberg interactions. At larger distances, we observe two positive-correlated shells at about 4 and 8 μm, which indicate translational correlations between nearest and next-nearest neighbours. The observed shell structure decays rapidly indicating the absence of true long-range order. We note very similar behaviour of $g(r)$ for the raw atom positions (shaded bars). From this we conclude that the information regarding density-density correlations can be reliably extracted from the images under realistic imaging conditions.

We can also extract information about the angular correlations in the images. For this we define the angular correlation function:

$$\Phi(\theta) \propto \left\langle \frac{\int d^2r'\ A(\boldsymbol{r'}) \int d\phi\ A(\boldsymbol{r'}+R_{sh}\boldsymbol{e}_\phi)A(\boldsymbol{r'}+R_{sh}\boldsymbol{e}_{\phi+\theta})}{\left(\int d^2r'\ A(\boldsymbol{r'})\right)^3} \right\rangle \tag{4.8}$$

where $\boldsymbol{e}_\phi$ is defined as the unit vector with angle ϕ with respect to a reference axis $\boldsymbol{e}_x$, and R_{sh} is the radius of the first positive shell of the pair distribution function. This

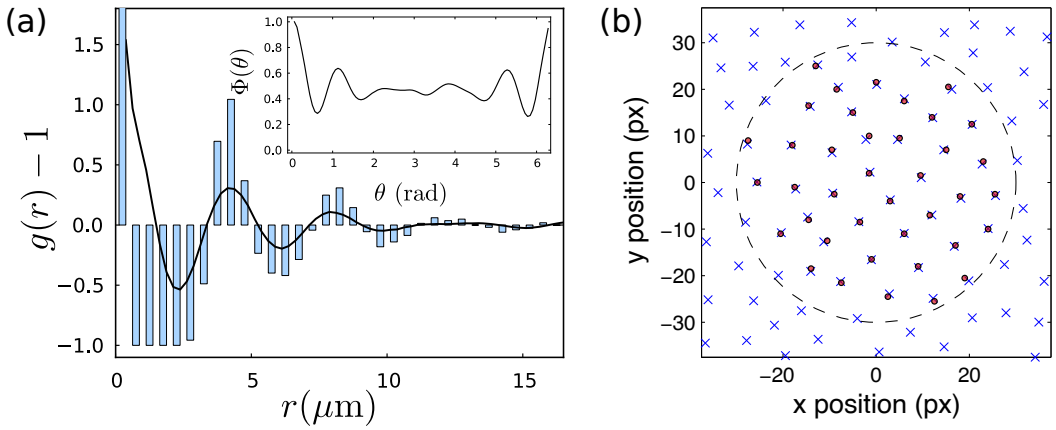

Figure 4.4: Pair distribution and angular correlation function of simulated Rydberg images and extracted positions of the Rydberg impurities. (a) The solid black line shows $g(r) - 1$ computed from the absorption images for 15 realizations. The shaded bars show $g(r) - 1$ taken directly from the simulated Rydberg atom coordinates with a bin size of 0.5 μm. The clear shell structure which reflects translational order between nearest and next-nearest neighbours is preserved by the images. The inset shows the angular correlation function for the radius of the first shell.(b) Rydberg atom positions extracted from Fig.4.3 compared with the Rydberg atom positions from the original simulations. Crosses correspond to the reference positions. Dots indicate the extracted positions from the noisy image using the matching pursuits algorithm.

gives the probability, starting from an atom and one of its nearest neighbours, to find a second nearest neighbour forming an angle θ with the first atom. The computed the angular correlation function $\Phi(\theta)$ at the radius of $R_{sh} = 4\,\mu$m is shown in Fig. 4.4. We observe the presence of two peaks at $\sim \pi/3$ and $\sim 5\pi/3$ rad, reflecting the 6-fold symmetry present among most nearest-neighbours. Even more information could be obtained from the images by studying higher-order correlation functions.

Alternatively, one could estimate the Rydberg atom positions and fully characterize the many-body state. We employ an image reconstruction approach based on sparse spikes deconvolution to extract the position of the individual Rydberg impurities. As we will see deconvolution of the images based on orthogonal matching pursuits algorithms [Mal93, RN02] allows to accurately locate individual Rydberg atoms even in the presence of noise.

The basic principle of the deconvolution algorithm is to iteratively construct an approximate image using an overcomplete basis of model functions. In each iteration step, the algorithm picks the model function which reduces the difference between the approximate image and the original image the most. While in general, there is an infinite number of ways to decompose an image using an overcomplete basis, a selection is made by constructing efficient image approximations from as few basis vectors as possible.

We use an overcomplete basis constructed out of a model image of a single Rydberg impurity. We calculate the model image of a single impurity by convolving a disk with radius R_{ip} with the point-spread function of the imaging system. In the analysis, the model image can be replaced by measured absorption spots of isolated impurities which e.g. are excited by a tightly focused laser beam. To construct the basis we displace the model image in steps of 0.5 pixel, resulting in $> 10,000$ basis elements covering the whole analysis region.

To reconstruct the position of the impurities we apply the matching pursuits deconvolution algorithm. The algorithm stops when adding another atom no longer reduces the difference between the original and the approximate image compared to the background noise level. The analysis is restricted to $1.5\,\sigma$ of the distribution of ground state atoms. Fig. 4.4(b) shows the reconstructed positions of the Rydberg impurities in Fig. 4.3 along side with their original positions. The algorithm retrieves 39 out of 45 impurities located in the analysis region. The impurities not found in the deconvolution process are located at the edge of the analysis region where the signal-to-noise is lower because of the reduced density of probe atoms. Of the 39 extracted impurities, 37 position are within a tolerance of one pixel. The median error in the position estimation is 0.4 pixel which is six times less than the optical resolution. This shows that our imaging technique allows to retrieve the position of Rydberg impurities with high efficiency and high spatial resolution, despite noise and limited optical resolution. This makes it ideally suited to study spatial correlations in Rydberg gases and to investigate crystalline many-body Rydberg states.

4.6 Perspectives

Our new imaging method provides the means to optically image individual particles within a dense atomic gas using Rydberg state EIT. The optimal imaging conditions which we identify are accessible in current cold atom experiments. To illustrate the potential of this novel imaging scheme, we have performed numerical simulations of Rydberg impurities excited from a quasi-2D gas and calculated the corresponding absorption images. The simulated images show that the imaging scheme allows for single-shot, non-destructive and time resolved images of many-body states Rydberg states.

We anticipate that this technique will complement the new optical lattice imaging techniques [Ger08, Bak09, Wei11], but with the capability to directly image many-body systems of Rydberg atoms like the recently predicted crystalline state [Poh10]. We can also foresee applications of the imaging scheme outside of the field of Rydberg physics. For example, single ions within an atomic gas could be to directly image [Gri09, Zip10, Sch10c]. Taking a gas of ^{87}Rb atoms coupled to the $|21S\rangle$-state which has a polarizability of $\alpha = -0.12\,\mathrm{MHz}/(\mathrm{V}^2/\mathrm{cm}^2)$, the presence of a single ion causes a level shift of $\approx 12\,\mathrm{MHz}$ at a distance of $1\,\mu\mathrm{m}$ which could be directly observed in current experiments. Closely related ideas could be used to realise a single atom optical transistor [Hwa09]. Furthermore our approach could be used to study the effects of

impurities and disorder on superfluids [Yaz97, Pan00], to realize high-fidelity readout of atomic quantum registers [Sch04, Nel07, Häf05], or as a precise way to observe individual charges or defects near surfaces [Gie11].

5 Interaction enhanced imaging: Experiments

This chapter is partially based on the following publication:

Observing the dynamics of dipole-mediated energy transport by interaction enhanced imaging
G. Günter, H. Schempp, M. Robert-de-Saint-Vincent, V. Gavryusev, S. Helmrich, C.S. Hofmann, S. Whitlock, M. Weidemüller
Science **342**, 954 (2013)

In the last years, strongly interacting ultracold gases and their associated quantum many-body states have attracted great interest [Blo08]. Especially, strongly interacting Rydberg gases have become an intense area of theoretical and experimental investigation [Löw12]. So far, probing of correlations among the Rydberg atoms was accomplished by studying interaction induced changes in cloud average properties which are readily accessible in the experiments. Recently, first images of Rydberg atoms have been obtained (cf. Sec. 4.1).

Here, we report on first experiments demonstrating interaction enhanced imaging [Gün12] which has been theoretically described in Ch. 4. We first introduce the experimental implementation of the imaging scheme as well as the imaging processing used to extract the impurity distribution. Then, we show how electric field tuning of the involved Rydberg states and exploiting Förster resonances can be used to maximize the signal per impurity. Using optimized conditions we sensitively image small numbers of Rydberg atoms in single-shot experiments with high-time resolution. Combining the imaging technique with simultaneous detection of the Rydberg atoms by field ionization, we directly observe the Rydberg blockade at the center of the cloud. Finally, we discuss ways to achieve single Rydberg sensitivity in future experiments.

5.1 Experimental implementation

The essence of interaction enhanced imaging is to exploit strong interactions between impurity atoms in the Rydberg state $|i\rangle$ with a bath of surrounding atoms, that are optically coupled to a probe Rydberg state $|p\rangle$ (cf. Ch. 4). Using an EIT resonance, the impurity-probe interactions are mapped onto the light field as schematically shown

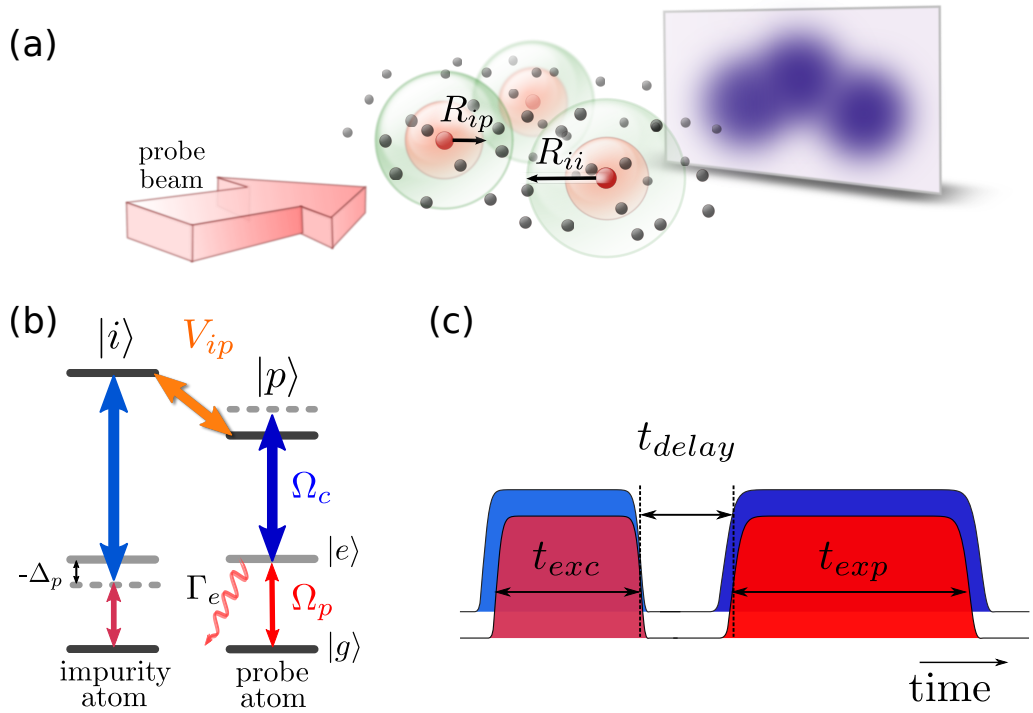

Figure 5.1: Interaction enhanced imaging experiment. (a) Each impurity (red sphere) breaks the EIT-condition for probe atoms within a volume characterized by R_{ip} due to the interaction induced level-shift on an auxiliary Rydberg-state $|p\rangle$ of the probe atoms. These atoms therefore strongly absorb the probe beam, casting a shadow in the images. The coupling beam which is counter-propagating to the probe beam is not shown. The minimal distance between two impurities is given by the impurity blockade radius R_{ii} which is larger than R_{ip} in our experiments. (b) Simplified level diagram showing the involved states in the excitation of the Rydberg-impurities $|i\rangle$ as well as the states involved in the EIT-ladder scheme which is employed to probe the level-shift on the state $|p\rangle$. (c) Pulse sequence of the excitation and imaging process.

in Fig. 5.1 (a). In the following, we discuss the implementation of the imaging scheme in the experiment.

In the experiment, we start with a cigar-shaped Gaussian cloud of ultracold ^{87}Rb atoms, prepared in the state $|g\rangle \equiv \left|5S_{1/2}, F = 2, m_F = 2\right\rangle$ with typical densities of $n_a = 5 \times 10^{10}\,\mathrm{cm}^{-3}$ and cloud parameters $\sigma_x \simeq 250\,\mu\mathrm{m}$ and $\sigma_r \simeq 15\,\mu\mathrm{m}$. In a first step, Rydberg impurities in state $|i\rangle \equiv |50S\rangle$ are excited within $t_{exc} = 5\,\mu\mathrm{s}$ in a small central region of the cloud, using a focused, direct two-photon excitation. The two excitation lasers at 780 nm and 480 nm, respectively, are two-photon resonant and detuned by $\Delta_p = -\Delta_c = -2\pi \times 65\,\mathrm{MHz}$ from the intermediate state $|e\rangle \equiv \left|5P_{3/2}, F = 3, m_F = 3\right\rangle$ as shown in Fig. 5.1 (b). The 780 nm light illuminates the entire cloud from the top. The σ^+ polarized 480 nm beam travels along the horizontal imaging axis and is focused onto

the atoms to define a well localized impurity region which is indicated in Fig. 5.2 (a). Using spatially resolved EIT-spectra in a low density cloud (cf. 3.2.1) we measure a vertical and horizontal beam waist of the 480 nm excitation beam of 19 μm and 7.4 μm, respectively.

The impurity excitation is followed by the acquisition of the image under EIT-conditions using separate lasers. We employ an EIT-ladder configuration involving the states $|g\rangle$, $|e\rangle$ and $|p\rangle \equiv \left|37S_{1/2}, m_J = 1/2\right\rangle$. The probe and coupling beams, which are σ^+ and σ^- polarized respectively, are counter-propagating and tuned to the single-photon resonances $|g\rangle \rightarrow |e\rangle$ and $|e\rangle \rightarrow |p\rangle$, respectively. The probe uniformly illuminates the cloud with typical Rabi-frequency $\Omega_p/2\pi \sim$ 1-2 MHz. The probe light transmitted through the cloud is imaged onto a CCD camera with a resolution of 9 μm (Rayleigh criterion). The coupling beam is focused onto the atoms to an elongated Gaussian intensity profile with $\sigma_x = 64\,\mu$m and $\sigma_y = 10\,\mu$m as indicated in Fig. 5.2 (a) with a peak coupling Rabi-frequency $\Omega_c \sim 2\pi \times 9$ MHz. Under these conditions, the polariton density is small compared to the critical density $\rho^{(0)}_{DSP}/\rho_c \ll 1$ and effects of probe-probe interactions on EIT are negligible (cf. Ch. 3). Typical exposure times for image acquisition are $t_{exp} =$ 2-20 μs.

To account for residual absorption and the spatial inhomogeneity of the coupling beam we take two images: one with and one without impurities. Figure 5.2 (b) shows an image of the cloud without impurities. The ellipsoidal coupling beam induces a transparency at the center of the cloud with a residual optical density of $\mathrm{OD_{EIT}} \approx 0.1$. The presence of the impurities breaks the transparency and leads to an increased absorption in the excitation region (Fig. 5.2(c)). By subtracting the two images, we determine the additional optical density $\mathrm{OD_{add}}$ induced by the presence of impurities. A typical image of approximately 200 impurities averaged over 150 shots is shown Fig. 5.2(d)[1]. Using the additional optical density we extract the number of additional two-level absorbers

$$N_{add} = \frac{A}{\sigma_0}\,\mathrm{OD}_{add} = -\frac{A}{\sigma_0}\log\left(\frac{I_{imp}}{I_{EIT}}\right), \tag{5.1}$$

with A the area corresponding to one pixel at the position of the atoms and $\sigma_0 = 3\lambda^2/2\pi$ the resonant scattering cross-section for the probe transition. I_{imp} and I_{EIT} denote the transmitted intensities of the probe beam for the image with and without impurities, respectively. To reduce the effects of shot-to-shot fluctuations in the atom number, photon-shot-noise and fringes, we make use of many images without impurities and construct an optimal image I^{opt}_{EIT} for each image with impurities [Ock10]. This is then used to determine the number of additional absorbers in this particular realization of the experiment. The optimal EIT-reference I^{opt}_{EIT} is obtained by solving for the

[1] The additional optical density in the images only reflects the presence of the impurities excited at the center of the cloud. In the shown images, the impurities are already blockaded at the cloud center and a significant fraction of the impurities is excited in the wings of the cloud which does not contribute to the signal. Also see Sec. 5.2.

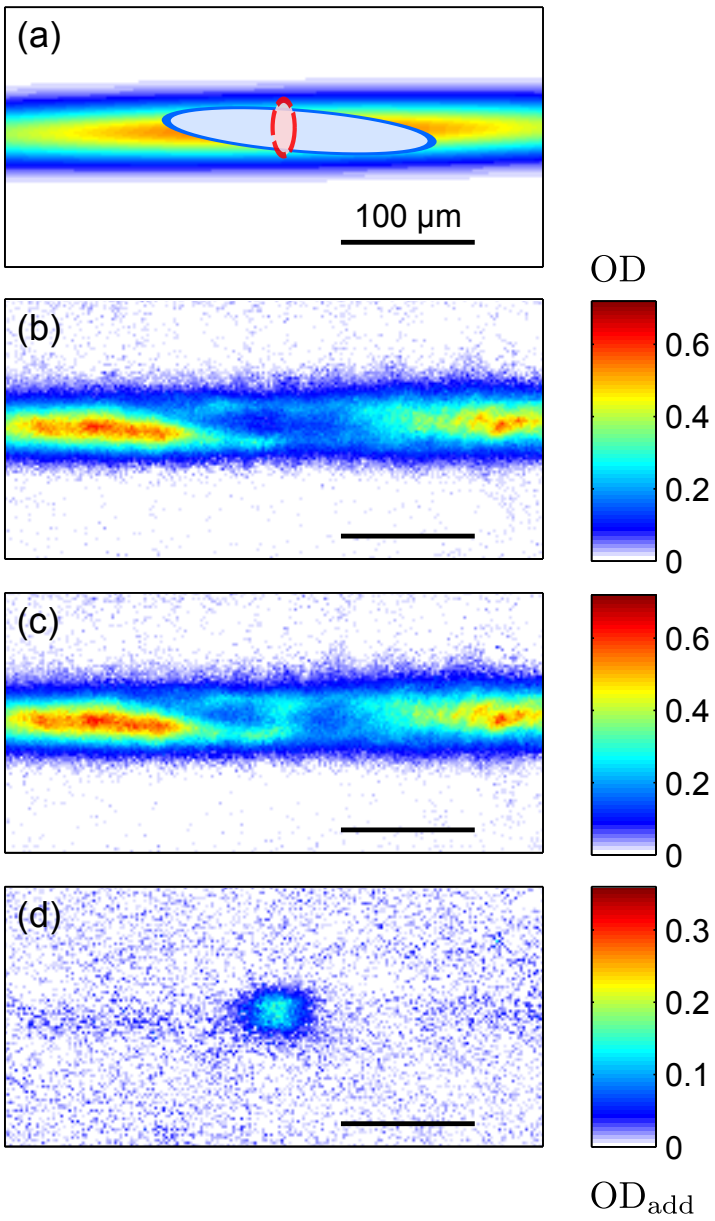

Figure 5.2: Images of the cloud with and without impurities. (a) schematically shows the cloud and the respective positions of the excitation (red) and imaging beam (blue). The ellipses indicating the two beams corresponds to $1.5 \times \sigma$ of the measured intensitiy profiles. (b) Without impurities the coupling beam, renders the center of the cloud transparent. The presence of impurities in the excitation region in (c) induces absorption, rendering the impurities visible. (d) shows the difference of the two images shown in (b) and (c) which only contains the additional absorption due to the impurities. The shown images are averages of 150 images taken with an exposure time $t_{exp} = 5\,\mu$s.

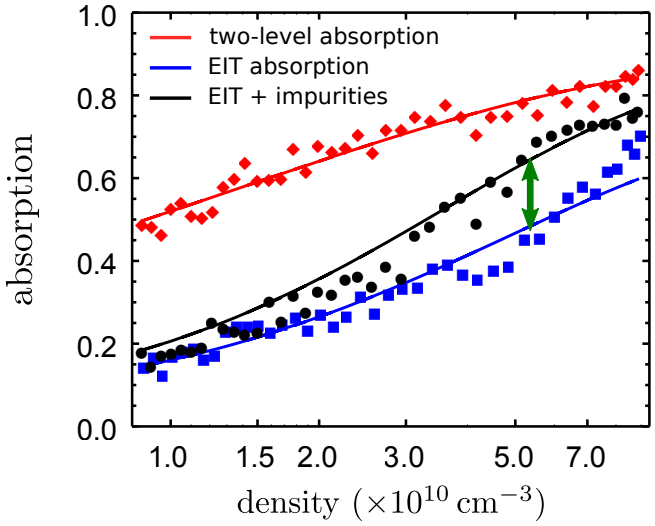

Figure 5.3: Density dependence of the imaging method. Shown are the two-level absorption (red diamonds), the absorption under EIT-conditions without (blue squares) and with impurities (black circles) at the center of the impurity region. With increasing density the absorption in the presence of impurities increases. This reflects the increasing number of probe atoms blocked per impurity. However, the absorption without impurities is also increasing due the imperfect transparency and interactions between polaritons mediated by the probe Rydberg state. The difference between the absorption with and without impurities reflects the additional absorption due to the presence of the impurities - the signal of the imaging technique. The green arrow indicates the density which yields the maximum signal for the given scan. The lines are guides to the eye.

linear combination of images without impurities, which best matches the image with impurities outside the excitation region.

5.1.1 Density dependence

To characterize the imaging method, we investigate the density dependence of the imaging signal. In principle, the number of blocked atoms per impurity and therefore the sensitivity of the imaging technique increases with density. However, for high densities the imperfect transparency and interactions mediated by the probe Rydberg state reduce the contrast of the imaging technique. Hence, these effects have to be balanced to achieve good imaging conditions in the experiment.

To characterize the density dependence, we record the absorption at the center of the impurity region under three different conditions: first, we record the two-level absorption of the cloud. This gives an estimate of the maximum possible number of absorbers. Second, we measure the absorption without impurities under EIT-conditions to analyze the effects of imperfect transparency and of probe-probe interactions (cf. Sec. 3.4). The difference between these two measurements determines the available

number of additional absorbers for imaging. In the last step, we record the absorption in the presence of impurities. The difference between the absorption with and without impurities reflects the additional absorption due to the presence of the impurities and gives the signal of the imaging technique. Fig. 5.3 shows a typical measurement of these three quantities as a function of the atomic density. The shown measurement was taken under slightly different conditions compared to the ones outlined in the previous section, with the main differences being a smaller coupling Rabi-frequency $\Omega_c \sim 5\,\mathrm{MHz}$ and impurities in the $38S$-state. For low densities the cloud is rendered highly transparent by the coupling beam, but the number of probe atoms within R_{ip} around an impurity is small which yields only little additional absorption due the impurities. With increasing density the absorption in the presence of the impurities increases ultimately almost reaching the full two-level absorption of the cloud. On the one hand, this reflects the increasing number of atoms blockaded by the impurities. On the other hand, the increase in absorption is also caused by the residual absorption due to imperfect EIT and the nonlinear optical response of the atomic cloud. The best imaging conditions are obtained when the increase in absorption in the presence of the impurities is largest. Under good imaging conditions, we typically observe an increase in absorption of $\sim 20\%$. For the scan given in Fig. 5.3, best conditions are obtained for an atomic density $n_a \sim 5 \times 10^{10}\,\mathrm{cm}^{-3}$ indicated by the green arrow.

5.1.2 Electric field tuning

To maximize the signal per impurity we make use of a Förster resonance to enhance the impurity-probe interactions [Gal08] (cf. Sec. 2.1.3). On the Förster resonance, the interstate interactions V_{ip} peak resulting in the maximum number of blockaded probe atoms per impurity.

The Rydberg impurities interact with the probe Rydberg state via dipolar coupling to close-by pair states. For our choice of states, the largest contribution to the interaction is given by

$$37S_{1/2} + 50S_{1/2} \leftrightarrows 36P_{1/2} + 51P_{3/2}\ . \tag{5.2}$$

Figure 5.4 (a) shows the calculated pair state energies as a function of the electric field $\mathcal{E}$. The energy of the $|37S_{1/2}, 50S_{1/2}\rangle$ pair states crosses with the ones of the $|36P_{1/2}, 51P_{3/2}\rangle$ pair states at electric fields of $0.35\,\mathrm{V/cm}$ and $0.38\,\mathrm{V/cm}$ for the $|m_j| = 3/2$ and $|m_j| = 1/2$ states, respectively, which gives rise to strong dipolar interactions.

To observe the Förster resonance in the experiment, we apply an electric field in the z-direction and record the number of additional absorbers which are displayed in Fig. 5.4 (b). The number of additional absorbers shows a resonance peak at about $\approx 0.5\,\mathrm{V/cm}$ which is close to the theoretically expected resonance position. The discrepancy of $\sim 0.1\mathrm{V/cm}$ can be attributed to a stray electric field. Using the polariz-

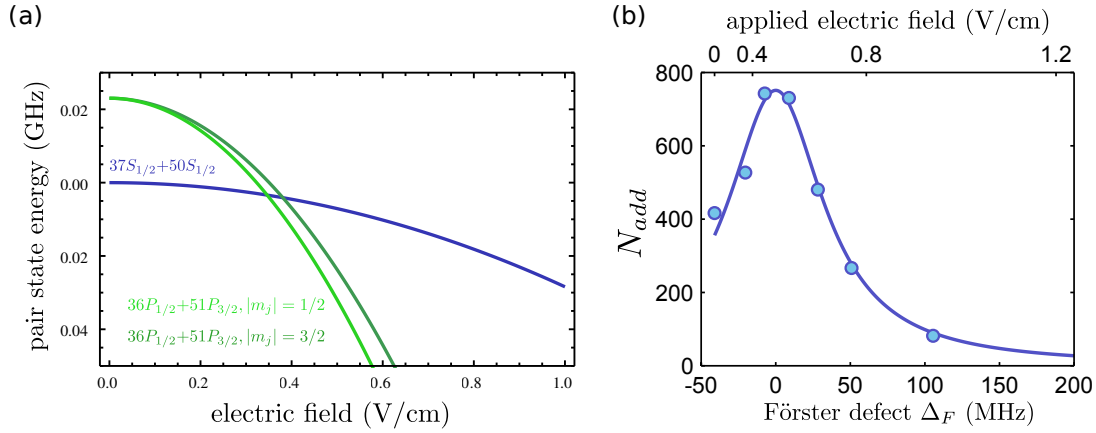

Figure 5.4: Electric field tuning of the interactions. (a) Calculated pair state energies as a function of the electric field. (b) Measured number of additional absorbers N_{add} for different applied electric fields (upper axis). Using the polarizability of the pair states, the electric field is converted into a Förster defect Δ_F shown on the lower axis.

abilities of the $|m_j| = 1/2$ states, we convert the applied electric field $\mathcal{E}_{applied}$ into a Förster defect $\Delta_F = 1/2\,([\alpha_{37S} + \alpha_{50S}] - [\alpha_{36P} - \alpha_{51P}])\,(\mathcal{E}^2_{stray} + \mathcal{E}^2_{applied})$ assuming that the stray field is orthogonal to the applied electric field. The zero position of the Förster defect is set to the peak position of the scan by fitting the stray field component. The narrow width of $\approx 80\,\mathrm{MHz}$ of the resonance, which is estimated using a Lorentzian fit, indicates that the imaging method can be made state-selective as only Rydberg impurities in a particular state interact strongly with the probe Rydberg state via the Förster resonance.

5.1.3 Sensitivity

For imaging, we tune to the Förster resonance which maximizes the interstate blockade radius R_{ip}. On resonance, the interactions are dipolar in character with $C_3 = 368\,\mathrm{MHz}\,\mu\mathrm{m}^3$ and the anticipated interstate blockade radius is $R_{ip} = (2\,C_3/(\gamma_{gr} + \Omega_c^2/\Gamma_e))^{1/3} = 3.8 \pm 0.3\,\mu\mathrm{m}$. This is, however, still smaller than the impurity-impurity blockade radius $R_{ii} = 4.35 \pm 0.2\,\mu\mathrm{m}$ including collective enhancement with approximately 70 atoms per blockade volume[2]. Hence, in the superatom picture the absorbing spheres that accompany each impurity do not overlap as indicated in Fig. 5.1 (a) and each additional absorber is blocked by a single impurity.

To determine the sensitivity of the imaging method, we compare the number of

[2]The blockade radius is estimated using $C_6/R_{ii}^6 = \left(\gamma^2/4 + N_c\Omega_{exc}^2/2\right)^{1/2}$ with $C_6 = 16\,\mathrm{GHz}$, $\mu\mathrm{m}^6$ for the 50S-state. For the two-photon excitation we take an effective Rabi-frequency $\Omega_{exc} = 0.4\,\mathrm{MHz}$ and a laser dephasing of $\gamma = 0.8\,\mathrm{MHz}$. For the number of atoms N_c within a blockade sphere the radial Gaussian density profile of the cloud is taken into account. The blockade radius given here was calculated for an elongated cloud with $n_a = 2.4 \times 10^{11}\mathrm{cm}^{-3}$ and $\sigma_r = 4.9\,\mu\mathrm{m}$.

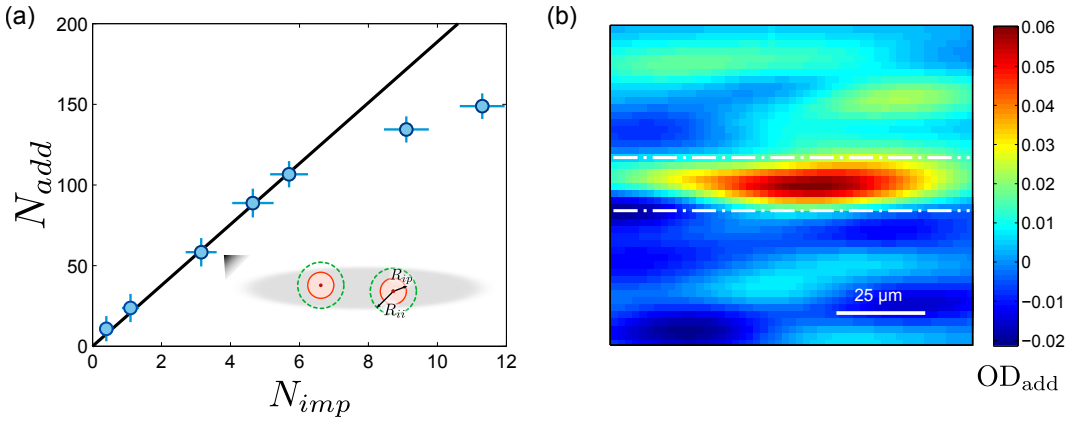

Figure 5.5: Imaging sensitivity for a quasi 1D-Rydberg ensemble. (a) For small numbers of impurities the number of additional absorbers grows linearly. The black line is a fit used to determine the amplification factor $A = 19 \pm 2$. For high impurity numbers the additional absorbers deviate from the linear behaviour indicative for the blockade at the cloud center (cf. 5.2). (b) A single-shot image of ~ 6 impurities obtained for an exposure $t_{exp} = 5\,\mu$s. The image is convolved with the average Rydberg distribution to reveal the presence of the impurities. The white dashed-dotted lines indicate the position of the cloud in the image. The indicated size of the cloud corresponds to $1.5 \times 2\,\sigma_{y,cloud}$.

additional absorbers with the number of impurity atoms detected using field ionization detection. We achieve the maximum sensitivity by radially compressing the cloud to $\sigma_r = 4.9\,\mu$m which increases the atomic density to $n_a = 2.4 \times 10^{11}\,\mathrm{cm}^{-3}$. Figure 5.5 (a) shows the number of additional absorbers N_{add} as a function of the number of impurity atoms N_{imp} in the compressed cloud. For low numbers of impurities, the number of additional absorbers increases linearly, since each impurity blocks roughly the same number of probe atoms. From the slope, we determine an amplification factor of $A = 19 \pm 2$ additional two-level absorbers per impurity. In this configuration the optical depth per interstate blockade sphere is $\mathrm{OD_{bl}} \approx 0.5$. This suggests that our images should be sensitive to single impurities. However, at the moment we are limited in the experiment by the optical resolution of our imaging system. Our optical resolution of $9\,\mu$m (Rayleigh criterion) prevents us from observing individual impurities for two reasons: first, as the optical resolution is larger than both R_{ip} and R_{ii} the absorbing spots of the impurities overlap in the images. Second, the optical resolution smears out the signal of an single impurity over ~ 20 pixels which results in a too low signal-to-noise to observe individual impurities in a single experimental realization.

Nonetheless, we can clearly detect as few as 5 impurities in a single shot with $\lesssim 5\,\mu$s time-resolution. As the signal is distributed over ~ 100 pixels due to the optical resolution, the signal-to-noise ratio for these small impurity numbers is not high enough to clearly see the impurities in the raw images. To reveal the impurities in a single shot image, we convolve the image with a smoothing kernel given by the averaged

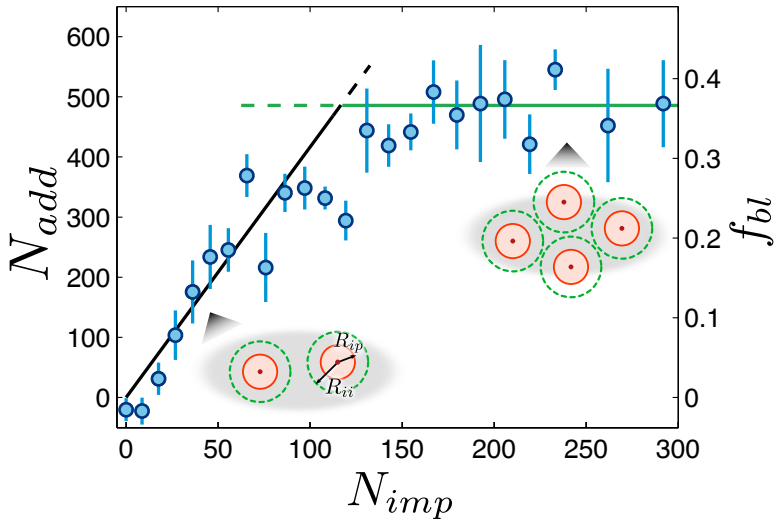

Figure 5.6: Imaging sensitivity and Rydberg-blockade in a 3D-Rydberg ensemble. For small impurity numbers, the impurities are mainly excited in the center of the cloud and the number of blockaded atoms per impurity is constant. This is observed as a linear growth in the number of additional absorbers indicated by the black line. For large impurity numbers, the number of additional absorbers deviate from the linear behaviour and saturates. As the center of the cloud becomes blockaded, the additional impurities are excited in the low density wing of the cloud without further increasing the number of blocked atoms. This is reflected in a saturation of the number of additional absorbers. The fraction f_{bl} of blockaded atoms at the cloud center is shown on the right axis and saturates at about ~ 0.38.

impurity distribution obtained from many shots. This minimizes the noise and makes the impurities clearly visible in the images. Fig. 5.5 (b) shows a processed single-shot image of ~ 6 impurities taken with an exposure time of $t_{exp} = 5\,\mu$s. The red signal in between the white dashed lines which indicate the position of the cloud corresponds to the signal of the atoms. For 6 atoms, we estimate the signal-to-noise to be ~ 2. By improving the optical resolution below R_{ip}, it should be possible to substantially increase the signal-to-noise for a single impurity and to resolve individual impurities in single shot images as will be further discussed in Sec. 5.3.

5.2 Imaging the Rydberg blockade

Even though under the current experimental conditions single impurities are not resolved in the images, the imaging method allows to investigate interesting phenomena such as the Rydberg blockade. As we have seen in the measurement in Fig 5.5 (a) for high impurity numbers the number of additional absorbers starts to deviate from the

linear behaviour observed for small numbers of impurities. This indicates saturation of the impurity density at the cloud center which is a manifestation of the Rydberg blockade.

To investigate the Rydberg blockade effect using interaction enhance imaging, we simultaneously determine the number of impurities and the number of additional absorbers in a larger volume and involving more impurities. The experimental conditions, which correspond to a 3D-geometry with respect to the Rydberg excitation, are the same as those described in Sec. 5.1. We observe the blockade by varying the excitation power which changes the number of impurities in the cloud. The measurement is shown in Fig. 5.6. In the case of weak excitation, the number of impurities increases linearly, reflecting the sensitivity $A = N_{add}/N_{imp} = 4.2 \pm 0.3$ for the given experimental parameters. For stronger excitation, however, the number of additional absorbers N_{add} saturates. As the impurity density in the center of the cloud saturates because of the blockade, the number of impurities increases further due to excitations in the low density wings of the cloud. However, this does not significantly increase the total number of additional absorbers as the density of probe atoms is low in this region.

To further investigate the blockade of the impurity atoms, we determine the fraction of additional absorbers $f_{bl} = \mathrm{OD_{add}}/(\mathrm{OD_{2lvl}} - \mathrm{OD_{EIT}})$ at the cloud center. This gives the ratio of the optical density of additional absorbers compared to the available two-level absorbers. Above approximately 150 impurities, f_{bl} saturates at a value of 0.38 ± 0.02. This is consistent with the picture that the blockade-limited density of impurities is $\rho_i \approx (4\pi R_{ii}^3/3)^{-1}$ and each impurity produces an absorbing sphere with a radius given by R_{ip} which is smaller than the impurity blockade radius $R_{ii} = 3.75 \pm 0.2\,\mu$m. In this case, we expect $f_{bl} \simeq R_{ip}^3/R_{ii}^3(1 - \rho_i/n_a) = 0.49 \pm 0.2$, in good agreement with the data. The factor $1 - \rho_i/n_a$ takes into account that the density of probe atoms is reduced compared to the atomic density n_a by the excitation of the impurities.

5.3 Towards imaging of single Rydberg atoms

So far, our experiments were limited to imaging of distribution of Rydberg atoms. Here, we discuss how this limitation can be overcome and individual Rydberg atoms can be imaged in future experiments. We identify two main ingredients to accomplish this task. Besides improving the imaging resolution, which was already pointed out in Sec. 5.1.3 as major limitation, addressing Rydberg states with higher principal quantum numbers offers several benefits for future experiments. These states exhibit larger interactions which result in increased interstate blockade radii. This provides two advantages: on the one hand side it reduces the demands on the optical resolution and at the same time increases the number of absorbers per impurity which boosts the sensitivity of the imaging method.

To show that imaging of single Rydberg atoms is within reach, we consider imaging Rydberg impurities in the state $|i\rangle \equiv |69S\rangle$ with the probe atoms optically coupled to the state $|p\rangle \equiv |50S\rangle$. For the parameter estimation, we assume an elongated atomic

cloud with a density $n_a = 1 \times 10^{11}\,\mathrm{cm}^{-3}$ and a radial extent of $\sigma_r = 5\,\mu$m similar to the presented experiments. The van der Waals interactions[3] between the impurities and the probe state result in an interstate blockade radius $R_{ip} = (2C_6/(\gamma_{gr} + \Omega_c^2/\Gamma_e))^{1/6} \simeq 4.8\,\mu$m with $C_6 = 98\,\mathrm{GHz}\,\mu\mathrm{m}^6$, $\Omega_c = 10\,\mathrm{MHz}$ and dephasing and decay rates like in the presented experiments. This yields about 40 absorbers per impurity which can readily be detected in cold atom experiments using absorption imaging [Ock10, Mue13]. Including the collective enhancement, we obtain an impurity blockade radius of $R_{ii} \simeq 7.6\,\mu$m taking an excitation Rabi-frequency $\Omega_{exc} = 0.5\,\mathrm{MHz}$ and an excitation linewidth of 0.8 MHz. The absorbing spots of individual impurities are therefore well separated. With the improved optical resolution in our experiment of $4.8\,\mu$m (Rayleigh criterion) [Hel13] the spots should be resolved in the images and it should be possible to determine the position of individual impurities.

In addition, it might be advantageous to use van der Waals interaction between the impurities and the probe atoms. Whereas dipolar interactions on a Förster-resonance maximize the signal per impurity atom, the resonant coupling to another pair state can lead to transport dynamics, as we will discuss in the next chapter, and motion during the imaging process has to be considered.

[3]The Förster defect of the closest pair-state is $\Delta_F \approx 120\,\mathrm{MHz}$.

6 Dipole-mediated energy transport in Rydberg-gases

This chapter is partially based on the following publication:

Observing the dynamics of dipole-mediated energy transport by interaction enhanced imaging
G. Günter, H. Schempp, M. Robert-de-Saint-Vincent, V. Gavryusev, S. Helmrich, C.S. Hofmann, S. Whitlock, M. Weidemüller
Science **342**, 954 (2013)

Watching a many-body quantum system evolve under the influence of well controlled interactions is the basic essence of Feynman's vision for a quantum simulator [Fey82], which could be used to address fundamental questions about coherent-quantum and open-system dynamics in diverse settings [Bar11, Lan11, Wei10]. One such question is the nature of energy transfer in real physical systems, such as complex chemical reactions, excitonic transport in organic semiconductors [Naj10] and molecular aggregates [Oij99, Gus01] or photosynthetic light-harvesting complexes [Lee07, Eng07, Sar10]. In these systems, both disorder and the environment play crucial roles.

Ultracold atomic gases offer a unique setting to tackle these kinds of problems with full access to the microscopic and macroscopic degrees of freedom [Kar09, Lew07, Wei11, Blo12]. Rydberg atoms possess exceptionally large dipole moments and long-range quantum-state changing interactions similar to those found in molecules (cf. Ch. 2). This renders them a natural candidate to study the effects of dipolar energy transfer. First evidence of Rydberg energy exchange was observed in the spectral broadening of optical transitions [And98, Mou98, And02] and more recently by studies of ionizing collisions [Li05], transfer of Rydberg state populations [Wes06, Dit08] and by optical Ramsey interferometry [Nip12]. For narrowband laser excitation, the Rydberg blockade effect, in which the presence of a single Rydberg atom strongly suppresses subsequent excitation of additional atoms in its vicinity (cf. Sec. 2.1.4) is expected to introduce interesting new dynamical features. So far however, the direct observation of Rydberg energy transport has remained out of reach due to the difficulty in spatially resolving the Rydberg atoms.

Here, we apply the novel imaging scheme described in Ch. 4 and Ch. 5 to study resonant energy transport dynamics of strongly-interacting Rydberg states. We discover that for Rydberg atoms in certain states, the spatial distribution of Rydberg atoms

is not stationary, but grows while the imaging light is on. This is a result of dipolar exchange interaction between the Rydberg atoms and the surrounding background gas. In addition the continuous observation of the excitation transport in the imaging process acts as an environment for the transport dynamics. We show that the transport dynamics can be controlled through the interactions and the coupling to the environment via the background gas. This illustrates the potential of ultracold Rydberg gases as a model system for investigations of dipolar transport phenomena.

The chapter is structured as follows: first, the observed transport dynamics of Rydberg excitations is presented and discussed. Then, we explain how exchange interactions between Rydberg atoms can mediate transport of Rydberg excitations in our system and how the continuous observation effects the transport dynamics. We provide a simple model which captures the main features of the dipolar transport and allows us to estimate transport parameters. Finally, building on the control possible in the presented system, we discuss perspectives for future investigations.

6.1 Transport dynamics during imaging

In the experiments, we discover that the spatial distribution of Rydberg atoms for certain Rydberg states is not stationary. Exciting impurity Rydberg atoms in the $|i\rangle \equiv |38S\rangle$ state and coupling the bath of surrounding atoms to the $|p\rangle \equiv |37S\rangle$ state, we find that the spatial distribution of impurities grows during the imaging process. The two involved Rydberg states have an interesting property, namely they exhibit state exchange interactions. The pair state $|38S\rangle \otimes |37S\rangle$ couples to the exchange-symmetric $|37P\rangle \otimes |37P\rangle$ state which mediates by the following process

$$\left|38S_{1/2}\right\rangle \otimes \left|37S_{1/2}\right\rangle \leftrightarrows \left|37P_{3/2}\right\rangle \otimes \left|37P_{3/2}\right\rangle \leftrightarrows \left|37S_{1/2}\right\rangle \otimes \left|38S_{1/2}\right\rangle \tag{6.1}$$

exchange of the $|38S\rangle$ and $|37S\rangle$ excitations. At an electric field of $\sim 1.8\,\mathrm{V/cm}$ [Rya10] the three pair states are degenerate and exhibit dipolar coupling with $C_3 = 2\pi \times 1.6\ \mathrm{GHz}\,\mu\mathrm{m}^3$.

The left column of Fig. 6.1 (a) shows images of the impurity distribution for different exposure times t_{exp}. The distribution is seen to expand horizontally as a function of the imaging exposure time. Expansion in the vertical direction is not observed due to the smaller size of the EIT coupling beam in this direction as indicated by the schematic at the top of Fig. 6.1 (a). In addition to the growing width, we observe a slight decay of the number of additional absorbers N_{add} which we can attribute to the lifetime of the $|38S\rangle$ Rydberg state ($\approx 30\,\mu$s)[Bet09]. To perform a quantitative analysis of the dynamics, we extract the second central moment σ_x^2 of the imaged distributions as a function of the exposure time. As shown in Fig. 6.1 (b), σ_x^2 grows approximately linearly.

To extract the diffusion coefficient D from the measured width σ_x, we have to take into account that our images with varying exposure time provide the time-integrated impurity distribution. Assuming an initial Gaussian distribution of impurities with am-

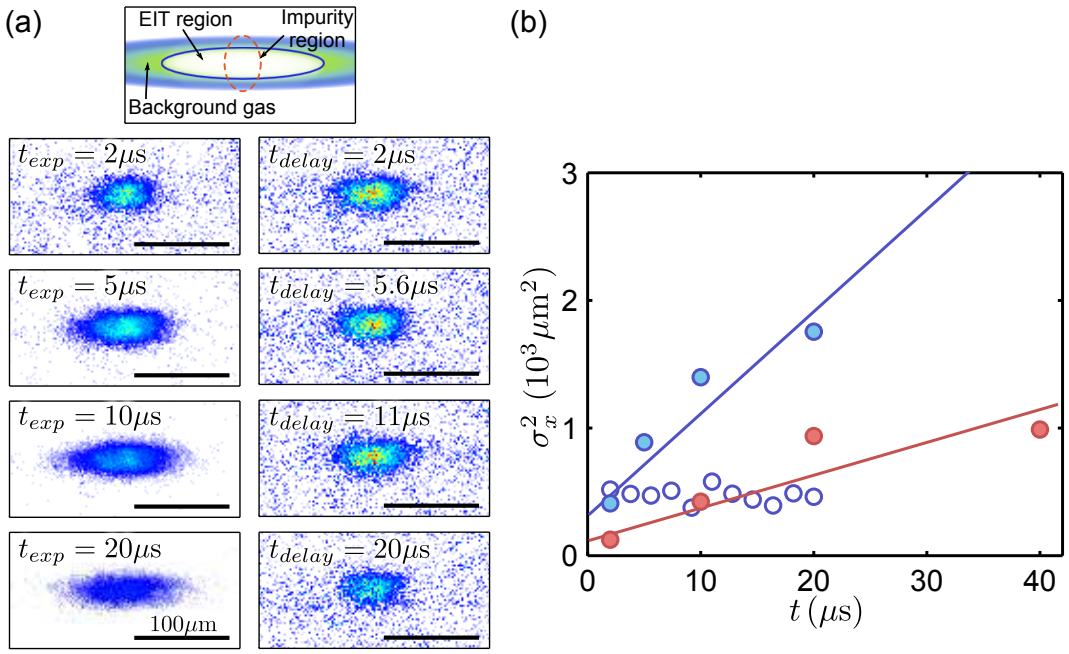

Figure 6.1: Diffusion of Rydberg-impurities. (a) The top sketch shows the experimental geometry indicating the initial position of the impurities and the imaging region. The images in the left column show the additional optical density reflecting the impurity distribution for different exposure times t_{exp} (images are averaged over 50 realizations). The strong exchange interactions between impurities and probe atoms lead to an expansion of the Rydberg distribution with the exposure time. In comparison, the images in the right column taken for different delay times t_{delay} with a fixed exposure of 2 μs show no growth of the distribution (images are averaged over 30 realizations). All images are taken on the Förster resonance and are displayed with a fixed color scale. (b) The squared width of the distribution σ_x^2 increases approximately linearly with time. On the Förster resonance (full blue circles) the expansion is faster than off resonance (full red circles). For comparison, open blue circles show σ_x^2 on the Förster resonance for fixed exposure time (2 μs), but with different delay times between the excitation and image acquisition.

plitude A_0 and width σ_0 together with diffusive expansion, the horizontal distribution obtained in an image with an exposure time t_{exp} is given by

$$\frac{A_0}{\sqrt{2\pi}t_{exp}}\int_0^{t_{exp}}\frac{1}{\sqrt{2Dt+\sigma_0^2}}e^{-\frac{x^2}{2\left(2Dt+\sigma_0^2\right)}}\,\mathrm{dt}\ . \tag{6.2}$$

The second moment σ_x^2 of the time-integrated distribution is

$$\sigma_x^2 = \sigma_0^2 + Dt\ , \tag{6.3}$$

which allows us to directly extract the diffusion coefficient D from the distributions in the images. On the Förster resonance, we find $D = 80 \pm 13\,\mu\mathrm{m}^2/\mu\mathrm{s}$.

To investigate the role of the continuous observation which acts as environment on the observed dynamics, we also record images with a fixed exposure time of $2\,\mu\mathrm{s}$, but with different times t_{delay} between impurity excitation and image acquisition during which $\Omega_p = \Omega_c = 0$ (see Fig. 5.1 (c) for the pulse sequence). The obtained images are shown in the right column of Fig. 6.1 (a). Here, we observe no growth of the distribution. Thus, this demonstrates that mechanical forces do not play a significant role and that the dynamics can be controlled by modifying the environment via the laser fields.

Finally, we study transport in the regime of off-resonant exchange interactions. Earlier experiments under these conditions observed spectral broadening and rapid dephasing of coherent state transfer [And98, Mou98, And02] which was too high to be explained by the off-resonant process in Eq. (6.4) alone. This was attributed to secondary processes resulting in enhanced spatial diffusion which we can now directly observe. By setting the electric field to zero we tune the Förster defect to $\Delta_F = 100\,\mathrm{MHz}$. Here, we expect weaker impurity-probe exchange interactions and a change in the character of the interactions to van der Waals type. As shown in Fig. 6.1 (b) we observe a slower broadening of the distribution and measure a diffusion coefficient $D = 26 \pm 6\,\mu\mathrm{m}^2/\mu\mathrm{s}$.

As we will discuss in the following, the observed diffusion is much faster than expected from simple estimates. This indicates that the diffusion involves additional processes such as the always resonant secondary process $|37S\rangle \otimes |37P\rangle \rightleftarrows |37P\rangle \otimes |37S\rangle$, and that spatial diffusion of secondary $|nP\rangle$ excitations plays an important role for the observed Rydberg state dynamics and the energy transfer.

6.2 Environment assisted transport

To understand the observed transport dynamics, we here identify important features of our system. Based on these basic considerations, we provide a simple model that allows us to estimate transport parameters like diffusion coefficients which are then compared to the experimental findings.

As already pointed out in the last section, the main ingredient for the observed exci-

tation transport is the strong dipolar state exchange interaction between the impurity and the probe atoms (cf. Sec. 2.1.3). This interaction leads to an excitation transfer of the kind

$$|i\rangle \otimes |p\rangle \rightleftarrows |p\rangle \otimes |i\rangle \,. \tag{6.4}$$

Typically, when transport of excitations is discussed in the framework of Rydberg gases, transfer of excitation from one Rydberg atom to another Rydberg atom is considered [Mül07, Wüs10]. In our system, we first excite atoms in the state $|i\rangle$ and then couple the bath of background atoms to the state $|p\rangle$ via a two-photon laser coupling. Thus, the probe atoms that are dressed by the imaging fields under EIT-conditions interact with the impurities via their Rydberg $|p\rangle$-state admixture. Due to the exchange property of the interactions, this leads to a transfer of the impurity excitations to the surrounding probe atoms. However, the Rydberg-Rydberg interactions not only induce excitation transfer of the impurity excitation, but as discussed within the framework of the imaging method result in an interstate blockade. The interstate blockade strongly suppresses the $|p\rangle$-state population in a volume characterized by the interstate blockade radius R_{ip} around the impurity which suppresses transfer to these atoms. This together with the continuous observation of the transport dynamics in the imaging process, differentiate our system from excitation transport in other systems. In particular, the spatial correlations due to the Rydberg blockade and the dissipation induced by the scattering of probe light, which acts as an environment, have a strong impact on the intrinsically coherent transfer mechanism.

6.2.1 A simple model

To attempt to understand how the transport dynamics is effected by the blockade and the continuous projection, we consider the following model. We consider the evolution of a single impurity atom embedded in a bath of background atoms which exhibits coherent state exchange interactions with all surrounding atoms. The hopping frequency $\omega_{hop}(r)$ between the impurity and a single atom at distance r depends on the exchange interaction $V_{ip}(r)$ and on the population $\rho_{pp}(r)$ of the probe Rydberg state $|p\rangle$ of the bath atom. The latter is effected by the presence of the impurity and depends on the laser fields, which allows to externally control the hopping dynamics. The presence of the impurity not only alters the probe Rydberg population of the bath atoms, but is also responsible for a finite population $\rho_{ee}(r)$ of the intermediate state caused by the interstate blockade. This results in light scattering from each probe atom with the rate $\Gamma_e \rho_{ee}(r)$. The light scattering by all probe atoms surrounding the impurity causes a measurement-induced environmental decoherence γ_{env} of the system. Therefore, the decoherence rate is expected to be on the order $\gamma_{env} \sim A\,\gamma_{2lvl}$, where γ_{2lvl} is the scattering rate of a two-level atom and A is the number of effective two-level absorbers induced by the impurity. Hence, the atomic density n_a and the probe Rabi-frequency Ω_p allow to control the environmental decoherence rate independent of ω_{hop} which shows that the key parameters in our system can be controlled independently.

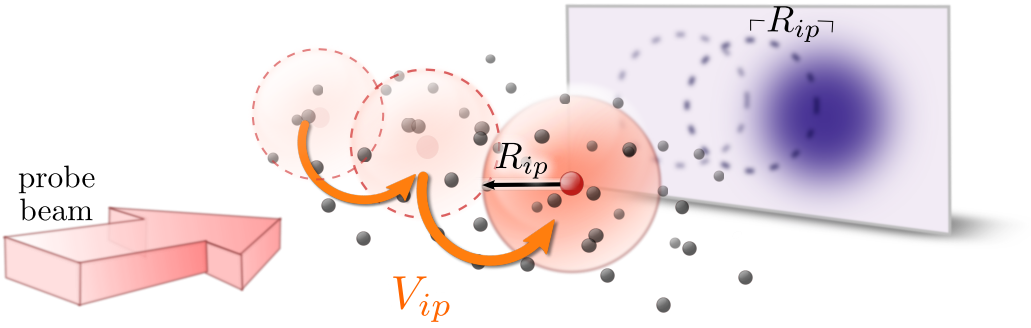

Figure 6.2: Schematic illustration of the environment assisted transport. The Rydberg impurity (red sphere) is embedded in a bath of probe atoms. The surrounding laser-dressed probe atoms interact with the impurity via state-exchanging Rydberg-Rydberg interactions V_{ip}. Far from the impurity the probe and the coupling laser (not shown) prepare the atoms in the dark state which contains a significant Rydberg fraction and allows excitation hopping to these atoms. Within the blockade radius R_{ip} the Rydberg interactions shift the probe Rydberg state. On the one hand, this leads to a suppression of the probe Rydberg population and concomitant suppression of hopping to these atoms. On the other hand, it breaks the EIT-condition for the atoms in the vicinity of the impurity which results in strong light scattering and continuous probing of the excitation transfer process.

To describe the system more quantitatively, we use the following heuristic model. Motivated by the picture outlined above, we assume the coherent hopping rate is $\omega_{hop}(r) \simeq 2\,V_{ip}(r)\rho_{pp}(r)$ as the exchange interaction couples the impurity and a probe atom via the population of the probe atom in the $|p\rangle$-state. The decoherence rate introduced by the ensemble of scatters surrounding the impurity is taken as the sum of the individual scattering rates $\gamma_{env} = \sum_i \Gamma_e \rho_{ee}^{(i)}(r)$, where the sum runs over all probe atoms. We have numerically checked the given simple model for two atoms. Solving the full quantum dynamics of two atoms including the levels $\{|g\rangle, |e\rangle, |p\rangle, |i\rangle, \}$, we find fairly good agreement of the simple model with the full calculation in the overdamped regime ($\gamma_{env} \gg \omega_{whop}$). In the following, we apply this simple model, which can be extended to systems involving many particles, to estimate transport parameters.

For typical parameters in our experiment, we estimate that γ_{env} is about 150 times higher than the maximum value of $\omega_{hop}(r)$. Therefore, we expect classical hopping to occur with a rate $\Gamma_{hop}(r) \simeq \omega_{hop}^2(r)/\gamma_{env}$ to each of the neighbouring atoms[1]. The competition between the interstate Rydberg blockade, which suppresses the probe Rydberg population close to the impurity, and the decreasing exchange interaction as a function of distance, results in a preferred hopping distance $r_{hop} \sim R_{ip}$ (see Fig. 6.3).

[1]The classical hopping rate Γ_{hop} can be derived considering a coupled two-level system with large dephasing. Adiabatic elimination of the coherences yields a rate model for the population with exchange rate Γ_{hop}.

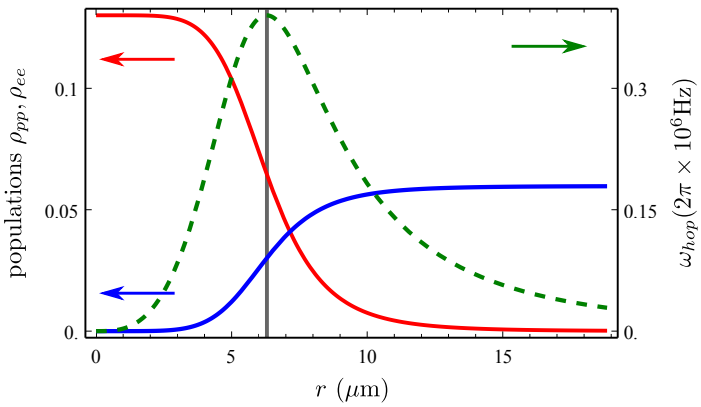

Figure 6.3: Probe atom populations as a function of distance to the impurity. The continuous blue and red curves show the populations $\rho_{pp}(r)$ and $\rho_{ee}(r)$, respectively (axis on the left). The vertical line marks the blockade radius R_{ip}^{dd} at which the Rydberg state population is suppressed by a factor of two by the interactions. The dashed green curve shows the hopping frequency $\omega_{hop}(r)$ which due to the competition between the low-distance suppression of the Rydberg population and the long-distance decay of the interaction presents a maximum approximately at R_{ip}^{dd} (right axis). The curves are calculated for $\Omega_p = 2\pi \times 2.2\,\mathrm{MHz}$, $\Omega_c = 2\pi \times 9\,\mathrm{MHz}$ and $C_3 = 2\pi \times 1.6\,\mathrm{GHz}\,\mu\mathrm{m}^3$.

This introduces an intrinsic scale, similar to that of self-assembled systems. As we anticipate classical hopping to dominate the transport process, the impurity distribution is expect to grow diffusively. Hence, we expect the width of the impurity distribution in each direction $\sigma(t)$ to grow as $\sigma^2(t) = \sigma_0^2 + 2Dt$, where σ_0 is the initial size of the distribution and D is a diffusion coefficient. In the following, we calculate diffusion coefficients for the case of dipolar and van der Waals energy transport.

Dipolar energy transfer

On or close to a Förster resonance, the impurity and the probe atoms interact via dipolar exchange $V_{ip}(r) = V_{dd}(r) = C_3/r^3$ (cf. Sec. 2.1.3). This interaction is responsible for a coherent excitation transfer of the impurity excitation to a probe atom dressed by the laser fields with the hopping frequency $\omega_{hop}(r) = 2\,V_{dd}(r)\rho_{pp}(r)$, as well as for a finite population $\rho_{ee}(r)$ of the intermediate state of the probe atom. To evaluate ρ_{pp} and ρ_{ee}, we assume stationary states for laser-driven probe atoms and include the effect of the interaction as a level shift $\Delta = V_{dd}(r)$ of the probe Rydberg state. In the weak probe limit ($\Omega_p \ll \Omega_c, \Gamma_e$), neglecting laser linewidths and decay of the Rydberg state,

we obtain

$$\rho_{pp}(r) = \frac{\Omega_p^2\Omega_c^2}{\Omega_c^4 + 4V_{dd}(r)^2\Gamma_e^2} \quad \text{and} \quad \rho_{ee}(r) = \frac{4V_{dd}(r)^2\Omega_p^2}{\Omega_c^4 + 4V_{dd}(r)^2\Gamma_e^2} \ . \tag{6.5}$$

In Fig. 6.3 both populations are shown, from which two observations can be made: First, we observe that within a sphere with a radius of approximately $R_{ip}^{dd} = (2\Gamma_e C_3/\Omega_c^2)^{1/3}$, the Rydberg population is highly suppressed. As a consequence of this and the rapidly decreasing strength of the exchange interaction with distance, the hopping frequency $\omega_{hop}(r)$ presents a peaked maximum at approximately R_{ip}^{dd} . This introduce a preferred hopping distance. Second, we observe that within the same sphere the atoms present a significant population of the intermediate state and thus strongly scatter light.

The transport dynamics results from the coherent hopping process of the impurity to all of the neighbouring atoms, damped by the light scattering of the ensemble of atoms in the vicinity of the impurity. The classical hopping rate $\Gamma_{hop}(r) = \omega_{hop}^2(r)/\gamma_{env}$ falls off as $1/r^6$. To obtain the total hopping rate Γ_{hop}^{tot} and the mean square hopping distance r_{hop}, we spatially integrate the classical hopping rate assuming a homogeneous three dimensional atomic density and find $\Gamma_{hop}^{tot} \simeq \Omega_p^2/2\Gamma_e$ and $r_{hop} = \sqrt{\langle \vec{r}^{\,2}\rangle} \simeq \sqrt{10/3}\, R_{ip}^{dd}$. The diffusion coefficient in three dimensions $D = \langle \vec{r}^{\,2}\rangle \Gamma_{hop}^{tot}/6$ then becomes

$$D \simeq \frac{5}{18}\left(R_{ip}^{dd}\right)^2 \frac{\Omega_p^2}{\Gamma_e} \ . \tag{6.6}$$

For the parameters corresponding to the measurement on the Förster resonance, $\Omega_p = 2\pi \times (2.2 \pm 0.3)\,\mathrm{MHz}$, $\Omega_c = 2\pi \times (9 \pm 1)\,\mathrm{MHz}$, $C_3 = 2\pi \times 1.6\,\mathrm{GHz}\,\mu\mathrm{m}^3$ and $n = (4.7 \pm 0.5) \times 10^{10}\,\mathrm{cm}^{-3}$, we find an interstate blockade radius $R_{ip}^{dd} = 6.3 \pm 0.5\,\mu\mathrm{m}$ and an expected diffusion coefficient $D = 55 \pm 23\,\mu\mathrm{m}^2/\mu\mathrm{s}$, where the stated uncertainty for the diffusion coefficient is dominated by the calibration of Ω_p. This is in fair agreement with the measured diffusion coefficient $D = 80 \pm 13\,\mu\mathrm{m}^2/\mu\mathrm{s}$.

Van der Waals energy transfer

In the case of off-resonant exchange interactions $V_{ip}(r) = V_{vdW}(r) = C_6/r^6$, the expressions for γ_{env} and Γ_{hop} determined analogously to the dipolar case do not present a simple analytical form. Therefore, we employ a hard sphere picture: Within the interstate blockade radius $R_{ip}^{vdw} = (2\Gamma_e C_6/\Omega_c^2)^{1/6}$, we assume perfect blockade and set $\rho_{ee} \simeq \Omega_p^2/\Gamma_e^2$ and $\rho_{pp} \simeq 0$. Outside the blockade sphere ($r \geq R_{ip}^{vdw}$), the probe atoms are assumed to be in the dark state and we use $\rho_{ee} \simeq 0$ and $\rho_{pp} \simeq \Omega_p^2/\Omega_c^2$. Using this approximation spatial integration of $\Gamma_{hop}(r)$ which decays with $1/r^{12}$ yields $\Gamma_{hop}^{tot} \simeq \Omega_p^2/3\Gamma_e$ and $r_{hop} \simeq \sqrt{9/7} R_{ip}^{vdw}$. Consequently, we again obtain a simple expression for the diffusion coefficient:

$$D \simeq \frac{1}{14}\left(R_{ip}^{vdW}\right)^2 \frac{\Omega_p^2}{\Gamma_e} \ . \tag{6.7}$$

The differences as compared to the dipolar exchange are the numerical pre-factor and the strongly reduced blockade radius. The blockade radii on and off the Förster resonance are related by $R_{ip}^{vdw}/R_{ip}^{dd} = (\Omega_c^2/2\Gamma_e\Delta_F)^{1/6} \approx 0.6$ for typical parameters in the experiment.

Using the parameters from the experiments detuned from the Förster resonance, $\Omega_p = 2\pi \times (1.8 \pm 0.2)\,\mathrm{MHz}$, $\Omega_c = 2\pi \times (9 \pm 1)\,\mathrm{MHz}$, $\Delta_F = 2\pi \times 100\,\mathrm{MHz}$, $n = (8.0 \pm 0.8) \times 10^{10}/\mathrm{cm}^3$, we expect diffusion with a coefficient $D = 3.0 \pm 0.9\,\mu\mathrm{m}^2/\mu\mathrm{s}$. Note that the direct numerical integration of γ_{env} and Γ_{hop} without hard sphere approximation gives a similar value $D = 2.2\,\mu\mathrm{m}^2/\mu\mathrm{s}$.

This is almost an order of magnitude slower than the measured diffusion coefficient of $D = 26 \pm 6\,\mu\mathrm{m}^2/\mu\mathrm{s}$. This shows that the observed diffusion involves additional processes. Creation of atoms in the $|37P\rangle$ in the exchange process for instance, might lead to diffusion of these atoms by the always resonant exchange process $|37S\rangle \otimes |37P\rangle \rightleftarrows |37P\rangle \otimes |37S\rangle$ which is not distinguished from the diffusion of $|38S\rangle$ atoms in the imaging process. This indicates that secondary process play an important role for the observed Rydberg state dynamics and the energy transfer.

6.3 Perspectives

In future work, it will be possible to investigate the transition to coherent-quantum dynamics in many-body systems. By creating probe Rydberg atoms in a short excitation pulse, or by detuning the EIT lasers from the intermediate state, decoherence via photon scattering can be suppressed while maintaining the preferred distance for hopping given by the blockade radius. This will allow for the study of excitonic behaviour, in which impurities evolve as delocalized superposition states. In this regime, transport should be completely different, leading to localisation or enhanced transport which can be controlled through the dimensionality, degree of disorder and dissipation in the system [Rob04]. By switching back to resonant probing this evolution could be observed. This provides an ideal platform for benchmarking current theories used to explain energy transport in complex systems such as light harvesting complexes, where for example the competition between mechanical and excitonic transport and the role of interactions are still open questions [Col13].

7 Conclusion

In this thesis, the interplay between light and strongly interacting ultracold Rydberg gases has been investigated. Considering the achievements presented in this thesis together with other advances in the field of Rydberg physics, I see three new research directions beginning to emerge:

Rydberg nonlinear optics

The mapping of photons on matter excitations in an interacting gas, as demonstrated in this thesis, allows to realize strong effective photon-photon interactions and sets the basis for the new field of Rydberg nonlinear optics. Our experiments, in which we have investigated the nonlinear optical response of the atomic gas as well as the correlations between the dark-state polaritons [Hof13b], together with other experiments performed in the past two years [Dud12b, Pey12, Max13] mark first steps in this emerging field. Since the photon-photon interactions are mediated by the Rydberg interactions, this allows us to realize photonic interactions with repulsive or attractive, dissipative or elastic and even non-local character [Sev11, Pri13]. These interactions which are strong on the level of individual photons open up new possibilities to deterministically control and manipulate single photons [Pri13]. This paves the way for novel applications in quantum information science, such as the implementation of photonic quantum gates for quantum computing [Gor11, Fri05, Sha11] or deterministic single photon sources for quantum communication [Dud12b, Pey12]. The unique ability of our experiment to access both degrees of freedom might provide new insight into this strongly coupled light-matter system, that combined with new theoretical models, might ultimately form the basis for new technologies. So far, however, a full theoretical description of our experiments is still missing and a full quantized theory including strong interactions remains an ongoing challenge. Moreover, the strong effective photon-photon interactions might allow to study new phenomena involving many-body states of light [Car13]. Strongly correlated streams of photons, produced for example using the photon blockade in Rydberg gases, can be regarded as quantum phases of light and have led to theoretical investigations of photonic superfluids [Chi99], Tonks-Girardeau gases of photons [Cha08] or Bose glasses of light [Ros07]. Compared to particles like atoms and electrons, the composite nature of the interacting photons inherently makes this system an open quantum system with new properties [Car13]. This results in a variety of new phenomena like non-equilibrium phase transitions which would be interesting to study in our experiment.

Investigation of many-body Rydberg states on the level of single particles

So far, studies of Rydberg ensembles have been mainly restricted to cloud average properties. This is now changing with first imaging techniques being demonstrated [Sch11, Sch12, McQ13, Loc13]. These techniques, including the novel imaging technique presented in this thesis [Gün12, Gün13], open the way for investigations of many-body Rydberg states on the level of single particles. On the one hand, this will give new insights into effects like the Rydberg blockade, interaction-driven dynamics in Rydberg gases [Amt07] or the formation of Rydberg aggregates [Sch13b]. On the other hand, it might allow to investigate so far unexplored phenomena like quantum crystals of Rydberg atoms [Poh10, Bij11]. For instance the ground state of Rydberg atoms under continuous laser driving is expected to show a quantum phase transition which belongs to a novel universality class [Wei08, Sch10a]. The access to the microscopic degrees of freedom of the Rydberg gas might allow to investigate the phase diagram of this system. Additionally, by mapping these many-body states onto the light field new non-classical light states like trains of single photons might be created [Poh10].

Quantum simulation with Rydberg atoms

Rydberg atoms with their strong dipolar interactions are ideal candidates to study dipolar transport phenomena. Dipolar energy transport plays an important role in diverse fields ranging from chemical reactions over exciton transport in organic semiconductors [Naj10] to photosynthetic light-harvesting complexes [Col13]. Due to their inherent complexity, these systems are hard to control and their understanding is an ongoing challenge. The experiments presented in Ch. 6 demonstrate first direct observations of dipolar transport in Rydberg gases [Gün13] and represent one of the first steps towards quantum simulation with Rydberg atoms. Rydberg gases provide an ideal platform for benchmarking current theories used to explain dipolar energy transport in the aforementioned, complex systems. In addition, studies of energy transport in Rydberg gases might help to elucidate open questions like the role of entanglement or effects of the competition between mechanical and excitonic transport in real physical systems [Col13]. Furthermore, Rydberg atoms have been proposed as a candidate for the implementation of a universal quantum simulator [Wei10, Mül12]. Such a device might allow to simulate spin models with many-particle interactions which are important in theoretical models like e.g. lattice gauge theories. In addition, the combination of Rydberg atoms with optical lattices might allow to emulate condensed matter phenomena like electron-phonon interactions [Hag12]. The addition of the light field which introduce a controlled environment will offer new degrees of freedom to control dissipation in the system, allowing for the simulation of open quantum systems. Needless to say, the future is bright!

Bibliography

[Abe09] R. P. Abel, A. K. Mohapatra, M. G. Bason, J. D. Pritchard, K. J. Weatherill, U. Raitzsch, C. S. Adams, *Laser frequency stabilization to excited state transitions using electromagnetically induced transparency in a cascade system*, Applied Physics Letters **94**(7), 071107 (2009).

[Abe11] R. P. Abel, C. Carr, U. Krohn, C. S. Adams, *Electrometry near a dielectric surface using Rydberg electromagnetically induced transparency*, Phys. Rev. A **84**, 023408 (Aug 2011).

[Alz76] G. Alzetta, A. Gozzini, L. Moi, G. Orriols, *An experimental method for the observation of r.f. transitions and laser beat resonances in oriented Na vapour*, Il Nuovo Cimento B Series 11 **36**(1), 5–20 (1976).

[Amt07] T. Amthor, M. Reetz-Lamour, S. Westermann, J. Denskat, M. Weidemüller, *Mechanical Effect of van der Waals Interactions Observed in Real Time in an Ultracold Rydberg Gas*, Phys. Rev. Lett. **98**, 023004 (2007).

[Amt10] T. Amthor, C. Giese, C. S. Hofmann, M. Weidemüller, *Evidence of Antiblockade in an Ultracold Rydberg Gas*, Phys. Rev. Lett. **104**(1), 013001 (Jan 2010).

[And98] W. R. Anderson, J. R. Veale, T. F. Gallagher, *Resonant Dipole-Dipole Energy Transfer in a Nearly Frozen Rydberg Gas*, Phys. Rev. Lett. **80**, 249–252 (Jan 1998).

[And02] W. R. Anderson, M. P. Robinson, J. D. D. Martin, T. F. Gallagher, *Dephasing of resonant energy transfer in a cold Rydberg gas*, Phys. Rev. A **65**, 063404 (Jun 2002).

[Ång55] A. J. Ångström, *XLVIII. Optical researches*, Philosophical Magazine Series 4 **9**(60), 327–342 (1855).

[Arg13] M. Argus, *Electric Field Optimization of a Rydberg Atom Experiment*, Bachelor Thesis, Department of Physics and Astronomy, University of Heidelberg (2013).

[Ate09] C. Ates, *Anregungsdynamik ultrakalter Rydberggase*, Dissertation, MPIKS Dresden (2009).

[Ate11] C. Ates, S. Sevinçli, T. Pohl, *Electromagnetically induced transparency in strongly interacting Rydberg gases*, Phys. Rev. A **83**, 041802 (Apr 2011).

[Baj03] M. Bajcsy, A. S. Zibrov, M. D. Lukin, *Stationary pulses of light in an atomic medium*, Nature **426**(6967), 638–641 (2003).

[Bak09] W. S. Bakr, J. I. Gillen, A. Peng, S. Fölling, M. Greiner, *A quantum gas microscope for detecting single atoms in a Hubbard-regime optical lattice*, Nature **462**(7269), 74–77 (2009).

[Bal85] J. J. Balmer, *Notiz über die Spectrallinien des Wasserstoffs*, Annalen der Physik **261**(5), 80–87 (1885).

[Bar04] M. Bartenstein, A. Altmeyer, S. Riedl, S. Jochim, C. Chin, J. H. Denschlag, R. Grimm, *Crossover from a Molecular Bose-Einstein Condensate to a Degenerate Fermi Gas*, Phys. Rev. Lett. **92**, 120401 (Mar 2004).

[Bar11] J. T. Barreiro, M. Müller, P. Schindler, D. Nigg, T. Monz, M. Chwalla, M. Hennrich, C. F. Roos, P. Zoller, R. Blatt, *An open-system quantum simulator with trapped ions*, Nature **470**(7335), 486–491 (2011).

[Bar12] F. Bariani, Y. O. Dudin, T. A. B. Kennedy, A. Kuzmich, *Dephasing of Multiparticle Rydberg Excitations for Fast Entanglement Generation*, Phys. Rev. Lett. **108**, 030501 (Jan 2012).

[Bau10] K. Baumann, C. Guerlin, F. Brennecke, T. Esslinger, *Dicke quantum phase transition with a superfluid gas in an optical cavity*, Nature **464**(7293), 1301–1306 (2010).

[Ben09] V. Bendkowsky, B. Butscher, J. Nipper, J. P. Shaffer, R. Löw, T. Pfau, *Observation of ultralong-range Rydberg molecules*, Nature **458**, 1005 – 1008 (04 2009).

[Bet93] E. Betzig, R. J. Chichester, *Single Molecules Observed by Near-Field Scanning Optical Microscopy*, Science **262**(5138), 1422–1425 (1993).

[Bet09] I. I. Beterov, I. I. Ryabtsev, D. B. Tretyakov, V. M. Entin, *Quasiclassical calculations of blackbody-radiation-induced depopulation rates and effective lifetimes of Rydberg nS, nP, and nD alkali-metal atoms with $n \leq 80$*, Phys. Rev. A **79**, 052504 (May 2009).

[Bij11] R. M. W. van Bijnen, S. Smit, K. A. H. van Leeuwen, E. J. D. Vredenbregt, S. J. J. M. F. Kokkelmans, *Adiabatic formation of Rydberg crystals with chirped laser pulses*, Journal of Physics B: Atomic, Molecular and Optical Physics **44**(18), 184008 (2011).

[Bij13] R. M. W. van Bijnen, *Quantum Engineering with Ultracold Atoms*, Dissertation, Technische Universiteit Eindhoven (2013).

[Blo08] I. Bloch, J. Dalibard, W. Zwerger, *Many-body physics with ultracold gases*, Rev. Mod. Phys. **80**, 885–964 (Jul 2008).

[Blo12] I. Bloch, J. Dalibard, S. Nascimbène, *Quantum simulations with ultracold quantum gases*, Nature Physics **8**(4), 267–276 (2012).

[Boc10] J. Bochmann, M. Mücke, C. Guhl, S. Ritter, G. Rempe, D. L. Moehring, *Lossless State Detection of Single Neutral Atoms*, Phys. Rev. Lett. **104**, 203601 (May 2010).

[Boh13] N. Bohr, *I. On the constitution of atoms and molecules*, Philosophical Magazine Series 6 **26**(151), 1–25 (1913).

[Boi02] C. Boisseau, I. Simbotin, R. Côté, *Macrodimers: Ultralong Range Rydberg Molecules*, Phys. Rev. Lett. **88**, 133004 (Mar 2002).

[Bol91] K.-J. Boller, A. Imamolu, S. E. Harris, *Observation of electromagnetically induced transparency*, Phys. Rev. Lett. **66**, 2593–2596 (May 1991).

[Bou00] D. Bouwmeester, A. K. Ekert, A. Zeilinger, *et al.*, *The physics of quantum information*, Vol. 38 (Springer Berlin, 2000).

[Bou04] T. Bourdel, L. Khaykovich, J. Cubizolles, J. Zhang, F. Chevy, M. Teichmann, L. Tarruell, S. J. J. M. F. Kokkelmans, C. Salomon, *Experimental Study of the BEC-BCS Crossover Region in Lithium 6*, Phys. Rev. Lett. **93**, 050401 (Jul 2004).

[Bra11] N. Brahms, T. P. Purdy, D. W. Brooks, T. Botter, D. M. Stamper-Kurn, *Cavity-aided magnetic resonance microscopy of atomic transport in optical lattices*, Nature Physics **7**(8), 604–607 (2011).

[Bre07] F. Brennecke, T. Donner, S. Ritter, T. Bourdel, M. Kohl, T. Esslinger, *Cavity QED with a Bose-Einstein condensate*, Nature **450**, 268 (2007).

[Bro56] R. H. Brown, R. Twiss, *Correlation between photons in two coherent beams of light*, Nature **177**(4497), 27–29 (1956).

[Bus11] H. Busche, *Efficient loading of a magneto-optical trap for experiments with dense ultracold Rydberg gases*, Masters Thesis, Department of Physics and Astronomy, University of Heidelberg (2011).

[Car13] I. Carusotto, C. Ciuti, *Quantum fluids of light*, Rev. Mod. Phys. **85**, 299–366 (Feb 2013).

[Cha08] D. Chang, V. Gritsev, G. Morigi, V. Vuletic, M. Lukin, E. Demler, *Crystallization of strongly interacting photons in a nonlinear optical fibre*, Nature Physics **4**(11), 884–889 (2008).

[Chi99] R. Y. Chiao, J. Boyce, *Bogoliubov dispersion relation and the possibility of superfluidity for weakly interacting photons in a two-dimensional photon fluid*, Phys. Rev. A **60**, 4114–4121 (Nov 1999).

[Col13] E. Collini, *Spectroscopic signatures of quantum-coherent energy transfer*, Chem. Soc. Rev. **42**, 4932–4947 (2013).

[Com10] D. Comparat, P. Pillet, *Dipole blockade in a cold Rydberg atomic sample*, J. Opt. Soc. Am. B **27**, A208 (2010).

[Dei06] J. Deiglmayr, M. Reetz-Lamour, T. Amthor, S. Westermann, A. L. de Oliveira, M. Weidemüller, *Coherent excitation of Rydberg atoms in an ultracold gas*, Opt. Comm. **264**, 293 (2006).

[Del08] S. Deleglise, I. Dotsenko, C. Sayrin, J. Bernu, M. Brune, J.-M. Raimond, S. Haroche, *Reconstruction of non-classical cavity field states with snapshots of their decoherence*, Nature **455**(7212), 510–514 (2008).

[Dic54] R. H. Dicke, *Coherence in Spontaneous Radiation Processes*, Phys. Rev. **93**, 99–110 (Jan 1954).

[Dit08] C. S. E. van Ditzhuijzen, A. F. Koenderink, J. V. Hernández, F. Robicheaux, L. D. Noordam, H. B. v. L. van den Heuvell, *Spatially Resolved Observation of Dipole-Dipole Interaction between Rydberg Atoms*, Phys. Rev. Lett. **100**, 243201 (Jun 2008).

[Dub12] R. Dubessy, K. Merloti, L. Longchambon, P.-E. Pottie, T. Liennard, A. Perrin, V. Lorent, H. Perrin, *Rubidium-87 Bose-Einstein condensate in an optically plugged quadrupole trap*, Phys. Rev. A **85**, 013643 (Jan 2012).

[Dud12a] Y. O. Dudin, F. Bariani, A. Kuzmich, *Emergence of Spatial Spin-Wave Correlations in a Cold Atomic Gas*, Phys. Rev. Lett. **109**, 133602 (Sep 2012).

[Dud12b] Y. O. Dudin, A. Kuzmich, *Strongly Interacting Rydberg Excitations of a Cold Atomic Gas*, Science **336**(6083), 887–889 (2012).

[Ein05] A. Einstein, *Über einen die Erzeugung und Verwandlung des Lichtes betreffenden heuristischen Gesichtspunkt*, Annalen der Physik **322**(6), 132 (1905).

[Eis06] M. D. Eisaman, *Generation, Storage, and Retrieval of Nonclassical States of Light using Atomic Ensembles*, Dissertation, Harvard University (2006).

[Eng07] G. S. Engel, T. R. Calhoun, E. L. Read, T.-K. Ahn, T. Mančal, Y.-C. Cheng, R. E. Blankenship, G. R. Fleming, *Evidence for wavelike energy transfer through quantum coherence in photosynthetic systems*, Nature **446**, 782 (2007).

[Fab11] A. Faber, *All-optical formation of a rubidium Bose-Einstein condensate for experiments on interacting Rydberg atoms*, Masters Thesis, Department of Physics and Astronomy, University of Heidelberg (2011).

[Fey82] R. Feynman, *Simulating physics with computers*, International Journal of Theoretical Physics **21**(6-7), 467–488 (1982).

[Fir13] O. Firstenberg, T. Peyronel, Q.-Y. Liang, A. V. Gorshkov, M. D. Lukin, V. Vuletić, *Attractive photons in a quantum nonlinear medium*, Nature (2013).

[Fle00a] M. Fleischhauer, M. D. Lukin, *Dark-State Polaritons in Electromagnetically Induced Transparency*, Phys. Rev. Lett. **84**, 5094–5097 (May 2000).

[Fle00b] M. Fleischhauer, A. B. Matsko, M. O. Scully, *Quantum limit of optical magnetometry in the presence of ac Stark shifts*, Phys. Rev. A **62**, 013808 (Jun 2000).

[Fle02] M. Fleischhauer, M. D. Lukin, *Quantum memory for photons: Dark-state polaritons*, Phys. Rev. A **65**, 022314 (Jan 2002).

[Fle05] M. Fleischhauer, A. Imamoglu, J. P. Marangos, *Electromagnetically induced transparency: Optics in coherent media*, Rev. Mod. Phys. **77**, 633–673 (Jul 2005).

[Fle08] M. Fleischhauer, J. Otterbach, R. G. Unanyan, *Bose-Einstein Condensation of Stationary-Light Polaritons*, Phys. Rev. Lett. **101**, 163601 (Oct 2008).

[Fré27] V. Fréedericksz, A. Repiewa, *Theoretisches und Experimentelles zur Frage nach der Natur der anisotropen Flüssigkeiten*, Zeitschrift fur Physik **42**, 532–546 (1927).

[Fri05] I. Friedler, D. Petrosyan, M. Fleischhauer, G. Kurizki, *Long-range interactions and entanglement of slow single-photon pulses*, Phys. Rev. A **72**, 043803 (Oct 2005).

[Gae09] A. Gaetan, Y. Miroshnychenko, T. Wilk, A. Chotia, M. Viteau, D. Comparat, P. Pillet, A. Browaeys, P. Grangier, *Observation of collective excitation of two individual atoms in the Rydberg blockade regime*, Nature Physics **5**, 115– 118 (2009).

[Gal05] T. Gallagher, *Rydberg Atoms*, Cambridge Monographs on Atomic, Molecular and Chemical Physics (Cambridge University Press, 2005).

[Gal08] T. F. Gallagher, P. Pillet, *Dipole-Dipole Interactions of Rydberg Atoms*, in A. et al (Ed.), *Advances in Atomic, Molecular, and Optical Physics*, Vol. 56 of *Advances In Atomic, Molecular, and Optical Physics*, 161 – 218 (Academic Press, 2008).

[Gär13] M. Gärttner, J. Evers, *Nonlinear absorption and density-dependent dephasing in Rydberg electromagnetically-induced-transparency media*, Phys. Rev. A **88**, 033417 (Sep 2013).

[Geh10] R. Gehr, J. Volz, G. Dubois, T. Steinmetz, Y. Colombe, B. L. Lev, R. Long, J. Estève, J. Reichel, *Cavity-Based Single Atom Preparation and High-Fidelity Hyperfine State Readout*, Phys. Rev. Lett. **104**, 203602 (May 2010).

[Ger08] T. Gericke, P. Würtz, D. Reitz, T. Langen, H. Ott, *High-resolution scanning electron microscopy of an ultracold quantum gas*, Nature Physics **4**(12), 949–953 (2008).

[Gie11] M. Gierling, P. Schneeweiss, G. Visanescu, P. Federsel, M. Häffner, D. Kern, T. Judd, A. Günther, J. Fortágh, *Cold-atom scanning probe microscopy*, Nature nanotechnology **6**(7), 446–451 (2011).

[Gle07] S. Gleyzes, S. Kuhr, C. Guerlin, J. Bernu, S. Deleglise, U. B. Hoff, M. Brune, J.-M. Raimond, S. Haroche, *Quantum jumps of light recording the birth and death of a photon in a cavity*, Nature **446**(7133), 297–300 (2007).

[Gör01] A. Görlitz, J. M. Vogels, A. E. Leanhardt, C. Raman, T. L. Gustavson, J. R. Abo-Shaeer, A. P. Chikkatur, S. Gupta, S. Inouye, T. Rosenband, W. Ketterle, *Realization of Bose-Einstein Condensates in Lower Dimensions*, Phys. Rev. Lett. **87**, 130402 (Sep 2001).

[Gor11] A. V. Gorshkov, J. Otterbach, M. Fleischhauer, T. Pohl, M. D. Lukin, *Photon-Photon Interactions via Rydberg Blockade*, Phys. Rev. Lett. **107**, 133602 (Sep 2011).

[Gre02] M. Greiner, O. Mandel, T. Esslinger, T. W. Hänsch, I. Bloch, *Quantum phase transition from a superfluid to a Mott insulator in a gas of ultracold atoms*, Nature **415**(6867), 39–44 (2002).

[Gri09] A. Grier, M. Cetina, F. Oručević, V. Vuletić, *Observation of cold collisions between trapped ions and trapped atoms*, Physical review letters **102**(22), 223201 (2009).

[Gün09] G. Günter, A. A. Anappara, J. Hees, A. Sell, G. Biasiol, L. Sorba, S. De Liberato, C. Ciuti, A. Tredicucci, A. Leitenstorfer, *et al.*, *Sub-cycle switch-on of ultrastrong light–matter interaction*, Nature **458**(7235), 178–181 (2009).

[Gün12] G. Günter, M. Robert-de Saint-Vincent, H. Schempp, C. S. Hofmann, S. Whitlock, M. Weidemüller, *Interaction Enhanced Imaging of Individual Rydberg Atoms in Dense Gases*, Phys. Rev. Lett. **108**, 013002 (Jan 2012).

[Gün13] G. Günter, H. Schempp, M. Robert-de Saint-Vincent, V. Gavryusev, S. Helmrich, C. S. Hofmann, S. Whitlock, M. Weidemüller, *Observing the Dynamics of Dipole-Mediated Energy Transport by Interaction-Enhanced Imaging*, Science **342**(6161), 954–956 (2013).

[Gur12] J. H. Gurian, P. Cheinet, P. Huillery, A. Fioretti, J. Zhao, P. L. Gould, D. Comparat, P. Pillet, *Observation of a Resonant Four-Body Interaction in Cold Cesium Rydberg Atoms*, Phys. Rev. Lett. **108**, 023005 (2012).

[Gus01] D. Gust, T. A. Moore, A. L. Moore, *Mimicking Photosynthetic Solar Energy Transduction*, Accounts of Chemical Research **34**(1), 40–48 (2001).

[Häf05] H. Häffner, W. Hänsel, C. F. Roos, J. Benhelm, D. Chek-al kar, M. Chwalla, T. Korber, U. D. Rapol, M. Riebe, P. O. Schmidt, C. Becher, O. Guhne, W. Dur, R. Blatt, *Scalable multiparticle entanglement of trapped ions*, Nature **438**(7068), 643–646 (2005).

[Hag12] J. P. Hague, C. MacCormick, *Quantum simulation of electron–phonon interactions in strongly deformable materials*, New Journal of Physics **14**(3), 033019 (2012).

[Ham10] K. Hammerer, A. S. Sørensen, E. S. Polzik, *Quantum interface between light and atomic ensembles*, Rev. Mod. Phys. **82**, 1041–1093 (Apr 2010).

[Han06] J. Han, Y. Jamil, D. V. L. Norum, P. J. Tanner, T. F. Gallagher, *Rb nf quantum defects from millimeter-wave spectroscopy of cold* ^{85}Rb *Rydberg atoms*, Phys. Rev. A **74**, 054502 (Nov 2006).

[Har89] S. Haroche, D. Kleppner, *Cavity quantum electrodynamics*, Phys. Today **42**, 24 (1989).

[Har90] S. E. Harris, J. E. Field, A. Imamoğlu, *Nonlinear optical processes using electromagnetically induced transparency*, Phys. Rev. Lett. **64**, 1107–1110 (Mar 1990).

[Har12] *Nobel Prize in Physics 2012,* http://www.nobelprize.org/nobel_prizes/physics/laureates/2012/, (2012).

[Har13] S. Haroche, *Controlling photons in a box and exploring the quantum to classical boundary*, Bulletin of the American Physical Society **58** (2013).

[Hau99] L. V. Hau, S. E. Harris, Z. Dutton, C. H. Behroozi, *Light speed reduction to 17 metres per second in an ultracold atomic gas*, Nature **397**(6720), 594–598 (1999).

[Hei07] R. Heidemann, U. Raitzsch, V. Bendkowsky, B. Butscher, R. Löw, L. Santos, T. Pfau, *Evidence for Coherent Collective Rydberg Excitation in the Strong Blockade Regime*, Physical Review Letters **99**(16), 163601 (2007).

[Hel13] S. Helmrich, *Improving optical resolution by noise correlation analysis*, Masters Thesis, Department of Physics and Astronomy, University of Heidelberg (2013).

[Hen10] N. Henkel, R. Nath, T. Pohl, *Three-Dimensional Roton Excitations and Supersolid Formation in Rydberg-Excited Bose-Einstein Condensates*, Phys. Rev. Lett. **104**(19), 195302 (May 2010).

[Hof13a] C. Hofmann, *Emergence of correlations in strongly interacting ultracold Rydberg gases*, Dissertation, Universität Heidelberg (2013).

[Hof13b] C. S. Hofmann, G. Günter, H. Schempp, M. Robert-de Saint-Vincent, M. Gärttner, J. Evers, S. Whitlock, M. Weidemüller, *Sub-Poissonian Statistics of Rydberg-Interacting Dark-State Polaritons*, Phys. Rev. Lett. **110**, 203601 (May 2013).

[Hof13c] C. S. Hofmann, G. Günter, H. Schempp, R. de Saint-Vincent, S. Whitlock, M. Weidemüller, *Combined optical and population-based measurements of Rydberg electromagnetically induced transparency* (2013), in preparation.

[Hwa09] J. Hwang, M. Pototschnig, R. Lettow, G. Zumofen, A. Renn, S. Götzinger, V. Sandoghdar, *A single-molecule optical transistor*, Nature **460**(7251), 76–80 (2009).

[Ise10] L. Isenhower, E. Urban, X. L. Zhang, A. T. Gill, T. Henage, T. A. Johnson, T. G. Walker, M. Saffman, *Demonstration of a Neutral Atom Controlled-NOT Quantum Gate*, Phys. Rev. Lett. **104**, 010503 (Jan 2010).

[JR04] G. S. JP Reithmaier, A. Löffler, C. Hofmann, S. Kuhn, S. Reitzenstein, L. Keldysh, V. Kulakovskii, A. F. TL Reinecke, *Strong coupling in a single quantum dot–semiconductor microcavity system*, Nature **432**(7014), 197–200 (2004).

[Jul04] B. Julsgaard, J. Sherson, J. I. Cirac, J. Fiurášek, E. S. Polzik, *Experimental demonstration of quantum memory for light*, Nature **432**(7016), 482–486 (2004).

[Kar06] L. Karpa, M. Weitz, *A Stern–Gerlach experiment for slow light*, Nature Physics **2**, 332–335 (2006).

[Kar09] M. Karski, L. Förster, J.-M. Choi, A. Steffen, W. Alt, D. Meschede, A. Widera, *Quantum Walk in Position Space with Single Optically Trapped Atoms*, Science **325**(5937), 174–177 (2009).

[Ket99] W. Ketterle, D. Durfee, D. Stamper-Kurn, *Bose-Einstein Condensation in Atomic Gases: Proceedings of the International School of Physics (Enrico Fermi) Course Cxl*, Chapter Making, probing and understanding Bose-Einstein condensates, 95 – 113 (IOS Press, 1999).

[Kil07] T. Killian, T. Pattard, T. Pohl, J. Rost, *Ultracold neutral plasmas*, Physics Reports **449**, 77 – 130 (2007).

[Kim98] H. J. Kimble, *Strong interactions of single atoms and photons in cavity QED*, Physica Scripta **1998**(T76), 127 (1998).

[Kir13] G. Kirchmair, B. Vlastakis, Z. Leghtas, S. E. Nigg, H. Paik, E. Ginossar, M. Mirrahimi, L. Frunzio, S. Girvin, R. Schoelkopf, *Observation of quantum state collapse and revival due to the single-photon Kerr effect*, Nature **495**(7440), 205–209 (2013).

[Kuz97] A. Kuzmich, K. Mølmer, E. S. Polzik, *Spin Squeezing in an Ensemble of Atoms Illuminated with Squeezed Light*, Phys. Rev. Lett. **79**, 4782–4785 (Dec 1997).

[Lan11] B. P. Lanyon, C. Hempel, D. Nigg, M. Müller, R. Gerritsma, F. Zähringer, P. Schindler, J. T. Barreiro, M. Rambach, G. Kirchmair, M. Hennrich, P. Zoller, R. Blatt, C. F. Roos, *Universal Digital Quantum Simulation with Trapped Ions*, Science **334**(6052), 57–61 (2011).

[Lee07] H. Lee, Y.-C. Cheng, G. R. Fleming, *Coherence dynamics in photosynthesis: protein protection of excitonic coherence*, Science **316**(5830), 1462–1465 (2007).

[Lei03] D. Leibfried, R. Blatt, C. Monroe, D. Wineland, *Quantum dynamics of single trapped ions*, Rev. Mod. Phys. **75**, 281–324 (Mar 2003).

[Lew07] M. Lewenstein, A. Sanpera, V. Ahufinger, B. Damski, A. Sen, U. Sen, *Ultracold atomic gases in optical lattices: mimicking condensed matter physics and beyond*, Advances in Physics **56**, 243–379 (März 2007).

[Li05] W. Li, P. J. Tanner, T. F. Gallagher, *Dipole-Dipole Excitation and Ionization in an Ultracold Gas of Rydberg Atoms*, Phys. Rev. Lett. **94**, 173001 (May 2005).

[Lie05] T. C. Liebisch, A. Reinhard, P. R. Berman, G. Raithel, *Atom Counting Statistics in Ensembles of Interacting Rydberg Atoms*, Phys. Rev. Lett. **95**(25), 253002 (Dec 2005).

[Liu01] C. Liu, Z. Dutton, C. H. Behroozi, L. V. Hau, *Observation of coherent optical information storage in an atomic medium using halted light pulses*, Nature **409**(6819), 490–493 (2001).

[Loc13] G. Lochead, D. Boddy, D. P. Sadler, C. S. Adams, M. P. A. Jones, *Number-resolved imaging of excited-state atoms using a scanning autoionization microscope*, Phys. Rev. A **87**, 053409 (May 2013).

[Lon05] J. J. Longdell, E. Fraval, M. J. Sellars, N. B. Manson, *Stopped Light with Storage Times Greater than One Second Using Electromagnetically Induced Transparency in a Solid*, Phys. Rev. Lett. **95**, 063601 (Aug 2005).

[Löw09] R. Löw, H. Weimer, U. Krohn, R. Heidemann, V. Bendkowsky, B. Butscher, H. P. Büchler, T. Pfau, *Universal scaling in a strongly interacting Rydberg gas*, Phys. Rev. A **80**, 033422 (Sep 2009).

[Löw12] R. Löw, H. Weimer, J. Nipper, J. B. Balewski, B. Butscher, H. P. Büchler, T. Pfau, *An experimental and theoretical guide to strongly interacting Rydberg gases*, Journal of Physics B: Atomic, Molecular and Optical Physics **45**(11), 113001 (2012).

[Luk01] M. D. Lukin, M. Fleischhauer, R. Cote, L. M. Duan, D. Jaksch, J. I. Cirac, P. Zoller, *Dipole Blockade and Quantum Information Processing in Mesoscopic Atomic Ensembles*, Phys. Rev. Lett. **87**, 037901 (Jun 2001).

[Mai60] T. H. Maiman, *Stimulated Optical Radiation in Ruby*, Nature **187**, 493–494 (Aug 1960).

[Mal93] S. Mallat, Z. Zhang, *Matching pursuits with time-frequency dictionaries*, Signal Processing, IEEE Transactions on **41**(12), 3397–3415 (1993).

[Mar07] K. P. Marzlin, *Physics 673: Quantum Optics and Nonlinear Optics* (2007).

[Mat04] D. N. Matsukevich, A. Kuzmich, *Quantum State Transfer Between Matter and Light*, Science **306**(5696), 663–666 (2004).

[Max13] D. Maxwell, D. J. Szwer, D. Paredes-Barato, H. Busche, J. D. Pritchard, A. Gauguet, K. J. Weatherill, M. P. A. Jones, C. S. Adams, *Storage and Control of Optical Photons Using Rydberg Polaritons*, Phys. Rev. Lett. **110**, 103001 (Mar 2013).

[McQ13] P. McQuillen, X. Zhang, T. Strickler, F. B. Dunning, T. C. Killian, *Imaging the evolution of an ultracold strontium Rydberg gas*, Phys. Rev. A **87**, 013407 (Jan 2013).

[Mes96] D. Meschede, A. Rauschenbeutel, *Manipulating single atoms*, Adv. At. Mol. Opt. Phys. **53**, 75 (1996).

[Met07] H. J. Metcalf, P. Straten, *Laser Cooling and Trapping* (Springer, 2007).

[Moe07] W. E. Moerner, *New directions in single-molecule imaging and analysis*, Proceedings of the National Academy of Sciences **104**(31), 12596–12602 (2007).

[Moh07] A. K. Mohapatra, T. R. Jackson, C. S. Adams, *Coherent Optical Detection of Highly Excited Rydberg States Using Electromagnetically Induced Transparency*, Physical Review Letters **98**(11), 113003 (2007).

[Moh08] A. K. Mohapatra, M. G. Bason, B. Butscher, K. J. Weatherill, C. S. Adams, *A giant electro-optic effect using polarizable dark states*, Nature Physics **4**, 890–894 (2008).

[Mon02] C. Monroe, *Quantum information processing with atoms and photons*, Nature **416**(6877), 238–246 (2002).

[Mou98] I. Mourachko, D. Comparat, F. de Tomasi, A. Fioretti, P. Nosbaum, V. M. Akulin, P. Pillet, *Many-Body Effects in a Frozen Rydberg Gas*, Phys. Rev. Lett. **80**, 253–256 (Jan 1998).

[Mue13] W. Muessel, H. Strobel, M. Joos, E. Nicklas, I. Stroescu, J. Tomkovic, D. B. Hume, M. K. Oberthaler, *Optimized absorption imaging of mesoscopic atomic clouds*, Applied Physics B **113**(1), 69–73 (2013).

[Mül07] O. Mülken, A. Blumen, T. Amthor, C. Giese, M. Reetz-Lamour, M. Weidemüller, *Survival Probabilities in Coherent Exciton Transfer with Trapping*, Phys. Rev. Lett. **99**, 090601 (Aug 2007).

[Mül09] M. Müller, I. Lesanovsky, H. Weimer, H. P. Büchler, P. Zoller, *Mesoscopic Rydberg Gate Based on Electromagnetically Induced Transparency*, Phys. Rev. Lett. **102**(17), 170502 (Apr 2009).

[Mül10] N. L. M. Müller, *Excitation and detection of Rydberg atoms in an ultracold gas — Electric field design and electromagnetically induced transparency*, Masters Thesis, Department of Physics and Astronomy, University of Heidelberg (2010).

[Mül12] M. Müller, S. Diehl, G. Pupillo, P. Zoller, *Engineered Open Systems and Quantum Simulations with Atoms and Ions*, in E. A. Paul Berman, C. Lin

(Ed.), *Advances in Atomic, Molecular, and Optical Physics*, Vol. 61 of *Advances In Atomic, Molecular, and Optical Physics*, 1 – 80 (Academic Press, 2012).

[Nag86] W. Nagourney, J. Sandberg, H. Dehmelt, *Shelved optical electron amplifier: Observation of quantum jumps*, Phys. Rev. Lett. **56**, 2797–2799 (Jun 1986).

[Naj10] H. Najafov, B. Lee, Q. Zhou, L. Feldman, V. Podzorov, *Observation of long-range exciton diffusion in highly ordered organic semiconductors*, Nature materials **9**, 938–943 (2010).

[Nel07] K. D. Nelson, X. Li, D. S. Weiss, *Imaging single atoms in a three-dimensional array*, Nature Physics **3**(8), 556–560 (2007).

[Nik12] G. Nikoghosyan, F. E. Zimmer, M. B. Plenio, *Dipolar Bose-Einstein condensate of dark-state polaritons*, Phys. Rev. A **86**, 023854 (Aug 2012).

[Nip12] J. Nipper, J. B. Balewski, A. T. Krupp, B. Butscher, R. Löw, T. Pfau, *Highly Resolved Measurements of Stark-Tuned Förster Resonances between Rydberg Atoms*, Phys. Rev. Lett. **108**, 113001 (Mar 2012).

[Ock10] C. F. Ockeloen, A. F. Tauschinsky, R. J. C. Spreeuw, S. Whitlock, *Detection of small atom numbers through image processing*, Phys. Rev. A **82**, 061606 (Dec 2010).

[Oij99] A. M. van Oijen, M. Ketelaars, J. Köhler, T. J. Aartsma, J. Schmidt, *Unraveling the Electronic Structure of Individual Photosynthetic Pigment-Protein Complexes*, Science **285**(5426), 400–402 (1999).

[Olm11] B. Olmos, W. Li, S. Hofferberth, I. Lesanovsky, *Amplifying single impurities immersed in a gas of ultracold atoms*, Phys. Rev. A **84**, 041607 (Oct 2011).

[Ott13] J. Otterbach, M. Moos, D. Muth, M. Fleischhauer, *Wigner Crystallization of Single Photons in Cold Rydberg Ensembles*, Phys. Rev. Lett. **111**, 113001 (Sep 2013).

[Pan00] S. H. Pan, E. W. Hudson, K. M. Lang, H. Eisaki, S. Uchida, J. C. Davis, *Imaging the effects of individual zinc impurity atoms on superconductivity in Bi2Sr2CaCu2O8+ δ*, Nature **403**(6771), 746–750 (2000).

[Per13] S. Perseguers, G. J. L. Jr, D. Cavalcanti, M. Lewenstein, A. Acin, *Distribution of entanglement in large-scale quantum networks*, Reports on Progress in Physics **76**(9), 096001 (2013).

[Pet11] D. Petrosyan, J. Otterbach, M. Fleischhauer, *Electromagnetically Induced Transparency with Rydberg Atoms*, Phys. Rev. Lett. **107**, 213601 (Nov 2011).

[Pey12] T. Peyronel, O. Firstenberg, Q.-Y. Liang, S. Hofferberth, A. V. Gorshkov, T. Pohl, M. D. Lukin, V. Vuletić, *Quantum nonlinear optics with single photons enabled by strongly interacting atoms*, Nature **488**, 57–60 (August 2012).

[Phi01] D. F. Phillips, A. Fleischhauer, A. Mair, R. L. Walsworth, M. D. Lukin, *Storage of Light in Atomic Vapor*, Phys. Rev. Lett. **86**, 783–786 (Jan 2001).

[Pla01] M. Planck, *Über das Gesetz der Energieverteilung im Normalspektrum*, Annalen der Physik **4**, 553 (1901).

[Poh10] T. Pohl, E. Demler, M. D. Lukin, *Dynamical Crystallization in the Dipole Blockade of Ultracold Atoms*, Phys. Rev. Lett. **104**(4), 043002 (Jan 2010).

[Pri10] J. D. Pritchard, D. Maxwell, A. Gauguet, K. J. Weatherill, M. P. A. Jones, C. S. Adams, *Cooperative Atom-Light Interaction in a Blockaded Rydberg Ensemble*, Phys. Rev. Lett. **105**, 193603 (Nov 2010).

[Pri11] J. Pritchard, *Cooperative Optical Non-linearity in a blockaded Rydberg ensemble*, Dissertation, Durham University (2011).

[Pri13] J. D. Pritchard, K. J. Weatherill, C. S. Adams, *Non-linear optics using cold Rydberg atoms*, Annual Review of Cold Atoms and Molecules **1**, 301 (2013).

[Pup10] G. Pupillo, A. Micheli, M. Boninsegni, I. Lesanovsky, P. Zoller, *Strongly Correlated Gases of Rydberg-Dressed Atoms: Quantum and Classical Dynamics*, Phys. Rev. Lett. **104**(22), 223002 (Jun 2010).

[Reg04] C. A. Regal, M. Greiner, D. S. Jin, *Observation of Resonance Condensation of Fermionic Atom Pairs*, Phys. Rev. Lett. **92**, 040403 (Jan 2004).

[Rit12] S. Ritter, C. Nölleke, C. Hahn, A. Reiserer, A. Neuzner, M. Uphoff, M. Mücke, E. Figueroa, J. Bochmann, G. Rempe, *An elementary quantum network of single atoms in optical cavities*, Nature **484**(7393), 195–200 (2012).

[RN02] L. Rebollo-Neira, D. Lowe, *Optimized orthogonal matching pursuit approach*, Signal Processing Letters, IEEE **9**(4), 137–140 (2002).

[Rob04] F. Robicheaux, J. V. Hernández, T. Topçu, L. D. Noordam, *Simulation of coherent interactions between Rydberg atoms*, Phys. Rev. A **70**, 042703 (Oct 2004).

[Rob05] F. Robicheaux, J. V. Hernández, *Many-body wave function in a dipole blockade configuration*, Phys. Rev. A **72**(6), 063403 (Dec 2005).

[Röh12] R. Röhlsberger, H.-C. Wille, K. Schlage, B. Sahoo, *Electromagnetically induced transparency with resonant nuclei in a cavity*, Nature **482**(7384), 199–203 (2012).

[Rol08] S. L. Rolston, *Ultracold neutral plasmas*, Physics **1**, 2 (Jul 2008).

[Ros07] D. Rossini, R. Fazio, *Mott-Insulating and Glassy Phases of Polaritons in 1D Arrays of Coupled Cavities*, Phys. Rev. Lett. **99**, 186401 (Oct 2007).

[Rya10] I. I. Ryabtsev, D. B. Tretyakov, I. I. Beterov, V. M. Entin, *Observation of the Stark-Tuned Förster Resonance between Two Rydberg Atoms*, Phys. Rev. Lett. **104**, 073003 (Feb 2010).

[Ryd90] J. Rydberg, *Recherches sur la constitution des spectres d'émission des éléments chimiques*, Kongl. Svenska Vetenskaps Akademians Handlin-gar **23** (1890).

[Saf10] M. Saffman, T. G. Walker, K. Mølmer, *Quantum information with Rydberg atoms*, Rev. Mod. Phys. **82**, 2313–2363 (Aug 2010).

[Sar10] M. Sarovar, A. Ishizaki, G. R. Fleming, K. B. Whaley, *Quantum entanglement in photosynthetic light harvesting complexes*, Nature Physics **6**, 462 (2010).

[Sch04] D. Schrader, I. Dotsenko, M. Khudaverdyan, Y. Miroshnychenko, A. Rauschenbeutel, D. Meschede, *Neutral Atom Quantum Register*, Phys. Rev. Lett. **93**, 150501 (Oct 2004).

[Sch10a] J. Schachenmayer, I. Lesanovsky, A. Micheli, A. J. Daley, *Dynamical crystal creation with polar molecules or Rydberg atoms in optical lattices*, New Journal of Physics **12**(10), 103044 (2010).

[Sch10b] H. Schempp, G. Günter, C. S. Hofmann, C. Giese, S. D. Saliba, B. D. DePaola, T. Amthor, M. Weidemüller, S. Sevinçli, T. Pohl, *Coherent Population Trapping with Controlled Interparticle Interactions*, Phys. Rev. Lett. **104**(17), 173602 (Apr 2010).

[Sch10c] S. Schmid, A. Härter, J. Denschlag, *Dynamics of a cold trapped ion in a Bose-Einstein condensate*, Physical Review Letters **105**(13), 133202 (2010).

[Sch11] A. Schwarzkopf, R. E. Sapiro, G. Raithel, *Imaging Spatial Correlations of Rydberg Excitations in Cold Atom Clouds*, Phys. Rev. Lett. **107**, 103001 (Aug 2011).

[Sch12] P. Schauß, M. Cheneau, M. Endres, T. Fukuhara, S. Hild, A. Omran, T. Pohl, C. Gross, S. Kuhr, I. Bloch, *Observation of spatially ordered structures in a two-dimensional Rydberg gas*, Nature **491**(7422), 87 (Nov 2012).

[Sch13a] T. Schaetz, C. R. Monroe, T. Esslinger, *Focus on quantum simulation*, New Journal of Physics **15**(8), 085009 (2013).

[Sch13b] H. Schempp, G. Günter, M. R. de Saint-Vincent, C. S. Hofmann, D. Breyel, A. Komnik, D. W. Schönleber, M. Gärttner, J. Evers, S. Whitlock, M. Weidemüller, *Full Counting Statistics of Laser Excited Rydberg Aggregates in a One-Dimensional Geometry*, arXiv:1308.0264 (2013).

[Scu97] M. Scully, S. Zubairy, *Quantum Optics* (Cambridge University Press, 1997).

[Sea83] M. J. Seaton, *Quantum defect theory*, Reports on Progress in Physics **46**(2), 167 (1983).

[Sed12] J. A. Sedlacek, A. Schwettmann, H. Kübler, R. Löw, T. Pfau, J. P. Shaffer, *Microwave electrometry with Rydberg atoms in a vapour cell using bright atomic resonances*, Nature Physics **8**(11), 819–824 (2012).

[Sev11] S. Sevinçli, N. Henkel, C. Ates, T. Pohl, *Nonlocal Nonlinear Optics in Cold Rydberg Gases*, Phys. Rev. Lett. **107**, 153001 (Oct 2011).

[Sha11] E. Shahmoon, G. Kurizki, M. Fleischhauer, D. Petrosyan, *Strongly interacting photons in hollow-core waveguides*, Phys. Rev. A **83**, 033806 (Mar 2011).

[She06] J. F. Sherson, H. Krauter, R. K. Olsson, B. Julsgaard, K. Hammerer, I. Cirac, E. S. Polzik, *Quantum teleportation between light and matter*, Nature **443**(7111), 557–560 (2006).

[Sin04] K. Singer, M. Reetz-Lamour, T. Amthor, L. G. Marcassa, M. Weidemüller, *Suppression of Excitation and Spectral Broadening Induced by Interactions in a Cold Gas of Rydberg Atoms*, Phys. Rev. Lett. **93**, 163001 (Oct 2004).

[Sin05] K. Singer, J. Stanojevic, M. Weidemüller, R. Robin Côté, *Long-range interactions between alkali Rydberg atom pairs correlated to the ns-ns, np-np and nd-nd asymptotes*, Journal of Physics B: Atomic, Molecular and Optical Physics **38**(2), S295 (2005).

[Sul94] S. Sultana, M. S. Zubairy, *Effect of finite bandwidth on refractive-index enhancement and lasing without inversion*, Phys. Rev. A **49**, 438–448 (Jan 1994).

[Tau10] A. Tauschinsky, R. M. T. Thijssen, S. Whitlock, H. B. van Linden van den Heuvell, R. J. C. Spreeuw, *Spatially resolved excitation of Rydberg atoms and surface effects on an atom chip*, Phys. Rev. A **81**(6), 063411 (Jun 2010).

[Tho06] J. K. Thompson, J. Simon, H. Loh, V. Vuletić, *A High-Brightness Source of Narrowband, Identical-Photon Pairs*, Science **313**(5783), 74–77 (2006).

[Ton04] D. Tong, S. M. Farooqi, J. Stanojevic, S. Krishnan, Y. P. Zhang, R. Côté, E. E. Eyler, P. L. Gould, *Local Blockade of Rydberg Excitation in an Ultracold Gas*, Phys. Rev. Lett. **93**(6), 063001 (Aug 2004).

[Tow10] C. H. Townes, *The first laser Charles H. Townes*, A Century of Nature: Twenty-One Discoveries that Changed Science and the World 107 (2010).

[TS11] H. Tanji-Suzuki, I. D. Leroux, M. H. Schleier-Smith, M. Cetina, A. T. Grier, J. Simon, V. Vuletić, *Chapter 4 - Interaction between Atomic Ensembles and Optical Resonators: Classical Description*, in P. B. E. Arimondo, C. Lin (Ed.), *Advances in Atomic, Molecular, and Optical Physics*, Vol. 60 of *Advances In Atomic, Molecular, and Optical Physics*, 201 – 237 (Academic Press, 2011).

[Tsi08] S. I. Tsintzos, N. T. Pelekanos, G. Konstantinidis, Z. Hatzopoulos, P. G. Savvidis, *A GaAs polariton light-emitting diode operating near room temperature*, Nature **453**(7193), 372 (Mai 2008).

[Vit11] M. Viteau, M. G. Bason, J. Radogostowicz, N. Malossi, D. Ciampini, O. Morsch, E. Arimondo, *Rydberg Excitations in Bose-Einstein Condensates in Quasi-One-Dimensional Potentials and Optical Lattices*, Phys. Rev. Lett. **107**(6), 060402 (Aug 2011).

[Vog06] T. Vogt, M. Viteau, J. Zhao, A. Chotia, D. Comparat, P. Pillet, *Dipole Blockade at Förster Resonances in High Resolution Laser Excitation of Rydberg States of Cesium Atoms*, Phys. Rev. Lett. **97**, 083003 (Aug 2006).

[Vul06] V. Vuletic, *When superatoms talk photons*, Nature Physics News & Views **2**, 801 (2006).

[Wal04] A. Wallraff, D. I. Schuster, A. Blais, L. Frunzio, R.-S. Huang, J. Majer, S. Kumar, S. M. Girvin, R. J. Schoelkopf, *Strong coupling of a single photon to a superconducting qubit using circuit quantum electrodynamics*, Nature **431**(7005), 162–167 (2004).

[Wal08] T. G. Walker, M. Saffman, *Consequences of Zeeman degeneracy for the van der Waals blockade between Rydberg atoms*, Phys. Rev. A **77**, 032723 (Mar 2008).

[Wea08] K. J. Weatherill, J. D. Pritchard, R. P. Abel, M. G. Bason, A. K. Mohapatra, C. S. Adams, *Electromagnetically induced transparency of an interacting cold Rydberg ensemble*, Journal of Physics B: Atomic, Molecular and Optical Physics **41**(20), 201002 (2008).

[Wei92] C. Weisbuch, M. Nishioka, A. Ishikawa, Y. Arakawa, *Observation of the coupled exciton-photon mode splitting in a semiconductor quantum microcavity*, Phys. Rev. Lett. **69**(23), 3314 (Dec 1992).

[Wei08] H. Weimer, R. Löw, T. Pfau, H. P. Büchler, *Quantum Critical Behavior in Strongly Interacting Rydberg Gases*, Physical Review Letters **101**(25), 250601 (2008).

[Wei10] H. Weimer, M. Müller, I. Lesanovsky, P. Zoller, H. P. Büchler, *A Rydberg quantum simulator*, Nature Physics **6**, 382 (2010).

[Wei11] C. Weitenberg, M. Endres, J. F. Sherson, M. Cheneau, P. Schauß, T. Fukuhara, I. Bloch, S. Kuhr, *Single-spin addressing in an atomic Mott insulator*, Nature **471**(7338), 319–324 (2011).

[Wes06] S. Westermann, T. Amthor, A. L. de Oliveira, J. Deiglmayr, M. Reetz-Lamour, M. Weidemüller, *Dynamics of resonant energy transfer in a cold Rydberg gas*, Eur. Phys. J. D **40**, 37 (2006).

[Wil10] T. Wilk, A. Gaëtan, C. Evellin, J. Wolters, Y. Miroshnychenko, P. Grangier, A. Browaeys, *Entanglement of Two Individual Neutral Atoms Using Rydberg Blockade*, Phys. Rev. Lett. **104**, 010502 (Jan 2010).

[Wit05] C. Wittig, *The Landau-Zener Formula*, The Journal of Physical Chemistry B **109**(17), 8428–8430 (2005), pMID: 16851989.

[Wüs10] S. Wüster, C. Ates, A. Eisfeld, J. M. Rost, *Newton's Cradle and Entanglement Transport in a Flexible Rydberg Chain*, Phys. Rev. Lett. **105**(5), 053004 (Jul 2010).

[Xie94] X. S. Xie, R. C. Dunn, *Probing Single Molecule Dynamics*, Science **265**(5170), 361–364 (1994).

[Yaz97] A. Yazdani, B. A. Jones, C. P. Lutz, M. F. Crommie, D. M. Eigler, *Probing the Local Effects of Magnetic Impurities on Superconductivity*, Science **275**(5307), 1767–1770 (1997).

[Zim11] F. Zimmer, G. Nikoghosyan, M. Plenio, *Dipolar Bose-Einstein condensate of Stationary-Light Dark-state Polaritons*, arXiv:1103.2395 (2011).

[Zip10] C. Zipkes, S. Palzer, C. Sias, M. Kohl, *A trapped single ion inside a Bose-Einstein condensate*, Nature **464**, 388 (2010).

Danksagung

An dieser Stelle möchte ich mich bei all jenen bedanken, ohne die die Durchführung und das Gelingen dieser Arbeit undenkbar gewesen wäre. Mein besonderer Dank gilt

meinem Betreuer **Prof. Dr. Matthias Weidemüller** für die Möglichkeit in seiner Arbeitsgruppe diese interessante und spannende Doktorarbeit durchführen zu können, bei der ich sehr viel lernen konnte. Ich danke dir für das Vertrauen, das du mir von Anfang an entgegengebracht hast, für deine stets offene Tür und deine Unterstützung sowie für unsere zahlreichen Diskussionen, in denen ich viel von Dir über die Physik und das Leben gelernt habe.

Prof. Dr. Markus Oberthaler für die freundliche Übernahme des Zweitgutachtens.

It has been my pleasure to work with **Shannon Whitlock**. Your enthusiasm and your seemingly endless ideas and energy have lifted this project on a new level. Your drive and our countless discussion were great motivation for me and have enlightened me many times. Thanks a lot!

Merci à **Martin Robert de Saint Vincent** pour sa joie communicative pour la physique, pour ses calculs griffonnés sur des dos d'enveloppes qui jouèrent un rôle crucial dans notre réussite de ces dernières années, pour une inoubliable nuit pizza/acquisition de données, le tout en lunettes de protection: sécurité oblige! Mais aussi pour simplement être celui que l'on appelle "Martin", "Robert", "Vincent" sans oublier "Herbert" selon l'envie du jour.

Ein besonderer Dank geht an **Hanna Schempp** für die schönen gemeinsamen Jahre, die uns nun zu Rydberg-Oldies gemacht haben. Ich danke dir für die sehr gute Zusammenarbeit im Labor, deine große Unterstützung bei den Experimenten vor dem Umzug, die lustigen Stunden am Tischkicker mit "Miss-One-Touch" und die wunderbare Zeit des gemeinsamen Musizierens.

Christoph Hofmann für die tolle Planung des neuen Aufbaus. Ohne deine Begeisterung für kleine Details wie Zauberschrauben, die gute Planung des Aufbaus und deinen Enthusiasmus für "the horny machine" wären, die tollen Experimente der letzten beiden Jahre nicht möglich gewesen.

Vladislav Gavryusev and **Miguel Ferreira Cao** for now taking over with the experiment and continuing all the interesting projects. I wish you all the best!

allen Mitgliedern des **Rydberg-Teams** der letzten Jahre. Die erfolgreichen Jahre am

Rydberg-Experiment waren auch ein Verdienst der vielen tollen Diplomanden und Masterstudenten Nele Müller, Aline Faber, Hannes Busche, Henning Labuhn, Max Argus und Stephan Helmrich. Die schöne gemeinsame Zeit und das freundschaftliche Klima, haben mir immer viel Freude bereitet und waren ein wichtiger Bestandteil für das Gelingen meiner Arbeit.

Marc Repp, Rico Pires und **Juris Ulmanis** und dem gesamten **Mixtures-Team** alias "Marc-and-the-Kids" sowie dem **Motrims-Team** um **Bastian Höltkemeier** für die stets gute und hilfsbereite Atmosphäre in der gesamten Arbeitsgruppe. Ohne euch und die vielen lustigen Stunden am Kicker oder auch außerhalb der Uni wäre die Zeit der Doktorarbeit nicht halb so schön gewesen.

Ein großer Dank geht auch an die **Werkstätten des Physikalischen Instituts**. Die großartige Unterstützung durch die Mechanische und die Elektronik-Werkstatt bei der Planung und beim Aufbau des neuen Experiments haben einen großen Anteil am Erfolg der durchgeführten Experimente. Insbesondere möchte ich mich bei **Ralf Ziegler** bedanken, der für alle Probleme im und ums PI eine Lösung findet. Ein großer Dank geht auch an **Dominik Litsch** für seine Hilfsbereitschaft bei kleineren und größeren mechanischen Problemen sowie seine große Unterstützung beim Bau von Christophs Doktorhut. Außerdem möchte ich mich bei **Venelin Angelov** für seine Hilfe bei zahlreichen Elektronikproblemen und bei **Klaus Layer** für seinen unermütlichen Einsatz bei der Entwicklung der Behlke-Schalter bedanken. Auch geht ein großes Dankeschön an **Claudia Krämer** für die Hilfe bei zahlreichen administrativen und bürokratischen Aufgaben.

der **Studienstiftung des deutschen Volkes** für die Unterstützung während der Promotion und die Möglichkeit auf interessanten Veranstaltungen meinen Horizont zu erweitern und spannende Menschen kennenzulernen.

Rick van Bijnen for the awesome time we had climbing many summits in the Alps combined with interesting discussions about physics and many other things. I'm looking forward to many more to come!

Annabelle, Tobias und Christiane, die mich hier in Heidelberg in den letzten Jahren begleitet haben. Die vielen fröhlichen Stunden, aber auch die gemeinsame Zeit in schwierigen Phasen der letzten Jahre haben mir immer wieder viel Kraft für meine Arbeit gegeben.

meinen Eltern, Friedhelm, Maren und Leni und **allen Freunden**, die mich die ganze Zeit unterstützt haben und immer für mich da waren. Vielen Dank dafür!